Status of Muon Collider Research and Development and Future Plans

Charles M. Ankenbrandt[1], Giorgio Apollinari[2], Muzaffer Atac[1], Bruno Autin[3], Valeri I. Balbekov[1], Vernon D. Barger[4], Odette Benary[5], Scott Berg[6], Michael S. Berger[6], S. Alex Bogacz[7], T. Bolton[8], Shlomo Caspi[9], Christine Celata[9], Yong-Chul Chae[10], David B. Cline[11], John Corlett[9], Lucien Cremaldi[12], H. Thomas Diehl[1], Alexandr Drozhdin[1], Richard C. Fernow[13], David A. Finley[1], Yasuo Fukui[14], Miguel A. Furman[9], Tony Gabriel[15], Juan C. Gallardo[13*], Alper A. Garren[11], Stephen H. Geer[1], Ilya F. Ginzburg[16], Michael A. Green[9], John F. Gunion[17], Ramesh Gupta[9], Tao Han[17], Katherine C. Harkay[10], Colin Johnson[3], Carol Johnstone[1], Stephen A. Kahn[13], Bruce J. King[13], Harold G. Kirk[13], Masayukiu Kumada[18], Yoshitaka Kuno[14], Paul LeBrun[1], Kevin Lee[11], Derun Li[9], David Lissauer[13], Laurence S. Littenberg[13], Changguo Lu[19], Alfredo Luccio[13], Kirk T. McDonald[19], Alfred D. McInturff[9], Frederick E. Mills[1], Nikolai V. Mokhov[1], Alfred Moretti[1], David V. Neuffer[1], King-Yuen Ng[1], Robert J. Noble[1], James H. Norem[10,1], Blaine E. Norum[20], Hiromi Okamoto[21], Yasar Onel[22], Robert B. Palmer[13], Zohreh Parsa[13], Jack M. Peterson[9], Yuriy Pischalnikov[11], Milorad Popovic[1], Eric J. Prebys[19], Zubao Qian[1], Rajendran Raja[1], Pavel Rehak[13], Thomas Roser[13], Robert Rossmanith[23], Jack Sandweiss[24], Ronald M. Scanlan[9], Lindsay Schachinger[9], Andrew M. Sessler[9], Quan-Sheng Shu[7], Gregory I. Silvestrov[25], Alexandr N. Skrinsky[25], Panagiotis Spentzouris[1], Ray Stefanski[1], Sergei Striganov[1], Iuliu Stumer[13], Don Summers[12], Valery Tayursky[25], Valeri Tcherniatine[13], Lee C. Teng[10], Alvin V. Tollestrup[1], Yağmur Torun[13,26], Dejan Trbojevic[13], William C. Turner[9], Andy Van Ginneken[1], Tatiana A. Vsevolozhskaya[25], Masayoshi Wake[14], Weishi Wan[1], Haipeng Wang[13], Robert Weggel[13], Erich H. Willen[13], David R. Winn[27], Jonathan S. Wurtele[28], Yongxiang Zhao[13], Max Zolotorev[9]

[1]*Fermi National Laboratory, P. O. Box 500, Batavia, IL 60510*
[2]*Rockefeller University, New York, NY 10021*
[3]*CERN, 1211 Geneva 23, Switzerland*
[4]*Department of Physics, University of Wisconsin, Madison, WI 53706*
[5]*Tel-Aviv University, Ramat-Aviv, Tel-Aviv 69978, Israel*
[6]*Physics Department, Indiana University, Bloomington, IN 47405*
[7]*Jefferson Laboratory, 12000 Jefferson Ave., Newport News, VA 23606*
[8]*Kansas State University, Manhattan, KS 66502-2601*
[9]*Lawrence Berkeley National Laboratory, 1 Cyclotron Rd., Berkeley, CA 94720*
[10]*Argonne National Laboratory, Argonne, IL 60439*
[11]*University of California Los Angeles, Los Angeles, CA 90095*
[12]*University of Mississippi, Oxford, MS 38677*
[13]*Brookhaven National Laboratory, Upton, NY 11973*
[14]*KEK High Energy Accelerator Research Organization, 1-1 Oho, Tsukuba 305, Japan*
[15]*Oak Ridge National Laboratory, Oak Ridge, TN 37831*
[16]*Institute of Mathematics, Prosp. ac. Koptyug 4, 630090 Novosibirsk, Russia*
[17]*Physics Department, University of California, Davis, CA 95616*
[18]*National Institute of Radiological Sciences, 4-9-1 Anagawa, Inage, Chiba, Japan*
[19]*Joseph Henry Laboratories, Princeton University, Princeton, NJ 08544*
[20]*University of Virginia, 205 McCormick Road, Charlottesville, VA 22901*
[21]*N.S.R.F, Institute for Chemical Research, Kyoto University, Gokanoshou, Uji, Kyoto 611, Japan*
[22]*Physics Department, Van Allen Hall, University of Iowa, Iowa City, IA 52242*
[23]*DESY, Hamburg, Germany*
[24]*Physics Department, Yale University, CT 06520*
[25] *Budker Institute of Nuclear Physics, 630090 Novosibirsk, Russia*
[26]*Department of Physics and Astronomy, SUNY, Stony Brook, NY 11790*
[27]*Fairfield University, Fairfield, CT 06430*
[28]*University of California Berkeley, Berkeley, CA 94720*

(July 6, 1998)

The status of the research on muon colliders is discussed and plans are outlined for future theoretical and experimental studies. Besides continued work on the parameters of a 3-4 and 0.5 TeV center of mass (CoM) collider, many studies are now concentrating on a machine near 100 GeV

*Corresponding author. Email:gallardo@bnl.gov

(CoM) that could be a factory for the s-channel production of Higgs particles. We discuss the research on the various components in such muon colliders, starting from the proton accelerator needed to generate pions from a heavy-Z target and proceeding through the phase rotation and decay ($\pi \rightarrow \mu\,\nu_{\mu}$) channel, muon cooling, acceleration, storage in a collider ring and the collider detector. We also present theoretical and experimental R & D plans for the next several years that should lead to a better understanding of the design and feasibility issues for all of the components. This report is an update of the progress on the R & D since the Feasibility Study of Muon Colliders presented at the Workshop Snowmass'96 [R. B. Palmer, A. Sessler and A. Tollestrup, *Proceedings of the 1996 DPF/DPB Summer Study on High-Energy Physics* (Stanford Linear Accelerator Center, Menlo Park, CA, 1997)].

29.27.-a,29.27.Bd,29.20.-c,29.20.Dh,29.25.-a,41.85.-p,41.75.Lx,41.75.-i,13.35.Bv,13.10.+9,14.60.Ef

I. INTRODUCTION

The possibility of muon colliders was introduced by G. I Budker [1,2], Skrinsky et al. [3–5] and Neuffer [6,7]. More recently, a collaboration of over 100 members, led by Brookhaven National Laboratory (BNL), Fermi National Accelerator Laboratory (FNAL), Lawrence Berkeley National laboratory (LBNL), Budker Institute for Nuclear Physics (BINP), University of Mississippi, Princeton University and University of California at Los Angeles (UCLA) has been formed to coordinate studies on specific designs. The studies on the particle physics that could be done at the collider is led by the University of Wisconsin, University of California at Davis (UCD) and Indiana University. Work has been done on designs at 3-4 TeV, 0.4-0.5 TeV and $\approx$ 100 GeV [8–18]. A detailed feasibility study for a 4 TeV muon collider was presented at the SNOWMASS'96 workshop [19], [20].

The reason for interest in muon colliders comes from consequences of the muon behaving like a *heavy electron*. As for an electron, the full CoM energy is available in an interaction. But because of the large mass, there is essentially no synchrotron radiation from the muon (in comparison to electrons); consequently, the machine can be circular and much smaller than the current design of linear electron colliders and also much smaller than a hadron collider with the same *effective energy*. Of course, a muon collider requires successful solutions of many difficult physics and technical questions, but the cost of these solutions is not expected to be high. A further important consequence of the essential lack of synchrotron radiation is that the energy spread of the initial state at a muon collider can be very small; this opens up interesting particle physics possibilities.

For the first time, physicists are in a position to be able to effectively explore the Higgs mechanism for the origin of mass. We have the theoretical understanding to know where to look, we will soon have powerful enough accelerators to reach the requisite energy and we have the detectors that will allow us to study the subject. The first muon collider, that we describe here, is admirably suited for this task. Certainly, other machines can be, and will be, used to first determine some properties of the Higgs boson, but a detailed study of the Higgs–presumably the source of mass–will surely be called for, and a muon collider, as a copious producer of Higgs particles in the s-channel may be the ideal machine to perform that task.

Figs. 1 and 2 show possible outlines of the 3 TeV and 100 GeV machines. The assumed integrated luminosities, for the low energy machine, are given in Tb. I for three different energy spreads, $\mathcal{L}$=$1.2, 0.2, 0.1 \times 10^{32}\mathrm{cm}^{-2}\mathrm{s}^{-1}$ for $\frac{\Delta p}{p}\% = 0.12, 0.01, 0.003$, respectively.

Summarizing then, a $\mu^+\mu^-$collider would have some unique physics advantages over other collider options:

1. The direct coupling of a fermion-fermion system to a Higgs boson has a cross section that is proportional to the square of the mass of the fermion. As a result, the cross section for direct Higgs production from the $\mu^+\mu^-$system is 40,000 times that from an e^+e^-system.

2. Because of the lack of beamstrahlung, a $\mu^+\mu^-$collider can be operated with an energy spread of as little as 0.003 %. Furthermore, it will be possible to determine the absolute muon-beam energy to an accuracy of 10^{-6} or better [21] by observing the decay asymmetry of the naturally polarized muon beam (sec. VII-H). It should thus be possible to use a $\mu^+\mu^-$collider to make precision measurements of masses and direct measurements of the Higgs width (predicted to be $\approx$ 2 MeV) that would be otherwise impossible.

Machines with energies higher than 3-4 TeV, have significant beam-current constraints from off-site neutrino-induced-radiation limits (sec. VIII-B). If the required luminosities are to be reached without unacceptable hazards, then significant improvements in 6-dimensional muon emittance over the current baseline values are needed. There is, however, reason to believe such improvements are achievable, and machines with a center of mass energy of 10 TeV

TABLE I. Baseline parameters for high and low energy muon colliders (Higgs/year assumes $\sigma = 5 \times 10^4$ fb; $\Gamma = 2.7$ MeV; 1year $= 10^7$ s).

CoM energy	TeV	3	0.4		0.1	
p energy	GeV	16	16		16	
p's/bunch		2.5×10^{13}	2.5×10^{13}		5×10^{13}	
Bunches/fill		4	4		2	
Rep. rate	Hz	15	15		15	
p power	MW	4	4		4	
μ/bunch		2×10^{12}	2×10^{12}		4×10^{12}	
μ power	MW	28	4		1	
Wall power	MW	204	120		81	
Collider circum.	m	6000	1000		350	
Ave bending field	T	5.2	4.7		3	
Depth	m	500	100		10	
Rms $\frac{\Delta p}{p}$	%	0.16	0.14	0.12	0.01	0.003
6d ϵ_6	$(\pi \mathrm{m})^3$	1.7×10^{-10}	1.7×10^{-10}	1.7×10^{-10}	1.7×10^{-10}	1.7×10^{-10}
Rms ϵ_n	π mm mrad	50	50	85	195	290
β^*	cm	0.3	2.6	4.1	9.4	14.1
σ_z	cm	0.3	2.6	4.1	9.4	14.1
σ_r spot	μm	3.2	26	86	196	294
σ_θ IP	mrad	1.1	1.0	2.1	2.1	2.1
Tune shift		0.044	0.044	0.051	0.022	0.015
n_{turns} (effective)		785	700	450	450	450
Luminosity	$cm^{-2}s^{-1}$	7×10^{34}	10^{33}	1.2×10^{32}	2.2×10^{31}	10^{31}
Higgs/year				1.9×10^3	4×10^3	3.9×10^3

and luminosities of $10^{35}\mathrm{cm}^{-2}\mathrm{s}^{-1}$ and above have begun to be studied [22]. For energies below 3 TeV CoM and fixed muon currents, this radiation varies as the cube of the energy, and it should not be an issue for machines with energies of 1.5 TeV or less.

To minimize cost, a small initial machine is desirable, which would serve as a demonstration of the technology of muon colliders. A machine of 100-GeV scale could be commissioned at the Z^0 pole, and would have major physics impact should the mass of the Higgs boson be in this range.

The remainder of this report is organized as follows: Section II gives an overview of muon colliders and their physics potential; then there are sections on the proton driver (sec. III), the target, pion production, capture and phase rotation, polarization (sec. IV), ionization cooling (sec. V), acceleration (sec. VI), the collider ring lattice, and magnet design for the ring, muon beam energy calibration (sec. VII), radiation and backgounds including neutrino radiation health effects and detector background (sec. VIII). Sec. IX contains conclusions.

II. THE PHYSICS POTENTIAL OF MUON COLLIDERS

The physics opportunities and possibilities of muon colliders have been well documented in the Feasibility Study [20] and other papers, see ref. [23]. This section begins with a brief overview of the current theoretical and experimental status of High Energy Physics (HEP), then summarizes the contributions that muon colliders could make to extending our knowledge of elementary particles physics.

A. Brief Theoretical Overview

We could summarize the current status of HEP by stating that the observed pattern of properties of all known elementary particles has been accurately characterized by the standard model (SM), a well tested but cumbersome phenomenological theory containing 19 independent experimentally determined parameters. However, the SM is known to be an incomplete theory that gives inconsistent predictions when extrapolated to experimentally inaccessible mass scales, and even its predictions for the next generation of collider experiments are uncertain.

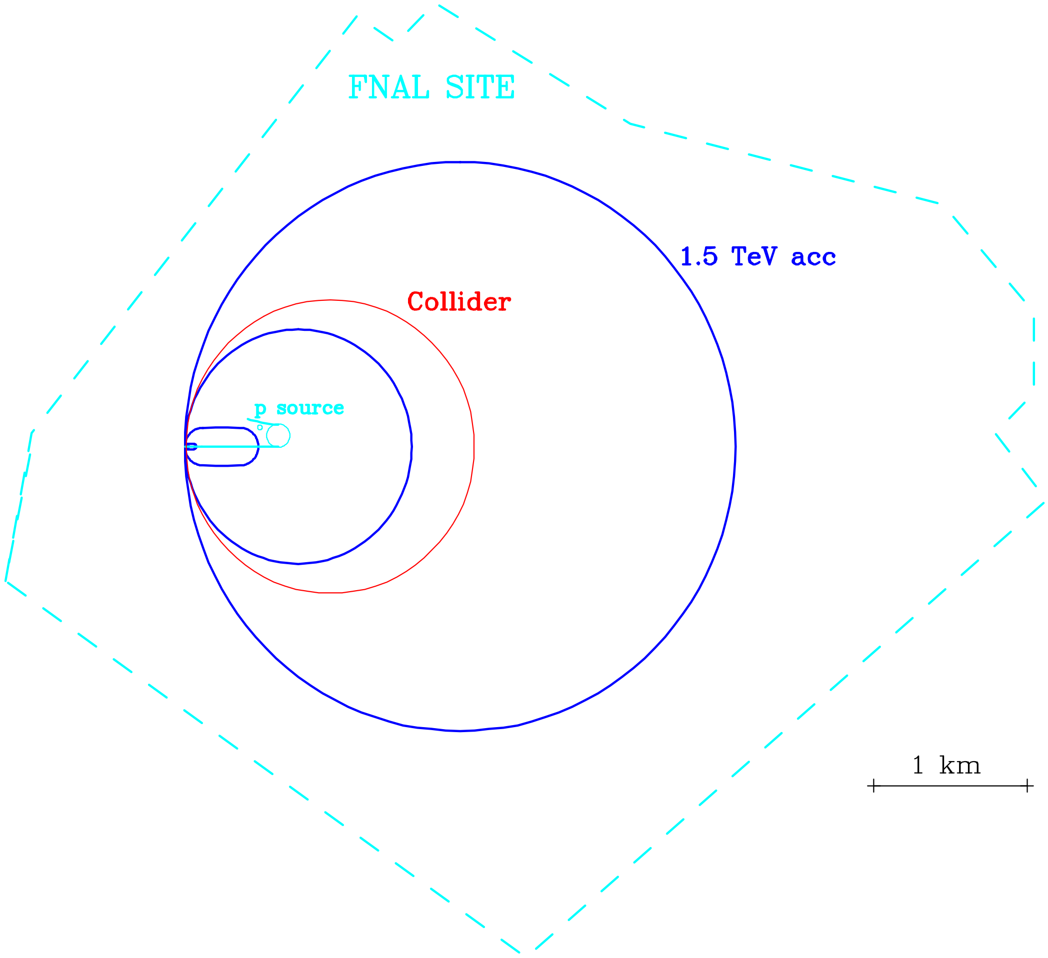

FIG. 1. Plan of a 3 TeV CoM Muon Collider shown on the Fermi National Laboratory site as an example.

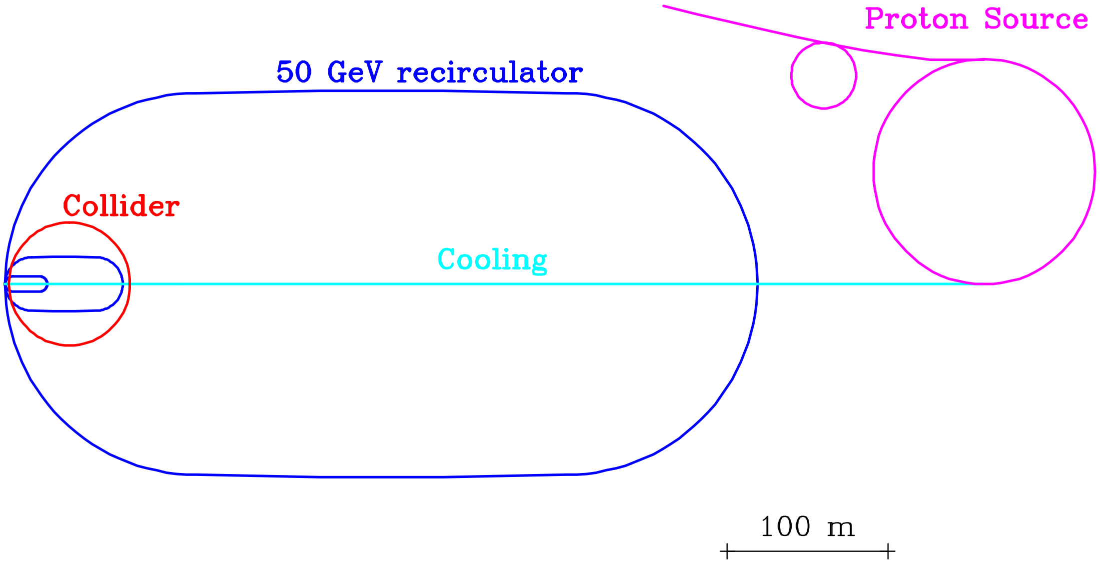

FIG. 2. Plan of a 100 GeV CoM Muon Collider.

Today's colliders have reached the threshold of an extremely interesting and fundamental mass scale in the SM: the electroweak symmetry breaking (EWSB) scale – at masses of order 100 GeV to 1 TeV. In the SM this is associated with the origin of the masses of all elementary particles through the so-called Higgs mechanism.

Recent collider experiments have already discovered and studied two of the three particles predicted by the SM at the EWSB mass scale, namely, the W and Z bosons that are the carriers of the weak force. However, the Higgs boson itself – the particle thought to be directly responsible for particle masses – still eludes detection.

Because the SM is known to be only an incomplete and phenomenological theory, we simply do not know if its prediction of a single Higgs particle at the EWSB scale is correct. In contrast, the most popular class of alternative theories, known as supersymmetric theories (SUSY), predict the possibility of an entirely new and rich spectrum of particles at this mass scale, including perhaps 5 types of Higgs bosons [23].

B. Potential Capabilities of Current Colliders

The discovery of the Higgs particle, if its mass is low enough, might be possible in the next few years at the LEP collider at CERN or at the FNAL Tevatron. Both of these colliders are currently taking data. Beyond this, the most powerful collider currently under construction is the Large Hadron Collider (LHC) at the European laboratory CERN, a proton-proton collider at 14 TeV center-of-mass (CoM) energy. The LHC is scheduled for completion in 2005 and will probably discover the Higgs boson if it exists and has not already been discovered elsewhere.

The LHC and other proton colliders offer the most established technology for reaching the high energy frontier of elementary particles. However, the physics potential of proton colliders is somewhat compromised because protons themselves are not elementary particles. The interesting physics interactions take place between their quark and gluon sub-components, so only a fraction of the CoM energy is available in each interaction and the interpretation of the interaction is more difficult. Further, the very large proton-proton cross section for soft interactions – of order 100 millibarns – produces an enormous event rate, so the interesting physics events must be disentangled from a huge pile-up of uninteresting background events. This problem becomes more acute at higher energies where the falling fundamental cross sections should dictate higher luminosities leading to even higher event rates and radiation levels.

C. The Need for Muon Colliders

Because of the experimental difficulties associated with proton colliders and the potential for other physics processes not explored in proton collisions, a strong case can be made for the complementary physics studies that can be done at high energy lepton colliders – either muon or linear electron-positron colliders.

The physics reach of the two types of lepton colliders has a large overlap, but there are also differences. Some of these differences result from differences in the physics processes, while others result from the completely different technical specifications of the colliders. Thus, their potential roles are also somewhat complementary, and studies at a muon collider would be able to provide important additional information, even if a new high energy linear electron collider were built. An example of this is the unique potential of muon colliders for very narrow CoM energy spreads that makes them particularly suited for both resonance production and threshold studies of elementary particles at energy scales of around 100 GeV and above.

D. Additional Physics Possibilities with Muon Beams

Further types of hybrid colliders become possible with the addition of muons to the menu of high energy particle beams. One possibility which is generating increased interest is muon-proton colliders [24]. This becomes a natural extension when a muon collider complex is built at a site already including a high energy proton machine, such as FNAL, CERN or DESY.

Additional collider possibilities that have been considered are same-sign muon colliders ($\mu^-\mu^-$ or $\mu^+\mu^+$) [24] or even muon-electron colliders.

The intense beams of muons and neutrinos in the complex also offer many opportunities for new physics. Rare muon decay or conversion experiments would be ideally suited for such a facility, while the neutrino beams might be several orders of magnitude stronger than existing beams. Neutrino studies [25,26] that could be greatly extended with such uniquely powerful beams include searches for neutrino oscillations, precise indirect measurements of the W boson mass and measurements of nucleon structure functions and the parameters of the CKM matrix. These and other areas of research have been recently summarized [27].

III. PROTON DRIVER

The overview of the required parameters is followed by a description of possible designs that have been studied in some detail. The section concludes with a discussion of the outstanding open issues.

A. Specifications

The proton driver requirements are determined by the design luminosity of the collider, and the efficiencies of muon collection, cooling, transport and acceleration. The baseline specification is for a 4 (7) MW, 16 (30) GeV proton driver, with a repetition rate of 15 Hz and 10^{14} protons per cycle in 2 bunches (for the 100 GeV machine) or 4 bunches (for the higher energies) of 5×10^{13} or 2.5×10^{13} protons respectively. Half the bunches are used to make μ^- and the other for μ^+.

The total beam power is several MW, which is larger than that of existing synchrotrons. However, except for bunch length, these parameters are similar to those of kaon factories [28] and spallation neutron sources [29]. As in those cases, the proton driver must have very low losses to permit inexpensive maintenance of components.

The rms bunch length for the protons on target has to be about 1 ns to: 1) reduce the initial longitudinal emittance of muons entering the cooling system and, 2) optimize the separation of the muon populations of + and - polarizations off the target. Although intensities of up to 6×10^{13} protons per cycle have been accelerated, the required peak currents, at extraction, for 1 ns and 4 bunches, is 2000 A which is unprecedented. In the low energy machine, to avoid the even higher current, bunch area requirements, and tune shift constraints, where two bunches of 5×10^{13} are required on target, two bunches can be merged outside the driver. Two bunches would be extracted simultaneously from two different extraction ports, and fed by different transmission lines to the same target. By arranging the path lengths of the two lines appropriately, the time of arrival of the two bunches can be exactly merged. This is explicitly assumed in the FNAL study quoted below.

Since the collection of polarized μ's is inefficient, to do polarized beam physics at the same luminosity, the proton driver should eventually provide an additional factor of approximately two to compensate for the inefficiency in producing these beams.

B. Possible Options

Accelerator designs are site, and to some extent, time dependent, and there have been three studies at three different energies (30, 16 and 24 GeV). In general, if the final energy is higher, the required currents are lower, bunch manipulation and apertures are easier, and the final momentum spread and space charge tune shifts are less. Lowering the final energy gives somewhat more π's/Watt, a lower rf requirement ($V_{rf} \sim E^2$) and perhaps a lower facility cost.

1. A Generic Design

A 7 MW collider driver design based on parameters originally proposed in the Snowmass Feasibility study [20], consists of a 600 MeV Linac, a 3.6 GeV Booster and a 30 GeV driver. Both Linac and Booster are copied from the BNL SNS design [29], using a lower repetition rate and a lower total number of protons per pulse. For the 4 bunch case (2.5×10^{13} protons per bunch), the (95%) bunch area is assumed to be 2 eVs at injection and <4.5 eVs at extraction. The driver lattice is derived from the lattice of the JHF driver using 90 degree FODO cells with missing dipoles in every third FODO cell, allowing a transition energy that is higher than the maximum energy, or perhaps imaginary.

2. FNAL Study

The 4 MW design [30] is described by Tb. II. It is a major upgrade of the present FNAL proton source. The driver lattice would be a Flexible Momentum Compaction (FMC) lattice, which is also used to raise the transition energy or make it imaginary.

The parameters of these two designs are somewhat similar. Both options assume a high transition energy, so that transition does not need to be crossed. The repetition rate of both booster and driver may permit the use of an

TABLE II. Baseline proton driver parameters

	Linac	**Booster**	**Driver**
Energy range	1 GeV	3 GeV	16 GeV
Rep. Rate	15 Hz	15 Hz	15 Hz
RF voltage per turn		0.15 MV	1.5 MV
Circumference		158 m	474 m
Protons per bunch		2.5×10^{13}	2.5×10^{13}
Beam Emittance [95 %]		200 π mm mrad	240 π mm mrad
Bunch Area [95%]		1.5 eVs	<2.0 eVs
Incoherent tune Shift @ Inj.		0.39	0.39

Inconel vacuum chamber with eddy current correction coils, which would be simpler and less expensive than the ceramic chamber with wires and blocking capacitors used at ISIS.

3. AGS Upgrade

The third study [31] is of an upgrade to the BNL AGS, which should produce bunches larger than those required for the muon collider, but at a lower repetition rate. The AGS presently produces 6×10^{13} protons in eight bunches at 25 GeV and 0.6 Hz. A 2.5 GeV accumulator ring in the AGS tunnel and AGS power supply upgrade to 2.5 Hz operation would match the repetition rate to the 10 Hz repetition rate of the booster. This would generate 1 MW. With an additional upgrade of the linac energy to 600 MeV, an intensity of 2×10^{14} protons per pulse in four bunches of 5×10^{13} at 25 GeV and 2.5 Hz could be reached, raising the power to 2 MW. Other options are also under consideration, such as the addition of a second booster and 5 Hz operation, that would reach the baseline specification of 4 MW.

The AGS momentum acceptance of $\pm 3\%$ requires that the longitudinal phase space occupied by one bunch be less than 4.5 eVs. This high bunch density in turn generates stringent demands on the earlier parts of the accelerator cycle. In particular, Landau damping from the beam momentum spread may guard against resistive wall instabilities during injection and longitudinal microwave instabilities after transition. Beam stability can be restored with a more powerful transverse damping system and possibly a new low impedance vacuum chamber. The transverse microwave instability is predicted to occur after transition crossing unless damped by Landau damping from incoherent tune spread or possibly high frequency quadrupoles.

C. Progress and Open Issues

Conventional rf manipulations appear able to produce 1 to 2 ns proton bunches if enough rf voltage to overcome the space charge forces is used, and the beam energy is far enough from transition so the final bunch rotation is fast. Both simulations and experimental work have been directed at demonstrating that a short pulse can be produced easily. An experiment at the AGS has shown that bunches with $\sigma \sim 2$ ns can be produced near transition from $\sigma \sim$ 8 ns bunches using an rf frequency of 3 MHz (which would be comparable to 1 ns with the 7 MHz systems proposed above) [32]. This experiment was done with bunches of 4×10^{12} protons. Simulations with the ESME code have also shown that 1 - 2 ns bunches of 5×10^{13} can be produced at extraction in a 16 GeV ring with the rf and emittance shown in Tb.II.

The efficiency of capturing and accelerating beam may be increased by compensation of the space charge forces in the proton driver. The use of tunable inductive inserts in the ring vacuum chamber may permit active control and compensation of the longitudinal space charge below transition (since the inductive impedance is of the opposite sign to the capacitive space charge) [33]. Initial experiments at the KEK proton synchrotron and Los Alamos PSR with short ferrite inserts appear to show a reduction in the synchrotron oscillation frequency shift caused by space charge and a decrease in the necessary rf voltage to maintain a given bunch intensity [34]. Further experiments are needed to fully demonstrate this technique.

The high rf voltage and beam power and the relatively small size of the machine require high gradient high power rf cavities. There is an agreement between Fermilab, BNL and KEK to collaborate on the research and development of such type of cavities. This work includes the study of magnet alloys and hybrid cavities using both ferrite and new magnet alloys, high power amplifiers and beam loading compensation.

The employment of barrier bucket rf cavities can effectively generate and manipulate a gap in the beam and reduce the space charge effect. Two barrier cavities have been built by BNL and KEK and will be installed on the AGS for test. Another high gradient barrier cavity using magnet alloys is under study at Fermilab.

IV. PION PRODUCTION, CAPTURE AND PHASE ROTATION CHANNEL

This subsection first discusses the choice of target technology, optimization of the target geometry, and then describes design studies for the pion capture and phase rotation channel.

Figure 3 gives an overview of the configuration for production of pions by a proton beam impinging on a long thin target, followed by capture of low-momentum, forward pions in a channel of solenoid magnets with rf cavities to compress the bunch energy while letting the bunch length grow: thus rotating the bunch in phase space.

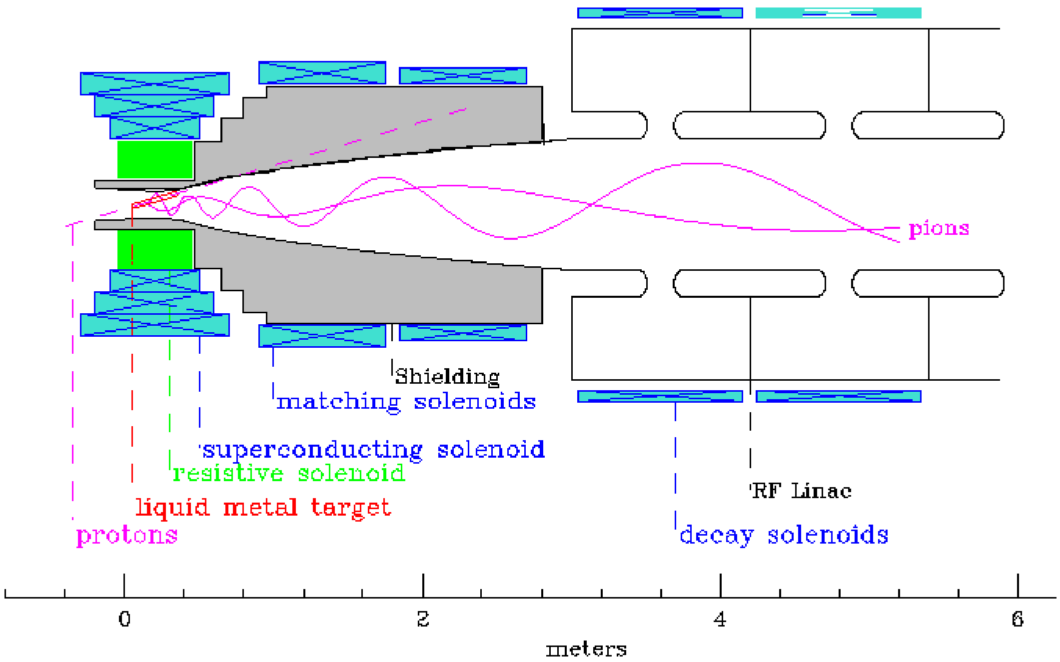

FIG. 3. Schematic view of pion production, capture and initial phase rotation: A pulse of 16-30 GeV protons is incident on a skewed target inside a high-field solenoid magnet followed by a decay and phase rotation channel.

A. Pion production

To achieve the luminosities for muon colliders presented in Tb. I, 2×10^{12} (or 4×10^{12} in the 100 GeV CoM case) muons of each sign must be delivered to the collider ring in each pulse. We estimate that a muon has a probability of only $\frac{1}{4}$ of surviving the processes of cooling and acceleration, due to losses in beam apertures or by decay. Thus, 0.8×10^{13} muons (1.6×10^{13} at 100 GeV) must exit the phase rotation channel each pulse. For pulses of 2.5×10^{13} protons (5×10^{13} for 100 GeV), this requires 0.3 muons per initial proton. And since the efficiency of the phase rotation channel is about 1/2, this is equivalent to a capture of about 0.6 pions per proton: a very high efficiency.

The pions are produced in the interaction of the proton beam with the primary target. Extensive simulations have been performed for pion production from 8-30 GeV proton beams on different target materials in a high-field solenoid [20,35,36]. Three different Monte Carlo codes [37–40] predict similar pion yields despite significant differences in their physics models. The Collaboration is involved in an AGS experiment [41] to measure the yield of very low momentum pions, which will validate the codes in the critical kinematic region.

The pion yield is greater for relatively high-Z materials, and for these, the pion yield is maximal for longitudinal momenta of the same order as the average transverse momentum (≈ 200 MeV/c). Targets of varying composition ($6 < Z < 82$), radii (0.4-3 cm) and thicknesses (0.5-3 nuclear interaction lengths (λ_I)) have been explored. For a fixed number of interaction lengths, the pion yield per proton rises almost linearly with proton energy [36], and hence almost proportional to the energy deposited in the target. The yield is higher for medium and high-Z target materials, with a noticeable gain at $Z > 26$ for 30 GeV proton beams, but with only a minor effect for $E \leq 16$ GeV, as shown in Fig. 4(a).

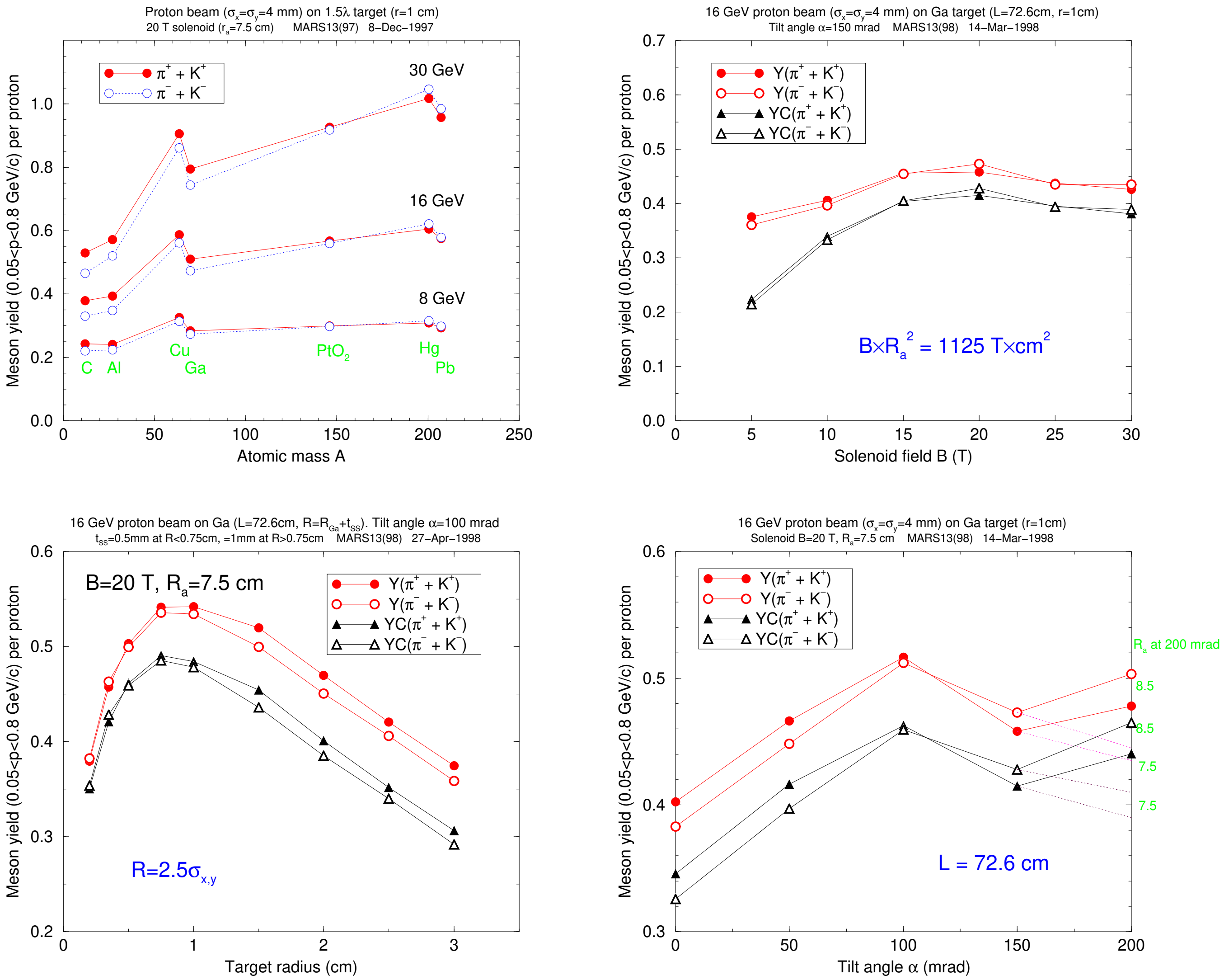

FIG. 4. (a) Meson yield ($\pi + K$) from a 1.5 λ_I, 1 cm radius target irradiated with 8, 16 and 30 GeV proton beams as a function of target atomic mass; (b) Meson yield from a 3 λ_I, 1 cm radius gallium target tilted at angle 150 mrad in a 16 GeV proton beam *vs.* solenoid field for a fixed adiabatic invariant BR_a^2; (c) Meson yield as a function of target radius; (d) Meson yield *vs.* tilt angle between the axis of the capture solenoid and the proton beam. The target is aligned along the beam. The curves labeled YC show mesons that are transported into the decay channel.

B. Target

The target should be 2-3 interaction lengths long to maximize pion production. A high density material is favored to minimize the size and cost of the capture solenoid magnet. Target radii larger than about 1 cm lead to lower pion rates due to reabsorption, while smaller diameter targets reduce the added production from secondary interactions. Tilting the target by 100-150 mrad minimizes loss of pions by absorption in the target after one turn on their helical trajectory. Another advantage of the tilted target geometry is that the high energy and neutral component of the shower can be absorbed in a water cooled beam dump to the side of the focused beam (see Fig. 3).

About 30 kJ of energy is deposited in the target by each proton pulse (10% of the beam energy). Hence, the target absorbs 400 kW of power at the 15 Hz pulse rate. Cooling of the target via contact with a thermal bath would lead to unacceptable absorption of pions, and radiative cooling is inadequate for such high power in a compact target. Therefore, the target must move so as to carry the energy deposited by the proton beam to a heat exchanger outside the solenoid channel.

Both moving solid metal and flowing liquid targets have been considered, with the latter as the currently preferred solution. A liquid is relatively easy to move, easy to cool, can be readily removed and replaced, and is the preferred target material for most spallation neutron sources under study. A liquid flowing in a pipe was considered, but calculations done at CERN [42] suggest serious problems in shock damage to the pipe. An open liquid jet is thus proposed.

A jet of liquid mercury has been demonstrated [42] but not exposed to a beam. For our application, safety and other considerations favor the use of a low-melting-point lead alloy rather than mercury. Gallium alloys, though with lower density, are also being considered. Experimental and theoretical studies are underway to determine the consequences of beam shock heating of the liquid. It is expected that the jet will disperse after being exposed to be beam. The target station must survive damage resulting from the violence in this dispersion. This consideration will determine the minimum beam, and thus jet, radius.

For a conducting liquid jet in a strong magnetic field, as proposed, strong eddy currents will be induced in the jet, causing reaction forces that may disrupt its flow [43,44]. The forces induced are proportional to the square of the jet radius, and set a maximum for this radius of order 5-10 mm. If this maximum is smaller than the minimum radius set by shock considerations, then multiple smaller beams and jets could be used; *e.g.*, four jets of 5 mm radius with four beams with 2.5 10^{13} protons per bunch. Alternatives include targets made from insulating materials such as liquid PtO_2 or Re_2O_3), slurries (*e.g.*, Pt in water), or powders [45].

A moving solid metal target is not the current baseline solution, but is a serious possibility. In this case [46] the target would consist of a long flat band or hoop of copper-nickel that moves along its length (as in a band saw). The band would be many meters in length, would be cooled by gas jets away from the target area, and would be supported and moved by rollers, as shown in Fig. 5.

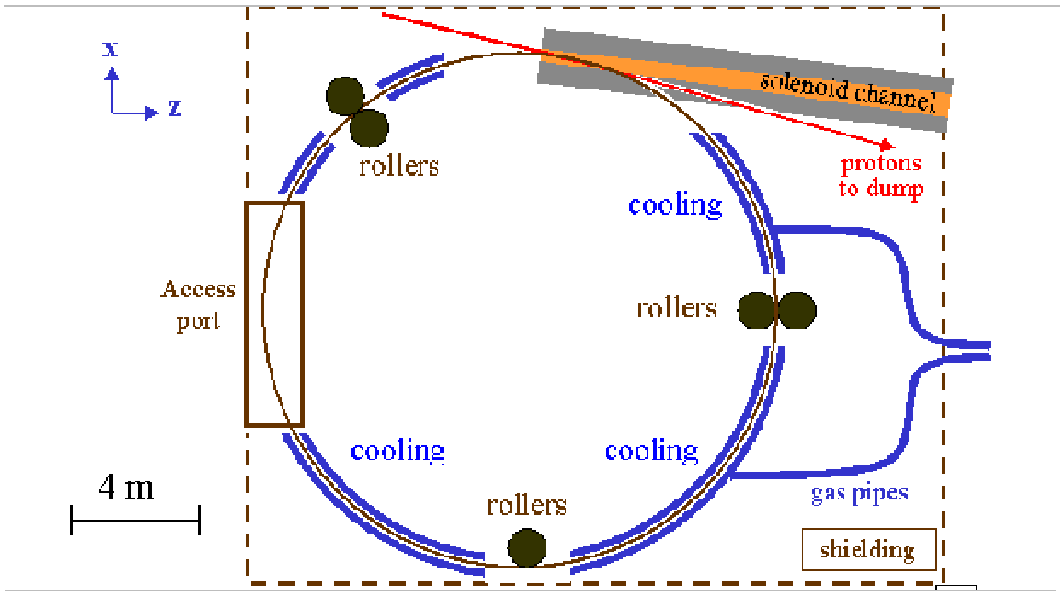

FIG. 5. Alternative concept of a solid metal target in the form of a rotating Cu-Ni band.

The choice and parameters of the target are a critical question that needs resolution. Only an experiment in a magnetic field and in a beam will settle it, and this is being planned.

C. Capture

In order to capture all pions with transverse momenta $P_\perp$ less than their typical values of 200 MeV/c, the product of the capture solenoid field B and its radius R_a must be greater than 1.33 T-m. The use of a high field and small radius is preferred to minimize the corresponding transverse emittance, which is proportional to BR^2: for a fixed transverse momentum capture, this emittance is thus proportional to R. A field of 20 T and 7.5 cm radius was chosen for the baseline. This gives $BR = 1.5$ T-m. $BR^2 = 0.1125$ T-m^2 and a maximum transverse momentum capture of $P_\perp = 225$ MeV$/c$.

A preliminary design [47] of the capture solenoid has an inner 6 T, 4 MW, water-cooled, hollow-conductor magnet with an inside diameter of 24 cm and an outside diameter of 60 cm. There is space for a 4 cm thick water-cooled heavy-metal shield inside the coil. The outer superconducting magnet has three coils, with inside diameters of 60 to 80 cm. It generates an additional 14 T of field at the target and provides the required tapered field to match into the decay channel. Such an hybrid solenoid has parameters compatible with those of existing magnets [48].

The 20-T capture solenoid is matched via a transfer solenoid [35] into a decay channel consisting of a system of superconducting solenoids with the same adiabatic invariant $BR^2 \propto RP_\perp$. Thus, for a 2.5-T decay channel, B drops by a factor of 1/8 between the target and decay channel, R and $P_\perp$ change by factors of $\sqrt{8}$ and $1/\sqrt{8}$, respectively. This permits improved acceptance of transverse momentum within the decay channel, at the cost of an increased spread in longitudinal momentum.

Detailed results of a simulation of pion production and capture are shown in Fig. 4.

The curves labeled YC in Fig. 4(b) show the yield of pions that are both captured in the high-field solenoid and transported into the decay channel as a function of field in the capture solenoid, with the radius of the capture solenoid adjusted to maintain the same BR_a^2 as in the decay channel. The optimum field is 20 T in the capture solenoid.

Figure 4(c) shows that pion production *vs* target radius has a maximum near $r = 0.85$ cm. This is the result of the competition between secondary production and tertiary absorption, both of which increase with target radius.

If the axis of the target is coincident with that of the solenoid field, then there is a relatively high probability that pions re-enter the target after one cycle on their helical trajectory and are lost due to nuclear interactions. When the target and proton beam are set at an angle of 100-150 mrad with respect to the field axis [36], the probability for such pion interactions at the target is reduced, and the overall production rate increased by 60 %, as shown in Fig. 4(d).

In sum, the simulations indicate that a 20 T solenoid of 16 cm inside diameter surrounding a tilted target will capture about half of all produced pions. With target efficiency included, about 0.6 pions per proton will enter the pion decay channel [36].

D. Phase Rotation Linac

The pions, and the muons into which they decay, have an energy spread with an rms value of approximately 100 % and a peak value at about 200 MeV/c. It would be difficult to handle such a wide spread in any subsequent system. A linac is thus introduced along the decay channel, with frequencies and phases chosen to deaccelerate the fast particles and accelerate the slow ones; i.e. to phase rotate the muon bunch. Several studies have been made of the design of this system, using differing ranges of rf frequency, delivering different final muon momenta, and differing final bunch lengths. In all cases, muon capture efficiencies of close to 0.3 muons per proton are obtained. Until the early stages of the ionization cooling have been designed, it is not yet possible to choose between them. Independent of the above choices is a question of the location of the focusing solenoid coils and rf cavity design. These will be discussed below in the subsection on Phase Rotation RF.

1. Lower Energy, longer bunch example

This example captures muons at a mean kinetic energy of 130 MeV. Tb.III gives parameters of the linacs used. It is seen that the frequencies vary between 60 and 30 MHz, and that the overall length is 42 m. Monte Carlo simulations [16], with the program MUONMC [49], were done using pion production calculated by ARC [37] for a copper target 1 cm radius at an angle of 150 mrad. A uniform solenoidal field was assumed in the phase rotation, and the rf was approximated by a series of kicks.

Fig. 6 shows the energy *vs.* c t at the end of the decay and phase rotation channel. A loose final bunch selection was defined with an energy 130 +/- 70 MeV and bunch ct from 3 to 11 m. With this selection, the rms energy spread is 16.5 %, the rms ct is 1.7 m, and there are 0.385 muons per incident proton. A tighter selection with an energy 130 +/- 35 MeV and bunch ct from 4 to 10 m gave an rms energy spread of 11.7 %, rms ct of 1.3 m, and contained 0.305 muons per incident proton.

TABLE III. Parameters of Phase Rotation Linacs

Linac	Length (m)	Frequency (MHz)	Gradient (MeV/m)
1	3	60	5
2	29	30	4
3	5	60	4
4	5	37	4

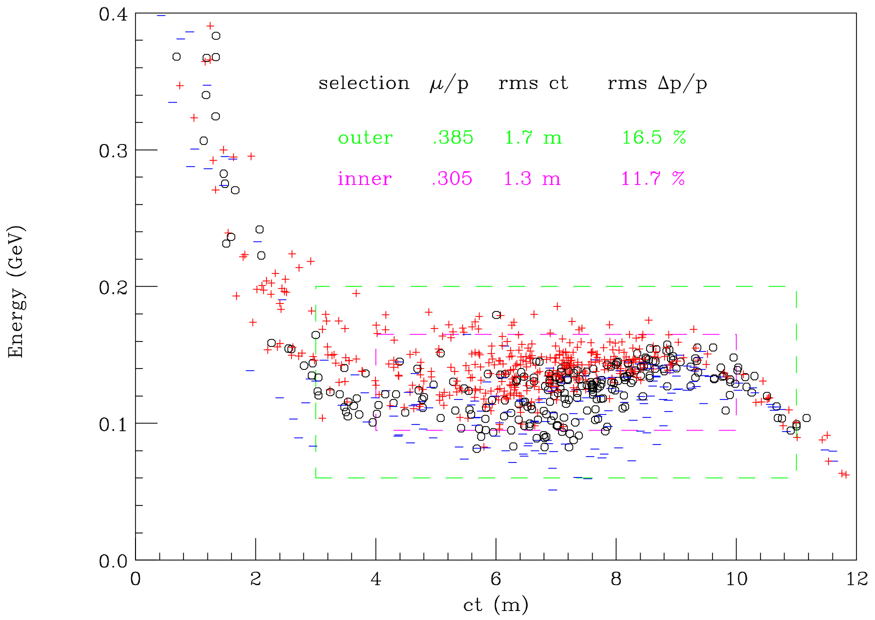

FIG. 6. Energy *vs.* ct of μ's at end of the Option-1 phase rotation channel. The symbols +, o and $-$ denote muons with polarization $P > \frac{1}{3}$, $-\frac{1}{3} < P < \frac{1}{3}$ and $P < -\frac{1}{3}$, respectively.

2. Higher Energy, shorter bunch example

This example captures muons at a mean kinetic energy of 300 MeV, and is taken from a Monte Carlo study [50] using the updated MARS pion production models and, in some examples, initial cooling by shaped absorbers in the rf rotation channel. Figure 7 shows a sample result, displaying the longitudinal phase space at the end of a 90 m (30-90 MHz) system. In this example, $\approx 0.27\,\mu's$ per 16 GeV protons are obtained within a beam which has transverse emittances of 0.01 m-rad (normalized), a bunch length of 1.5 m and energy width of 50 MeV with an average kinetic energy of ≈ 300 MeV. Higher frequency systems obtain fewer, higher energy muons, but with a shorter bunch length.

E. Use of Both Signs

Protons on the target produce pions of both signs, and a solenoid will capture both, but the required subsequent phase rotation rf systems will have opposite effects on each. The baseline solution is to use two proton bunches, aim them at the same target one after the other, and adjust the rf phases such as to act correctly on one sign of the first bunch and on the other sign of the second.

A second possibility would be to separate the charges into two channels, and phase rotate them separately. However, the separation, probably using a bent solenoid, is not simple and would not be fully efficient. Whether a gain in overall efficiency could be achieved is not yet known.

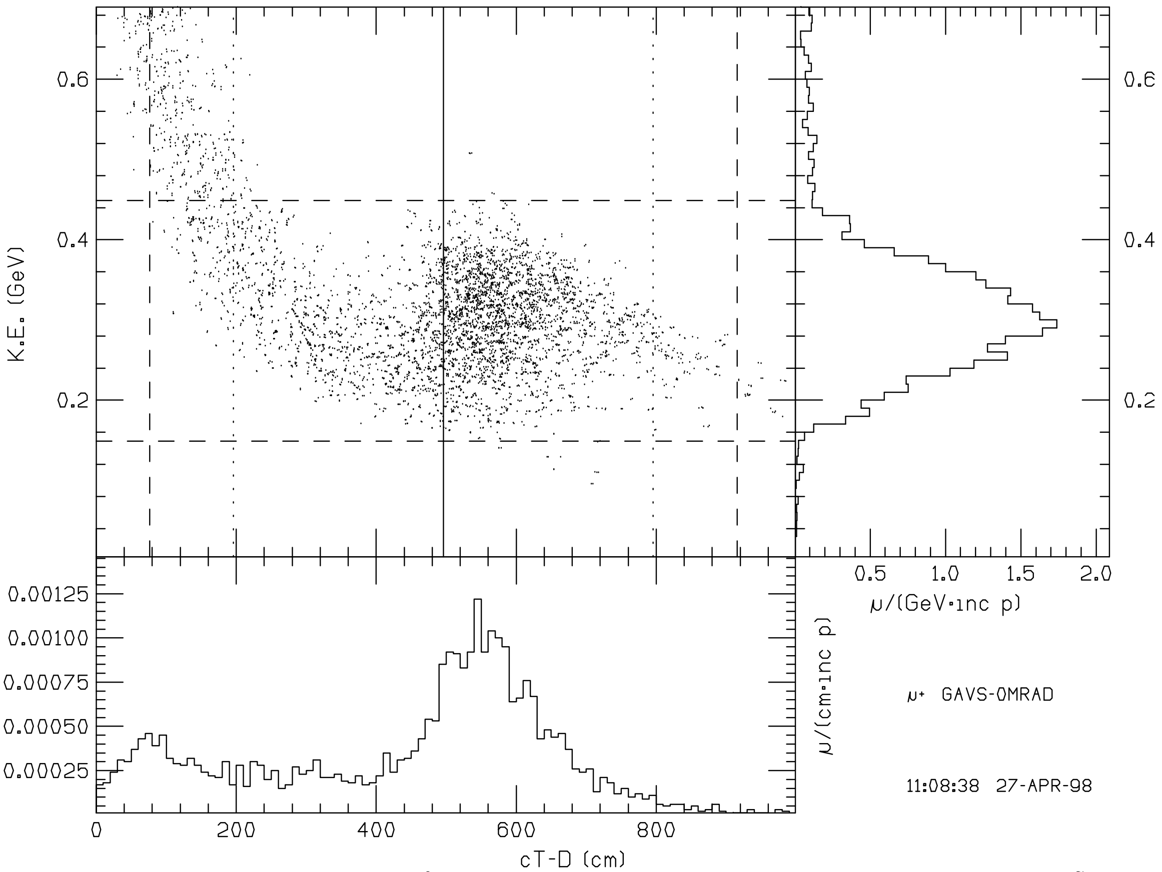

FIG. 7. Longitudinal phase space at the end of decay channel with projections onto time and energy axes. Solid vertical line corresponds to arrival time which receives no acceleration, dotted lines on either side indicate maximum acceleration (right) and deceleration (left). The four dashed lines delineate region deemed acceptable for the cooling channel.

F. Solenoids and RF

As noted above, capture using higher frequencies appears to be less efficient, and most studies now use frequencies down to 30 MHz. Such cavities, when conventionally designed, are very large (about 6.6 m diameter). In the Snowmass study [51] a reentrant design reduced this diameter to 2.52 m, but this is still large, and it was first assumed that the 5 T focusing solenoids would, for economic reasons, be placed within the irises of the cavities (see Fig. 8). But it has a problem that is not included in the above simulations.

A study [52] of transmission down a realistic system of iris-located coils revealed betatron resonant excitation from the magnetic field periodicities, leading to significant particle loss. This was reduced by the use of more complicated coil shapes [51], smaller gaps, and shorter cavities, but remained a problem.

An alternative is to place continuous focusing coils outside the cavities (as shown in Fig. 3). In this case cost will be minimized with lower magnetic fields (1.25 - 2.5 T) and correspondingly larger decay channel radii (21 - 30 cm). Studies are underway to determine the optimal solution.

G. Polarization

Polarization of the muon beams presents a significant advantage over the unpolarized case, since signal and background usually come predominantly from different polarization states.

1. Polarized Muon Production

In the center of mass of a decaying pion, the outgoing muon is fully polarized (-1 for μ^+ and +1 for μ^-). In the lab system the polarization depends [53–55] on the decay angle θ_d and initial pion energy. For pion kinetic energy larger

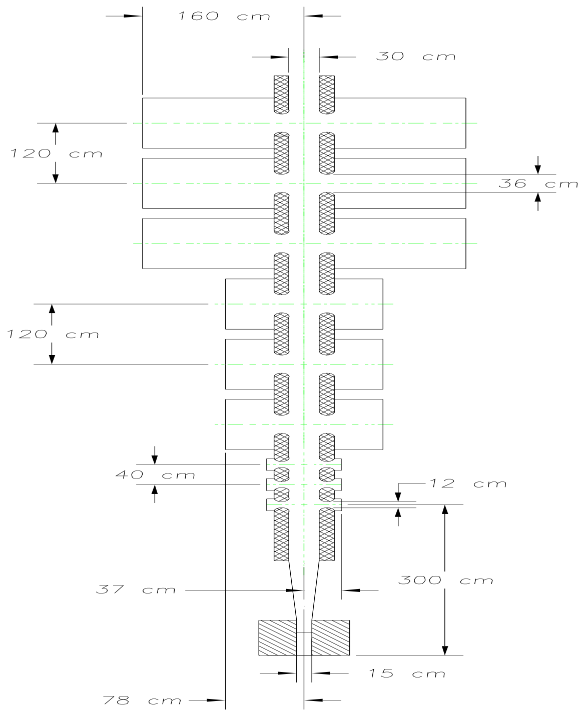

FIG. 8. Schematic of capture and phase rotation using rf cavities with superconducting solenoids (hatched) inside the irises. Only three sections each are shown for cavities operating at 90, 50, and 30 MHz

than the pion mass, the average is about 20 %, and if nothing else is done, the polarization of the captured muons after the phase rotation system is approximately this value.

If higher polarization is required, some selection of muons from forward pion decays ($\cos\theta_d \to 1$) is required. Figure 6, above, showed the polarization of the phase rotated muons. The polarization {P$> \frac{1}{3}$, $-\frac{1}{3} < P < \frac{1}{3}$, and P$< -\frac{1}{3}$} is marked by the symbols +, **o** and − respectively. If a selection is made on the minimum energy of the muons, then greater polarization is obtained. The tighter the cut, the higher the polarization, but the less the fraction F_{loss} of muons that is selected. Figure 9 gives the results of a Monte Carlo study.

If this selection is made on both beams, and if the proton bunch intensity is maintained, then each muon bunch is reduced by the factor F_{loss} and the luminosity would fall by F_{loss}^2. But if, instead, proton bunches are merged so as to obtain half as many bunches with twice the intensity, then the muon bunch intensity is maintained and the luminosity (and repetition rate) falls only as F_{loss}.

One also notes that the luminosity could be maintained at the full unpolarized value if the proton source intensity could be increased. Such an increase in proton source intensity in the unpolarized case would be impractical because of the resultant excessive high energy muon beam power, but this restriction does not apply if the increase is used to offset losses in generating polarization.

2. Polarization Preservation

A paper [56] has discussed the preservation of muon polarization in some detail. During the ionization cooling process the muons lose energy in material and have a spin flip probability $\mathcal{P}$,

$$\mathcal{P} \approx \int \frac{m_e}{m_\mu} \beta_v^2 \frac{dE}{E}, \tag{1}$$

where β_v is the muon velocity divided by c, and $\frac{\Delta E}{E}$ is the fractional loss of energy due to ionization. In our case the integrated energy loss is approximately 3 GeV and the typical energy is 150 MeV, so the integrated spin flip

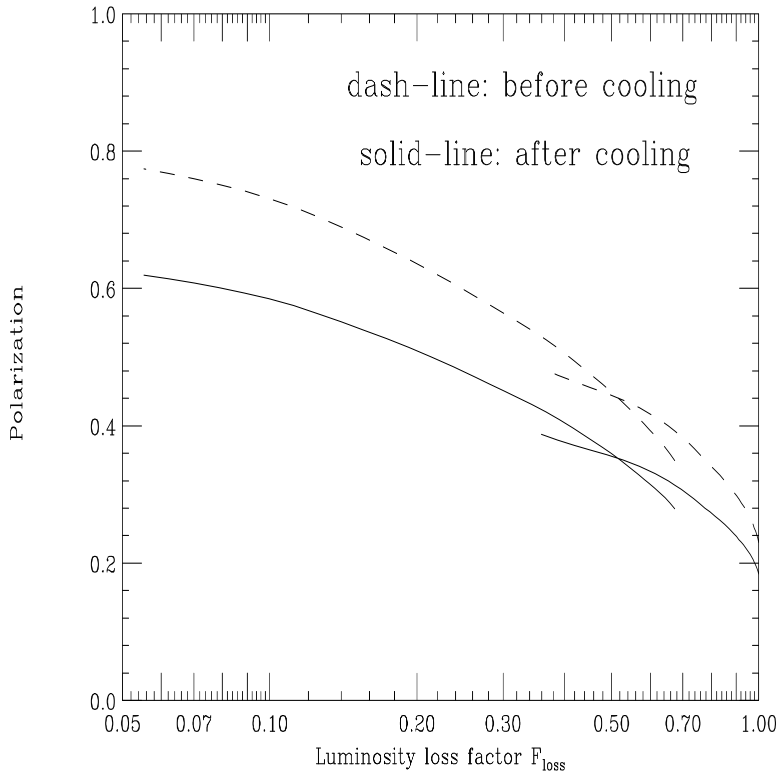

FIG. 9. Polarization *vs.* fraction F_{loss} of μ's accepted.

probability is close to 10 %. The change in polarization $\frac{\Delta \mathcal{P}}{\mathcal{P}}$ is twice the spin flip probability, so the reduction in polarization is approximately 20 %. This loss is included in Fig. 9.

During circulation in any ring, the muon spin, if initially longitudinal, will precess by $(g-2)/2\gamma$ turns per revolution, where $(g-2)/2$ is 1.166×10^{-3}. A given energy spread $\frac{\Delta\gamma}{\gamma}$ will introduce variations in these precessions and cause dilution of the polarization. But if the particles remain in the ring for an exact integer number of synchrotron oscillations, then their individual average γ's will be the same and no dilution will occur.

In the collider, bending can be performed with the spin orientation in the vertical direction, and the spin rotated into the longitudinal direction only for the interaction region. The design of such spin rotators appears relatively straightforward, but long. This might be a preferred solution at high energies but is not practical, in the 100 GeV machine. An alternative is to use such a small energy spread, as in the Higgs factory, that although the polarization vector precesses, the beam polarization does not become significantly diluted.

H. R&D Program

An R&D program is underway to clarify several critical issues related to targetry and phase rotation. A jet of the room-temperature eutectic liquid alloy of Ga-In will be exposed to nanosecond pulses of 1.5×10^{13} 24-GeV protons at the F.E.B. U-line of the Brookhaven AGS to study the effect of the resulting pressure wave on the liquid. The same jet will also be used in conjunction with a 20 T, 20 cm bore resistive magnet at the National High Magnetic Field Laboratory (Tallahassee, FL) to study the effect of eddy currents on jet propagation. Then, a pulsed, 20 T magnet will be added to the BNL test station to explore the full configuration of jet, magnet and pulsed proton beam. Also, a 70 MHz rf cavity will be exposed to the intense flux of secondary particles downstream of the target and 20 T magnet to determine viable operating parameters for the first phase rotation cavity.

The first two studies should be accomplished during 1999, and the third and fourth in the years 2000/01.

V. IONIZATION COOLING

A. Introduction

The muon beam at the end of the decay channel is very intense, but diffuse in phase space. For a high luminosity collider, the phase-space volume of the muon beam must be reduced within a time of the order of the μ lifetime $\approx 2\ \mu s$. This requires the development of a new method for beam cooling.

Cooling by synchrotron radiation, conventional stochastic cooling and conventional electron cooling are all too slow. Optical stochastic cooling [57], electron cooling in a plasma discharge [58] and cooling in a crystal lattice [59,60] are being studied, but appear technologically difficult. Ionization cooling [61–63] of muons seems relatively straightforward, and it is unique for muons.

Ionization cooling involves passing the beam through some material in which the muons lose both transverse and longitudinal momentum by ionization loss (dE/dx). The longitudinal muon momentum is then restored by reacceleration, leaving a net loss of transverse momentum (transverse cooling). The process is repeated many times to achieve a large cooling factor.

The energy spread can also be reduced (longitudinal emittance exchange) by introducing a transverse variation in the absorber density or thickness (e.g. a wedge) at a location where there is dispersion (the position is energy dependent). This method results in an a corresponding increase of transverse momentum and is thus not true cooling, but an exchange of longitudinal and transverse emittances that, with transverse cooling, allows cooling in all dimensions.

The appropriate figure of merit for cooling is the final value of the 6-D relativistically invariant emittance ϵ_6 – the area in the 6-dimensional phase space (x, y, z, p_x, p_y, p_z)– since, to a fairly good approximation, it is preserved during acceleration and storage in the collider ring. Theoretical studies have shown that, assuming realistic parameters for the cooling hardware, ionization cooling can be expected to reduce the phase-space volume occupied by the initial muon beam by a factor of $10^5 - 10^6$. A complete cooling channel would consist of $20 - 30$ cooling stages, each stage yielding about a factor of two in phase-space reduction.

It is recognized that the feasibility of constructing a muon ionization cooling channel is on the critical path to understanding the viability of the whole muon collider concept. The muon cooling channel is the most novel part of a muon collider complex. Steady progress has been made both in improving the design of the channel and in adding detail to the computer simulations. We are now close to the goal of having a detailed and complete simulation of an entire cooling channel. A vigorous experimental program is needed to verify and benchmark the computer simulations.

In the following parts of this section we will briefly describe the physics underlying the process of ionization cooling, we will show results of simulations for some chosen examples and mention a six year R&D program to demonstrate the feasibility of using ionization cooling techniques to reduce the 6-dimensional phase space emittance.

B. Cooling Theory

In ionization cooling, the beam loses both transverse and longitudinal momentum as it passes through a material medium. At the same time its emittance is increased due to stochastic multiple scattering and Landau straggling. Subsequently, the longitudinal momentum can be restored by reacceleration, leaving a net loss of transverse momentum.

The approximate equation for transverse cooling (with energies in GeV) is

$$\frac{d\epsilon_n}{ds} = -\frac{1}{\beta^2}\frac{dE_\mu}{ds}\ \frac{\epsilon_n}{E_\mu} + \frac{\beta_\perp (0.014)^2}{2\beta^3 E_\mu m_\mu\ L_R}, \tag{2}$$

where ϵ_n is the normalized transverse emittance, $\beta_\perp$ is the betatron function at the absorber, dE_μ/ds is the energy loss, and L_R is the radiation length of the material. The first term in this equation is the cooling term, and the second is the heating due to multiple scattering. This heating term is minimized if $\beta_\perp$ is small (strong-focusing) and L_R is large (a low-Z absorber).

The equation for energy spread (longitudinal emittance) is:

$$\frac{d(\Delta E_\mu)^2}{ds} \ = -2\ \frac{d\left(\frac{dE_\mu}{ds}\right)}{dE_\mu} < (\Delta E_\mu)^2 > \ + \frac{d(\Delta E_\mu)^2_{\rm straggling}}{ds} \tag{3}$$

where the first term is the cooling (or heating) due to energy loss, and the second term is the heating due to straggling.

Energy spread can be reduced by artificially increasing $\frac{d(dE_\mu/ds)}{dE_\mu}$ by placing a transverse variation in absorber density or thickness at a location where position is energy dependent, i.e. where there is dispersion. The use of such wedges can reduce energy spread, but it simultaneously increases transverse emittance in the direction of the dispersion. Six dimensional phase space is not reduced, we only exchange longitudinal phase space with transverse phase space.

Ionization cooling of muons seems relatively straightforward in theory, but will require extensive simulation studies and hardware development for its optimization. There are practical problems in designing lattices that can transport, and focus the large emittance beam. There will also be effects from space charge and wake fields.

We have developed a number of tools for studying the ionization cooling process. First, the basic theory was used to identify the most promising beam properties, material type and focusing arrangements for cooling. Given the practical limits on magnetic field strengths, this gives an estimate of the minimum achievable emittance for a given configuration. Next, the differential equations for cooling and heating described above have been incorporated into a computer code. Allowance for the shifts in the betatron phase advance due to space charge and aberrations was included. This code was used to develop an overall cooling scenario, which broke the cooling system into a number of stages, and determined the properties of the beam, rf, and focusing lattice at each stage [64].

Finally, several tracking codes were either written or modified to study the cooling process in detail. Two new codes (SIMUCOOL [65], and ICOOL [66]) use Monte Carlo techniques to track particles one at a time through the cooling system. All the codes attempt to include all relevant physical processes to some degree, e.g. energy loss, straggling, multiple scattering, and to use Maxwellian models of the focusing fields. They do not yet take into account any space charge or wake field effects. In addition, we have also used a modified version of PARMELA [67] for tracking, which does include space charge effects, and a double precision version of GEANT. [68,69] All of these codes are continually being updated and optimized for studying the cooling problem.

C. Cooling System

The cooling is obtained in a series of cooling stages. Each stage consists of a succession of two components:

1. Transverse cooling sections using materials in a strong focusing (low$\beta_\perp$) environment alternated with linac accelerators.

2. Emittance exchange in lattices that generate dispersion, with absorbing material wedges to reduce momentum spread.

In the examples that follow it is seen that each such stage lowers the 6 dimensional emittance by a factor of about 2. Since the required total 6 dimensional cooling is about 10^6, about 20 such stages are required. The total length of the system would be of the order of 500 m, and the total acceleration would be approximately 6 GeV. The fraction of muons remaining at the end of the cooling system is estimated to be $\approx 60\%$.

The baseline solution for transverse cooling involves the use of liquid hydrogen absorbers in strong solenoid focusing fields, interleaved with short linac sections. The solenoidal fields in successive absorbers are reversed to avoid build up of the canonical angular momentum. The focusing magnetic fields are small (≈ 1 T) in the early stages where the emittances are large, but must increase as the emittance falls.

Two transverse cooling examples have been designed and simulated. The first would lie toward the end of a full cooling sequence and uses 15 T solenoids. The second, using 31 T solenoids, meets the requirements for the Higgs factory and could be the final cooling stage for this machine.

The baseline solution for emittance exchange involves the use of bent solenoids to generate dispersion and wedges of hydrogen or LiH to reduce the energy spread. A simulated example is given for exchange that would be needed after the 15 T transverse cooling case.

A lithium lens solution may prove more economical for the final stages, and might allow even lower emittances to be obtained. In this case, the lithium lens serves simultaneously to maintain the low $\beta_\perp$, and attenuate the beam momenta. Similar lenses, with surface fields of 10 T, were developed at Novosibirsk (BINP) and have been used, at low repetition rates, as focusing elements at FNAL and CERN [70–74]. Lenses for the cooling application, which would operate at 15 Hz, would need to employ flowing liquid lithium to provide adequate cooling. Higher surface fields would also be desirable.

Studies [75] have simulated cooling in multiple lithium lenses, and have shown cooling through several orders of magnitude. But these studies have, so far, used ideal matching and acceleration. Further studies are underway.

Cooling in beam recirculators could lead to reduction of costs of the cooling section [76], but again, full simulations with all higher order effects have not yet been successfully achieved.

D. 15 T Solenoid Transverse Cooling Example

The lattice consists of 11 identical 2 m long *cells*. In each cell there is a liquid hydrogen absorber (64 cm long, 10 cm diameter) in the 15 T solenoid focusing magnet (64 cm long, 12 cm diameter). The direction of the fields in the magnets alternates from one cell to the next. Between the magnets there are magnetic matching sections (1.3 m long, 32 cm inside diameter) where the field is lowered and then reversed. Inside the matching sections are short 805 MHz high gradient (36 MeV/m) linacs. Figure 10 shows the cross section of one cell of such a system, together with the beta function, and the magnetic field along the axis.

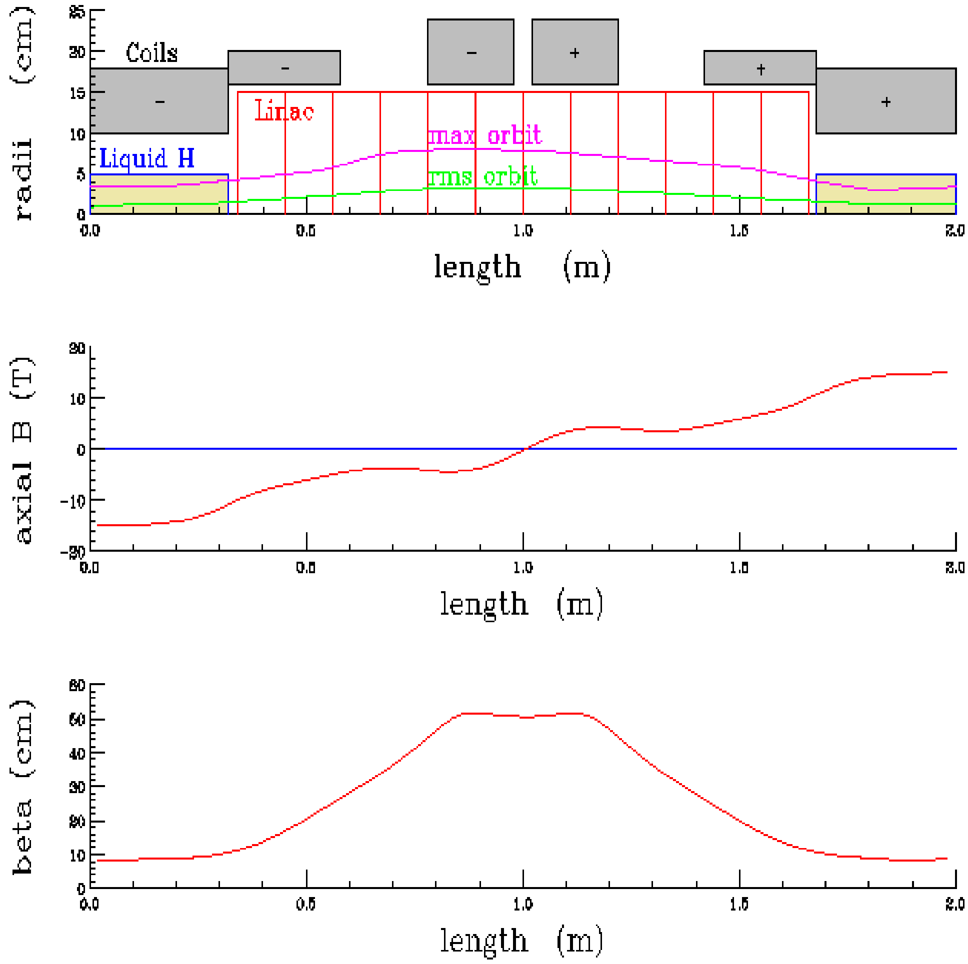

FIG. 10. a) Cross section of one cell of an alternating solenoid cooling system; b) axial magnetic field *vs.* z; c) beta function *vs.* z.

The simulations were performed using the program ICOOL [66]; the only effects which are not yet included are space charge and wake fields. Analytic vacuum calculations indicate that these effects should, for the later stages be significant, but not overwhelming, but a correct simulation must be done before we are assured that no significant problems exist. Particles are introduced with transverse and longitudinal emittance (186 MeV/c, 1400 π mm mrad transverse, and 1000 π mm longitudinal), together with a number of naturally occuring correlations: 1) the angular momentum appropriate for the starting axial magnetic field, 2) a correlation between momentum and amplitude squared to give forward velocities independent of amplitude, and 3) a distortion of the longitudinal bunch distribution to reflect the asymmetric nature of the alpha rf bucket.

Figure 11(a) shows the average momentum of the beam as it falls in the hydrogen absorbers and rises in the linacs. Figure 11(b) shows the average angular momentum, and (dashed) the canonical angular momentum, as they oscillate between positive and negative values in the reversing axial fields.

Figure 12(a) shows the rms and maximum radii of the beam as they rise and fall in the varying axial magnetic fields. Figure 12(b) shows the rms momentum corrected for the amplitude-momentum correlation. Figure 12(c) shows the rms bunch length.

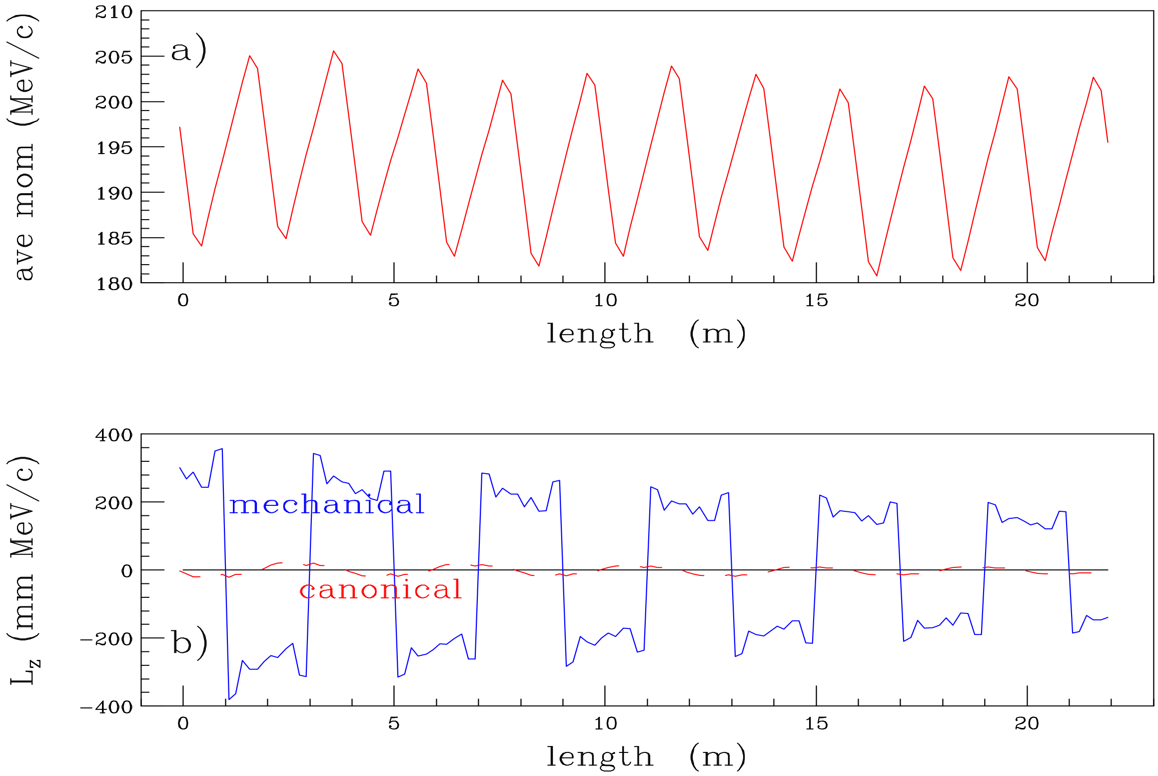

FIG. 11. a) average momentum vs. length; b) average angular momentum: mechanical (solid curve) and canonical (dashed curve), vs. length.

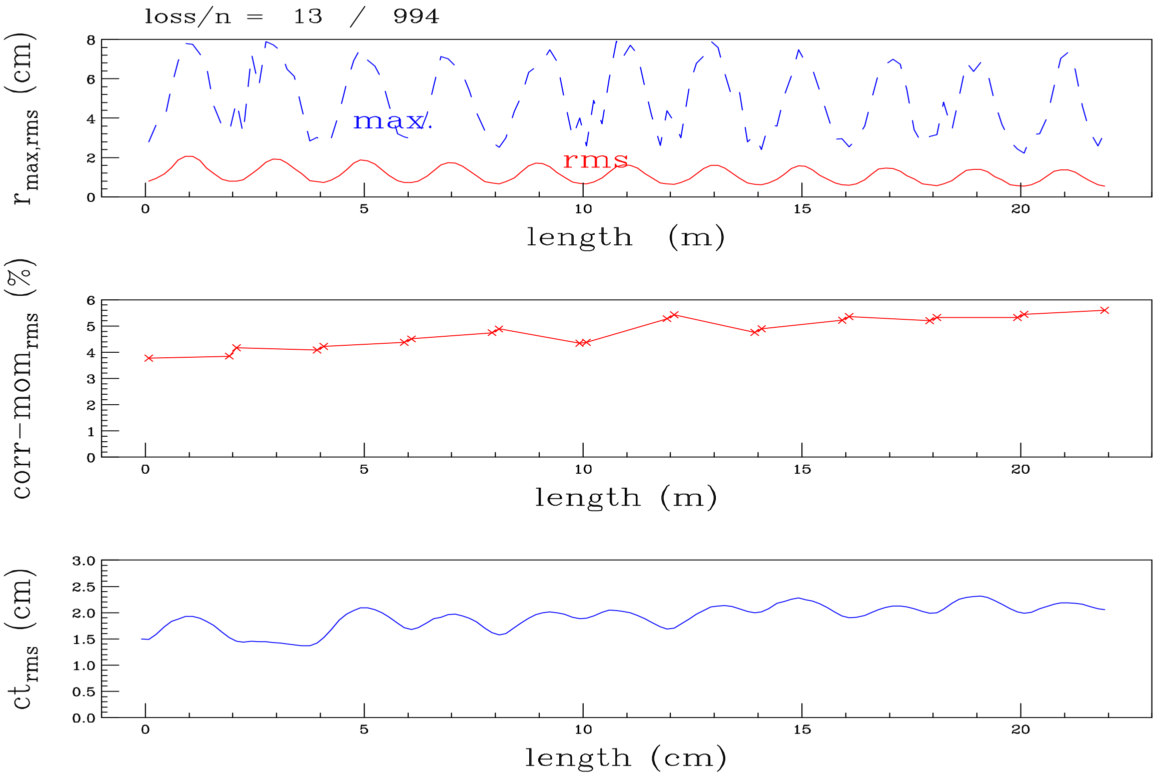

FIG. 12. a) rms and maximum beam radii, b) rms corrected momentum, c) rms bunch length; all vs. length.

Figure 13(a) shows the reduction of transverse emittance; Figure 13(b) shows the increase in longitudinal emittance induced by straggling and the adverse dependence of dE/dx with energy; Figure 13(c) shows the overall reduction in 6-dimensional emittance. Table IV gives the initial and final parameters.

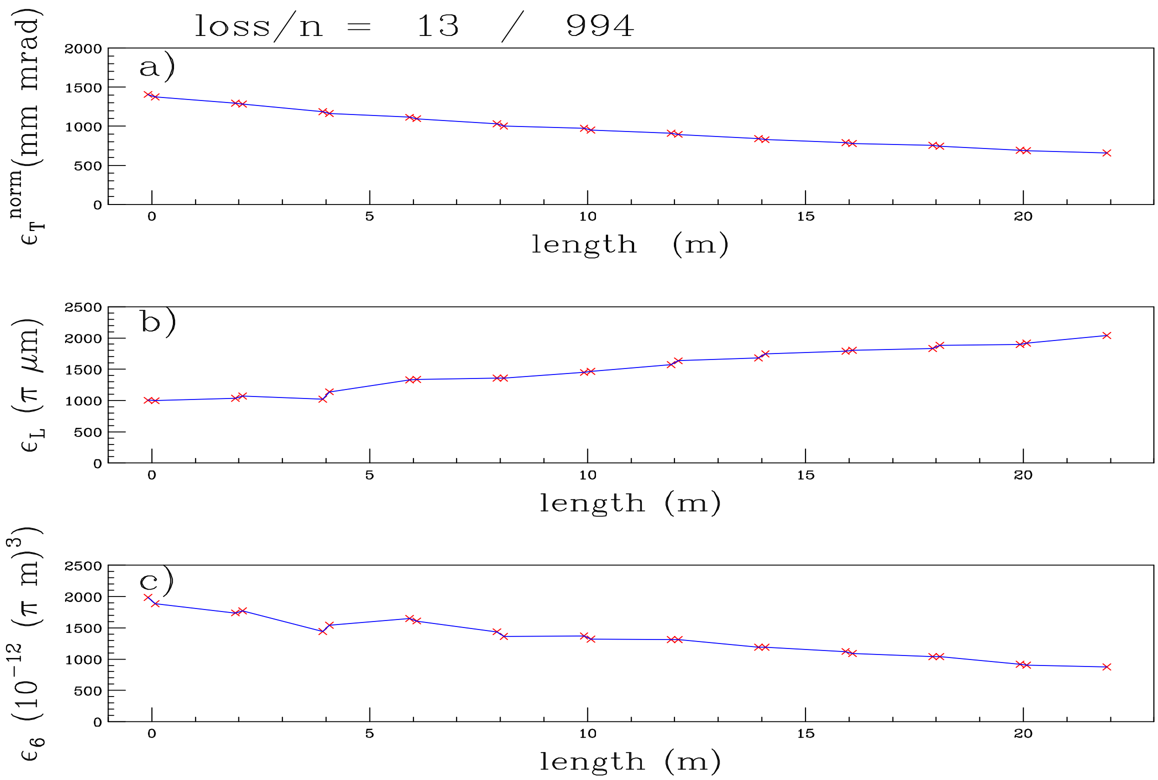

FIG. 13. emittance vs. length:a) transverse emittance; b)longitudinal emittance; and c) 6-dimensional emittance.

TABLE IV. Initial and final beam parameters in a 15 T transverse cooling section.

		initial	final	factor
Particles tracked		1000	980	98%
Transverse Emittance	π mm mrad	1400	600	0.43
Longitudinal Emittance	π mm mrad	1100	2300	2.09
6D emittance	10^{-12} $\times$ $(\pi\ m\ rad)^3$	2000	800	0.40
rms beam size in hydrogen	cm	0.8	0.55	0.69
rms beam size in linac	cm	2.0	1.4	0.70
max beam rad in linac	cm	7.0	7.0	1.0
rms bunch length	cm	1.5	2.2	1.5
max bunch full width	cm	13	19	1.5
rms dp/p	%	3.8	5.6	1.5

This simulation has been confirmed, with minor differences, by the codes double precision GEANT [69] and PARMELA [67].

E. 31 T Solenoid Transverse Cooling Example

As above, the lattice consists of 11 identical 2 m long *cells*. The maximum fields are higher (31 T) but the bore smaller (8 cm). The liquid hydrogen absorber is slightly shorter then in the previous case (64 cm long, 6 cm diameter). As before, the direction of the fields in the magnets alternates from one cell to the next. Between the magnets there are again magnetic matching sections (1.3 m long, 32 cm inside diameter) and the rf is also the same (805 MHz, 36 MeV/m).

Table V gives the initial and final parameters for the 31 T example, together with the required emittances for a Higgs factory. In setting these requirements a dilution of 20 % is assumed in each of the three emittances.

TABLE V. Initial and final beam parameters in a 31 T transverse cooling section.

		initial	final	factor	Req.
Particles tracked		4000	3984	99.6%	
Transverse Emittance	π mm mrad	460	240	0.52	240
Longitudinal Emittance	π mm mrad	850	1600	1.9	
6D emittance	$10^{-12} \times (\pi\ m\ rad)^3$	150	95	0.63	98
rms beam size in hydrogen	cm	0.44	0.33	0.75	
rms beam size in linac	cm	1.4	1.1	0.80	
max beam rad in linac	cm	6.0	6.0	1.0	
rms bunch length	cm	1.5	1.8	1.2	
max bunch full width	cm	11	19	1.7	
rms dp/p	%	3.5	5.0	1.4	

F. Bent Solenoid Emittance Exchange Example

The exchange of longitudinal and transverse emittance requires dispersion in a large acceptance channel, followed by low Z wedge absorbers. In this example, the lattice consists of a continuous (3.5 T) solenoid and dispersion is generated by bending the solenoid.

In a bent solenoid, in the absence of any dipole field, there is a drift perpendicular to the bend that is proportional to the particle's momentum. In this lattice, a uniform dipole field is introduced over the bend to exactly cancel this drift for particles with the reference momentum. Particles above and below this reference momentum then drift up or down, depending on their momentum, giving the required dispersion (0.4 m). The dispersion is removed, and the momentum spread reduced, by introducing liquid hydrogen wedges. The hydrogen wedges would be contained by thin beryllium or aluminum foils, but these were not included in this simulation.

After one bend and one set of wedges, the beam is asymmetric in cross section. Symmetry is restored by a following bend and wedge system rotated by 90 degrees with respect to the first. Figure 14 shows a representation of the two bends and wedges. The total solenoid length was 8.5 m. The beam tube outside diameters are 20 cm, and the minimum bend radii 34 cm.

Figure 15(a) shows the magnetic fields (B_z, B_y, and B_x) as a function of the position along the cell. The solenoid bend curvature is exactly that given by the trajectory of a reference particle (equal in momentum to the average momenta given in Fig. 15(b)) in the given transverse fields. It is seen that the onset and end of the bend curvatures is not sudden: the shape is chosen to minimize emittance growth.

The simulations were performed using the program ICOOL [66]. The maximum beam radius is 10 cm. Transmission was 100 %. Figure 16(a) shows the rms longitudinal momentum relative to the reference momentum as a function of the position along the cell. It decreases from an initial value of approximately 5%, to a final value of approximately 2.2%. At the same time, since this is an emittance exchange, the transverse beam area grows, as shown in Fig. 16(b). One notes that the area increases not only in the regions of bends (region 1 and 8), but also in the regions of wedges (2-6 and 9-11). This is probably due to failures in matching that have yet to be understood.

Figure 17 shows scatter plots of the transverse particle positions against their momenta: a) y-p at the start, b) y-p after the first bend c) y-p after the first set of wedges, d) x-p after the first wedges, e) x-p after the second bend, and f) at the end. The dispersion is clearly observed in Fig. 17(b) (after the first bend) and in Fig. 17(e) (after the second). It is seen to be removed, with a corresponding decrease in momentum spread, in Fig. 17(c) (after the first set of wedges) and Fig. 17(f) (after the second set of wedges).

Figure 18 shows a scatterplot of the particle squared radii vs. their longitudinal momentum, Figure 18(a) at the start, and Figure 18(b) at the end. The decrease in momentum spread and rise in beam area are clearly evident.

The initial and final beam parameters are given in Tb. VI. The example was not well optimized. There are significant final beam fluctuations, presumably due to mismatching, and some of the 37% rise in 5 dimensional phase space may be from this cause. RF must be included to allow the 6 dimensional emittance to be studied. Significantly more work is needed to further optimize the emittance exchange section.

Emittance exchange in solid LiH wedges, with ideal dispersion and matching, has also been successfully simulated [77] using SIMUCOOL [78]. Dispersion generation by weak focusing spectrometers [76] and dipoles with solenoids [79] have also been studied.

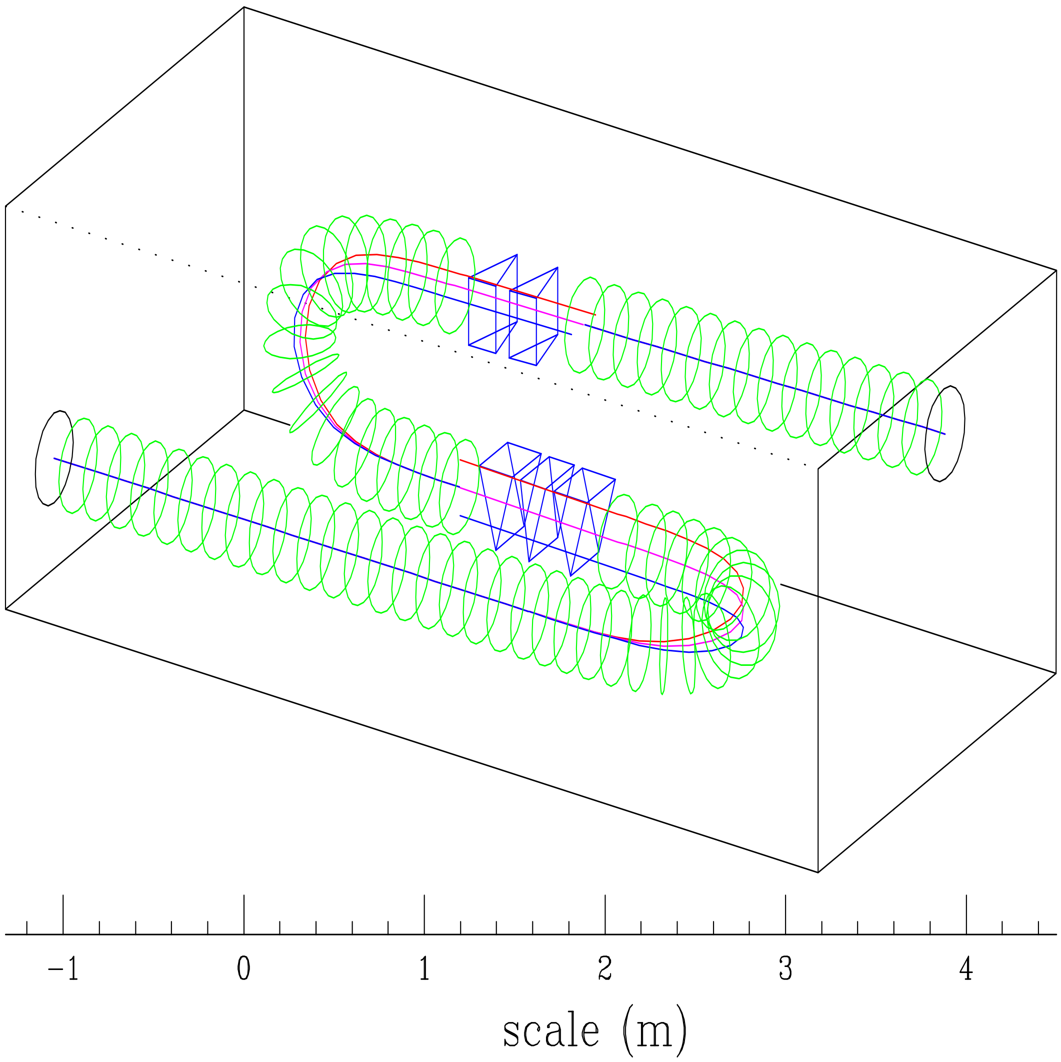

FIG. 14. Representation of a bent solenoid longitudinal emittance exchange section

TABLE VI. Initial and final beam parameters in a longitudinal emittance exchange section.

		initial	final	factor
Longitudinal Momentum spread	MeV/c	9.26	3.35	0.36
Ave. Momentum	MeV/c	180	150	0.83
Transverse size	cm	1.33	2.26	1.70
Transverse Momentum spread	MeV/c	6.84	7.84	1.15
Transverse Emittance	π mm mrad	870	1694	1.95
$\mathrm{Emit}^2_{trans} \times \Delta \mathrm{p}_{long}$	$(\pi$ m mrad$)^2$ MeV/c	7.0	9.6	1.37

G. RF for the Cooling Systems

RF acceleration sections are used to restore the longitudinal momentum of the muon beam after losses in the cooling media. These rf structures are embedded in solenoidal fields which reverse direction within each section. In the two transverse cooling examples, above, the rf frequency is 805 MHz and the peak gradient is 36 MeV/m. The focusing fields, which extend over the cavities, vary from 0 to 5 T, reversing in the center. It should be pointed out that in the earlier and later stages, the bunches are longer, and lower frequencies will be required.

In order to realize maximum acceleration gradients within the acceleration cavities, we take advantage of the penetrating properties of a muon beam by placing thin windows between each rf cell, thereby creating an accelerating

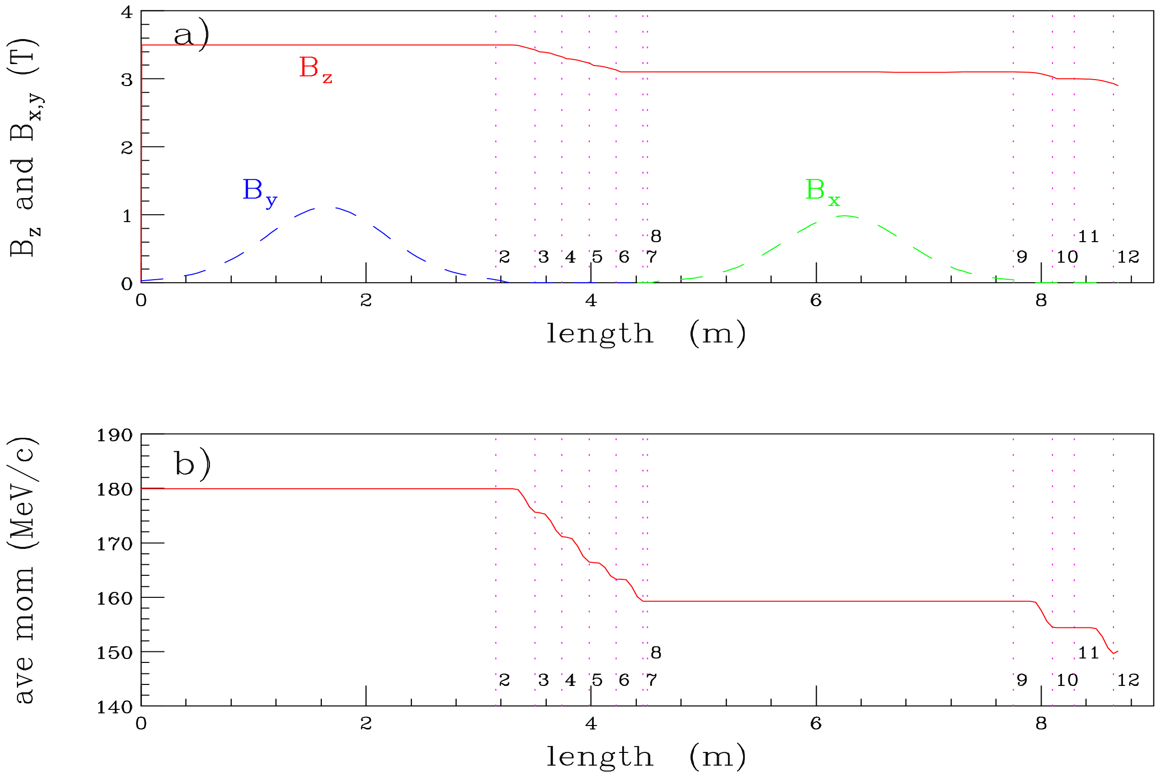

FIG. 15. a) Axial B_z and dipole B_y, B_x, magnetic fields; b) average momentum; both as a function of the position along the cell.

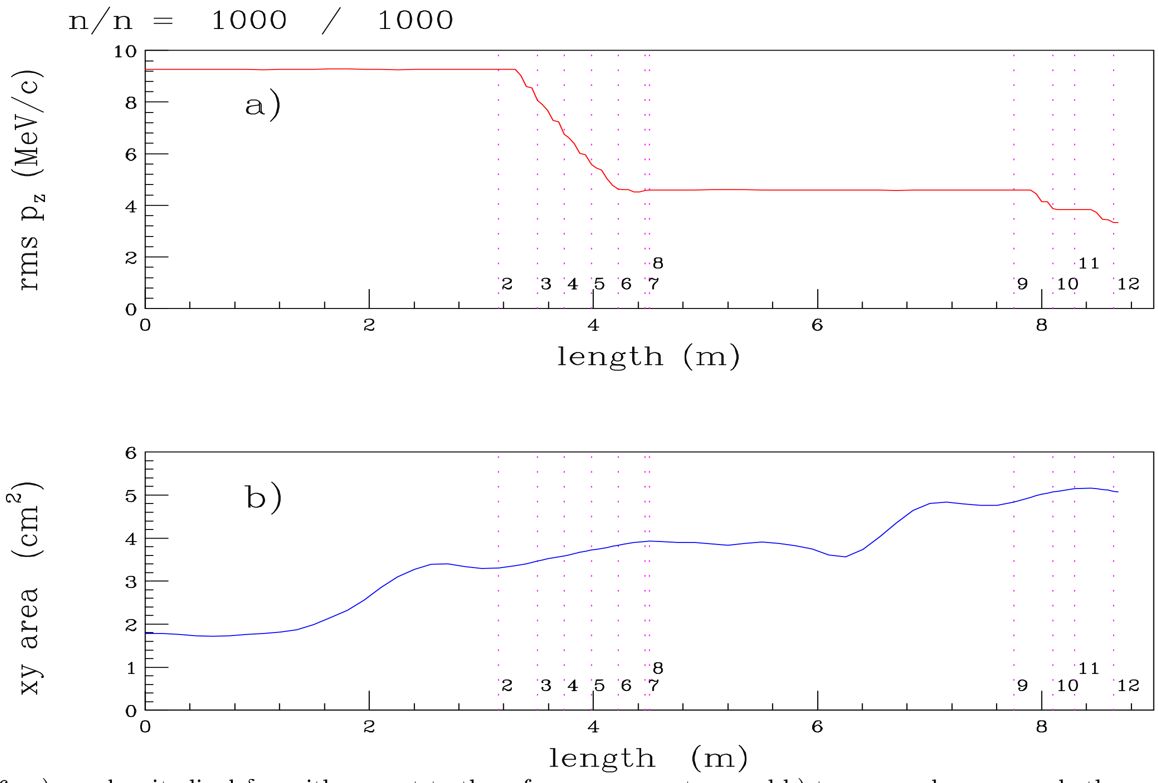

FIG. 16. a) rms longitudinal δp_z with respect to the reference momentum and b) transverse beam area, both as a function of length.

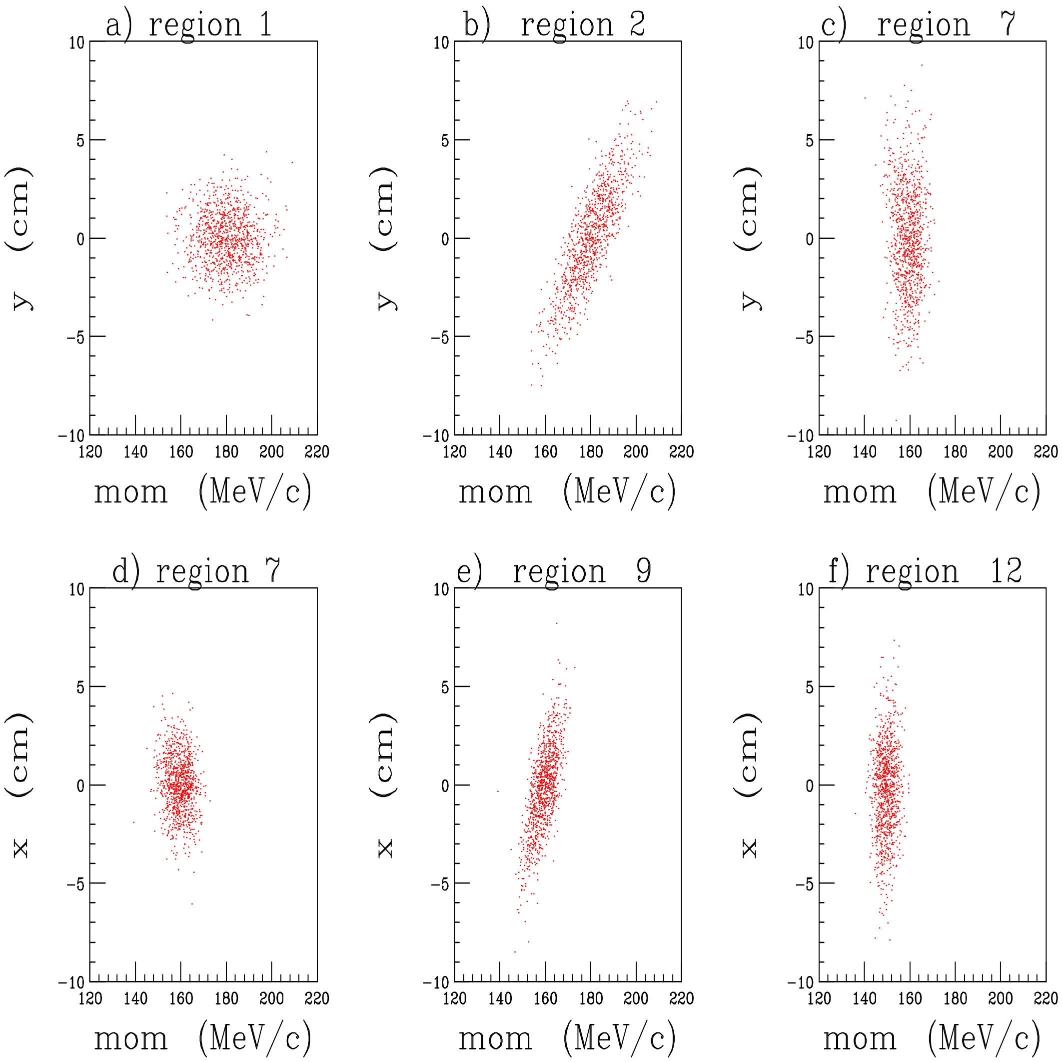

FIG. 17. y-p$_z$ plots: a) at the start, b) after the first bend, c) after the first set of wedges. x-p$_z$ plots: d) after the first wedges, e) after the second bend, and f) at the end

structure closely approximating the classic pill-box cavity. This permits operating conditions in which the axial accelerating field is equal to the maximum wall field and gives a high shunt impedance.

The windows in the 15 T example are 16 cm diameter, 125 μm thick Be foils. In the 31 T case, they are 10 cm diameter and 50 μm thick.

For these rf structures, we will use an interleaved cavity design in which two parts are independently powered (Fig. 19). The mode of the system will be referred to as $\pi/2$ interleaved. Each section supports a standing wave π mode, with each acceleration cell $\pi/2$ long, giving a good transit time factor. To reduce the peak rf power requirements (by a factor of 2) the cells may be operated at liquid nitrogen temperatures.

The characteristics of the rf systems currently being studied are summarized in Table VII. Figure 20 shows a full 1.3 m section with interleaved cavities. Each cell is 8.1 cm in length and the 1.3 m section consists of 16 cells.

H. Ionization Cooling Experiment

A proposal has been written [80], and submitted to the FNAL management, which describes a six-year research and development program to develop the hardware needed for ionization cooling, and demonstrate the feasibility of using the ionization cooling technique to produce cooled beams of positive and negative muons. It is proposed to design and prototype critical sections of the muon ionization cooling channel. These sections would be tested by measuring their performance when exposed to single incoming muons with momenta in the range 100 – 300 MeV/c. The phase-space

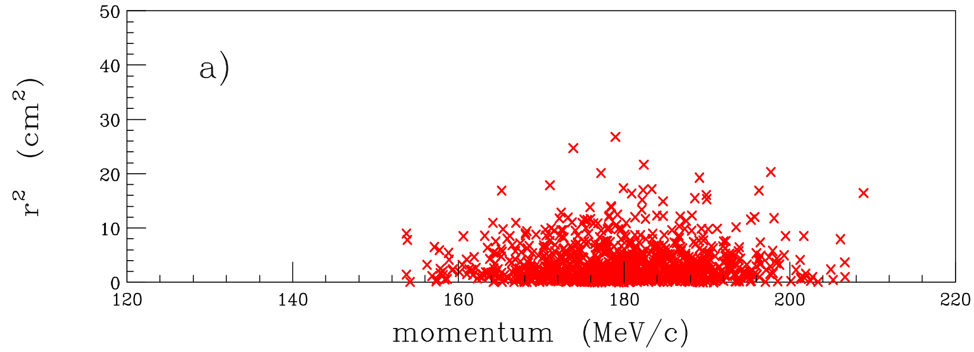

FIG. 18. Scatterplot of squared radii vs. longitudinal momentum a) at the start, and b) at the end.

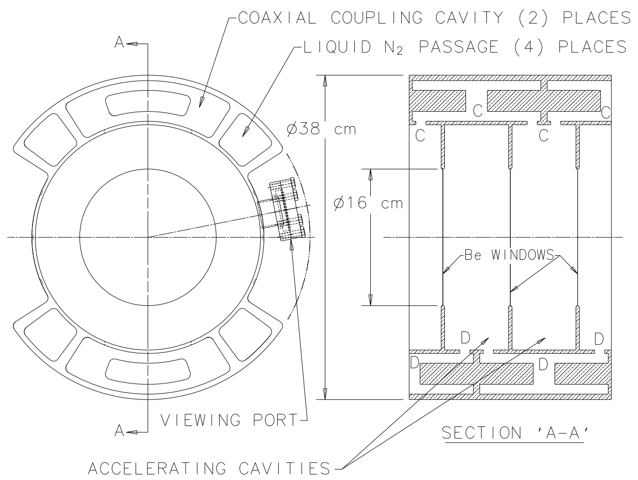

FIG. 19. Two full cell sections plus two half cell sections of the interleaved $\pi/2$ mode accelerating cavities. The volumes labeled **C** are powered separately from the volumes labeled **D**.

volume occupied by the population of muons upstream and downstream of the cooling sections would be measured sufficiently well [81] to enable cooling to be established, the calculations used to design the cooling system to be tested, and optimization of the cooling hardware to be studied. Figure 21 shows a schematic of the detector arrangement to measure the 6-dimensional phase space of the incoming and outgoing muons.

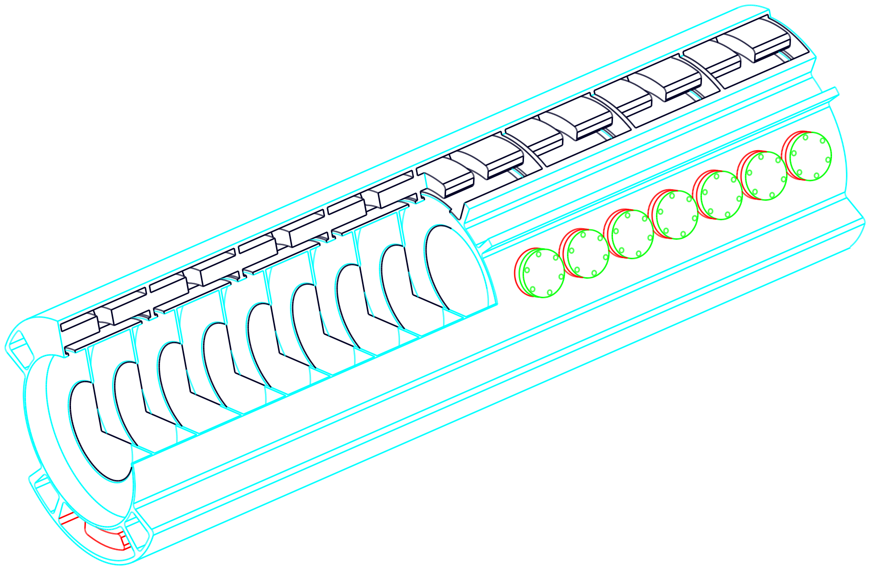

FIG. 20. A 1.3 m acceleration section with quarter section cut away for viewing the inter cavity windows.

TABLE VII. Characteristics of the rf system.

RF Cavity Parameters	
RF frequency [MHz]	805
Cavity Length [cm]	8.1
Cavity Inner Radius [cm]	14.65
Cavity Outer Radius [cm]	19
Q/1000	2×20
Peak Axial Gradient [MV/m]	30
Shunt Impedance [MΩ/m]	2×54
Zt^2 [MΩ/m]	2×44
Fill Time (3 τ) [μs]	26
RF Peak Power [MW/m]	16/2
Ave. Power (15Hz) [KW/m]	7/2
Be window aperture [cm]	16 (10 for 31 T case)
Be window thickness [μm]	127 (50 for 31 T case)

VI. ACCELERATION

A. Introduction

Following cooling and initial bunch compression, the beams must be rapidly accelerated. The acceleration needed for a Higgs collider is probably the most conventional part of the machine, and severe problems are not expected in its design, but far less work has gone into its study than into the other elements. No lattices have yet been designed and little simulation has been undertaken.

A sequence of linacs would work, but would be expensive. Some form of circulating acceleration is preferred. At the lowest energies (< 700 MeV) the momentum spread and beam sizes are so large that only a linac is possible. At intermediate energies (to ≈ 200 GeV) the acceleration time is so short that any form of magnet ramping is impractical. The conservative option here is to use a sequence of recirculating accelerators (similar to that used at TJNL), but Fixed Frequency Alternating Gradient (FFAG) accelerators are also being studied [82,83] (see next section). At higher energies, the acceleration rate is slow enough that fast rise time pulsed magnets are possible (see below).

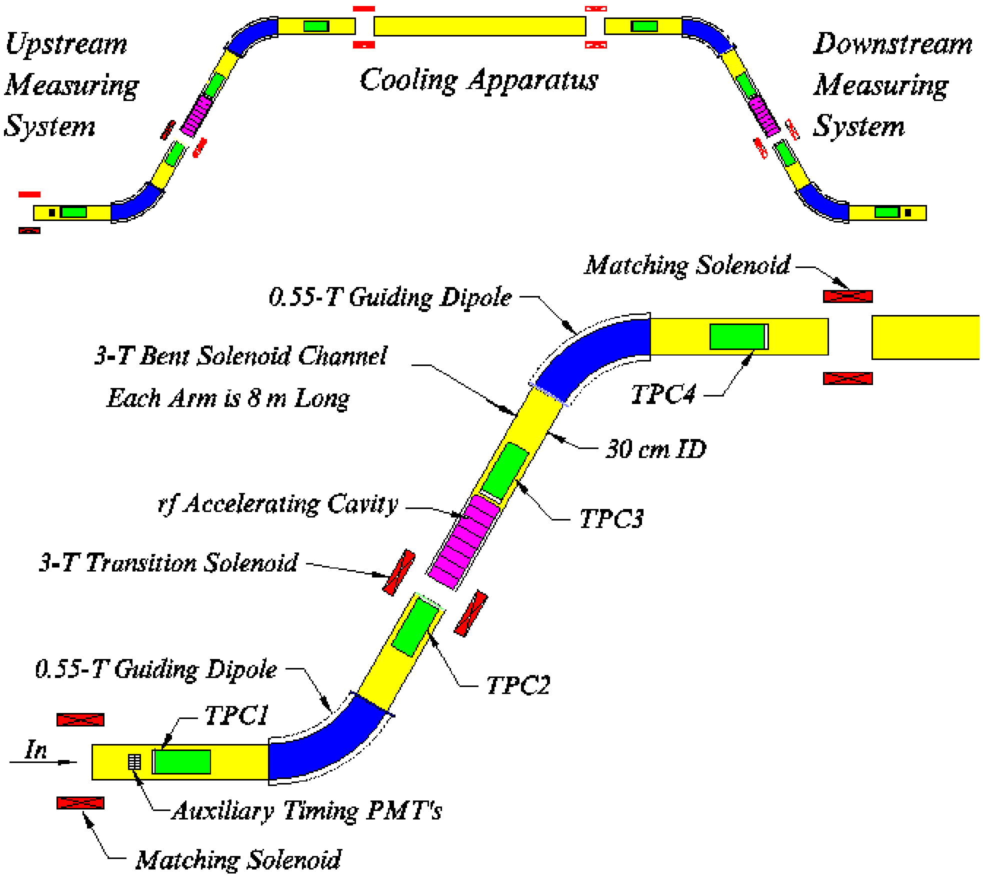

FIG. 21. Schematic of the cooling test apparatus arrangement.

B. Acceleration for Higgs Collider

Tb. VIII gives an early example of a sequences of accelerators for a 100 GeV Higgs Factory, i.e. a machine with the very low momentum spread (0.003 %) and relatively large *rms* transverse emittance ($\approx$ 300π mm mrad).

Following initial linacs, recirculating accelerators are used. The number of arcs in each recirculating accelerator is about 10. In this example, conventional 2 T magnets are used. The effective ramp frequencies that would be needed if pulsed magnets were used are given in the table.

Designs [84] have been made of multiple aperture superconducting magnets (see Fig. 7.12 in [20]) for use in this or higher energy machines. Their use would reduce the diameter of the recirculating accelerator ring and lower particle loss from decay and could be more economical.

Significant work [83,85] has also been done on Fixed Field Alternating Gradient (FFAG) lattices that could replace the multiple arcs (see next section).

In this example, all the accelerating cavities are room temperature copper structures, and the accelerating gradients are modest ($<$ 10 MeV/m). Nevertheless, the acceleration is rapid enough that the total losses from decay are only 30 %. The heating from these decays is also modest ($\approx$ 10 W/m) because of the small number of turns and relatively low energy. Since no superconducting magnets or rf are used in this example, this heating should cause no problem.

1. Design Issues

The first design challenge arises because of the large transverse emittances ($r$ms) ($\approx$ 300 π mm mrad). Strong focusing is required in the lattices. This will result naturally in relatively small dispersions, as are required to contain the relatively large momentum spreads (up to 1.37 % *rms*).

The second challenge is the high instantaneous rf peak powers required, and the resulting large numbers of power sources. For the linacs and early recirculating accelerators, the powers are high because of the high gradients, and low frequencies required to accelerate the long bunches. At these frequencies (200-400 MHz), currently available

TABLE VIII. Accelerator parameters for a Higgs Factory (100 GeV)

Acc. type		linac	linac	recirc	recirc	recirc	sums
Magnet type				warm	warm	warm	
rf type		Cu	Cu	Cu	Cu	Cu	
$E^{\rm init}$	(GeV)	0.10	0.20	0.70	2	7	
$E^{\rm final}$	(GeV)	0.20	0.70	2	7	50	
Circ.	(km)	0.04	0.07	0.07	0.19	1.74	2.11
Turns		1	1	8	10	11	
Loss	(%)	2.31	3.98	7.27	7.91	13.94	31.06
Decay heat	W/m	0.89	1.98	11.04	12.99	12.44	
$B_{\rm fixed}$	(T)			2	2	2	
Ramp freq.	(kHz)			281	79.83	8.00	
Disp	m			1	1.50	3	
$\beta{\rm max}$	m	0.83	1.42	3.00	5.31	21.08	
$\sigma_z^{\rm init}$	(cm)	2.71	2.22	1.42	1.64	0.90	
$\Delta p/p^{\rm init}$	(%)	3.58	2.80	1.64	0.56	0.32	
σ_y	cm	1.09	1.14	1.01	0.85	0.94	
σ_y	cm			1.93	1.19	1.34	
Pipe full height	cm	10.92	11.42	10.14	8.49	9.39	
Pipe full width	cm	10.92	11.42	19.28	11.94	13.35	
rf freq.	(MHz)	200	200	200	200	400	
Acc/turn	(GeV)	0.20	0.40	0.17	0.50	4	
Acc time	(μs)			1	6	62	
η	(%)	5.15	5.36	6.36	2.84	6.92	
Acc. Grad.	(MV/m)	8	8	8	10	10	
Synch. rot's		0.62	0.63	0.62	3.92	23.16	
Cavity rad.	(cm)	54.37	54.88	54.88	60.47	38.26	
Beam time	msec	0.00	0.00	0.00	0.01	0.06	
rf time	msec	0.17	0.17	0.17	0.18	0.13	
Tot. peak rf	(GW)	0.05	0.10	0.05	0.26	4.71	5.17
Ave. rf power	MW	0.14	0.24	0.13	0.68	9.54	10.73
rf wall	MW	0.64	1.16	0.46	2.42	28.06	32.75

sources (triodes and tetrodes) have relatively low maximum output powers and are expensive. Low temperature operation of the cavities, and superconducting or conventional SLED [86] systems, which would reduce the peak power requirements, are being considered.

It should be noted that in the first two recirculators (up to 7 GeV) there is no hope for the rf to keep up with the beam loading. Conventional continuous (cw) matching of the sources to the loaded cavities is not possible. The cavity is filled in a suitable filling time (twice the time constant in these examples), and the rf voltage allowed to sag as the beam makes its multiple passes. If excessive sensitivity to beam current is to be avoided, then the stored energy must be large compared to that used, which is somewhat inefficient.

In the final recirculating accelerator, continuous filling (cw) is just possible, but requires yet higher peak power ($\approx$ 5 GW total at 400 MHz) because of the high acceleration rate. The use of superconducting cavities can reduce losses, and thus reduce this peak rf power source requirement (see next section), but is not used in this example. At this frequency (400 MHz), klystrons are available with greater power ($\approx$ 20 MW) than that of the sources at the lower frequencies, but a yet higher power klystron (50-100 MW) could probably be developed.

C. Acceleration for High Luminosity 100 GeV

Table IX gives a sequences of accelerators for a high luminosity 100 GeV collider. In this example, superconducting cavities are used the for 7-50 GeV rings. This is given as an illustration, and is not related to the higher luminosity parameters. The reason for the use of these cavities is to reduce the peak power requirement. As noted above, the power is high because the acceleration must be rapid to avoid decay losses, and thus the acceleration rate is also high.

The six dimensional emittance in this machine is the same as in the Higgs collider, but the transverse emittance is smaller ($\approx 90\pi$ mm mrad *rms*), and the longitudinal emittance larger; i.e. the product of the bunch length and momentum spread is larger (by about a factor of 4). If the momentum spread is to be kept low then the very long resulting bunches require lower frequency rf, which is large and expensive. Alternatively one must have lattices with very large momentum acceptances. The latter approach is used in the example given below (Tb. IX), with a momentum spread in the first recirculating accelerator of nearly 6 % *rms*; or about 50 % full width. This is large by conventional standards, but far less than that in the FFAG lattice being studied [83]. Indeed, if true FFAG lattices were to be used for their convenience of avoiding the switch yards and multi-aperture magnets, then the specified momentum spread would certainly not be a problem.

It would be desirable to use the same accelerator for both modes: Higgs low energy spread, and 100 GeV high luminosity. With little modification, the accelerators described here (Tb. IX) would be able to do this, but it is recognized that these parameters are harder to meet than those given in Tb. VIII.

TABLE IX. Accelerator parameters for a High Luminosity 100 GeV Collider

Acc. type		linac	linac	recirc	recirc	recirc	sums
Magnet type				warm	warm	warm	
rf type		Cu	Cu	Cu	Cu	SC Nb	
$E^{\rm init}$	(GeV)	0.10	0.20	0.70	2	7	
$E^{\rm final}$	(GeV)	0.20	0.70	2	7	50	
Circ.	(km)	0.04	0.07	0.07	0.19	1.74	2.11
Turns		1	1	8	10	11	
Loss	(%)	2.31	3.98	7.27	7.91	13.94	31.06
Decay heat	W/m	0.89	1.98	11.04	12.99	12.44	
$B_{\rm fixed}$	(T)			2	2	2	
Ramp freq.	(kHz)			281	79.83	8.00	
Disp.	m			0.40	0.60	0.80	
$\beta_{\rm max}$	m	0.56	0.95	2.94	5.88	26.00	
$\sigma_z^{\rm init}$	(cm)	9.17	7.51	5.73	4.29	2.55	
$\Delta p/p^{\rm init}$	(%)	12.10	9.45	4.63	2.44	1.27	
σ_y	cm	0.49	0.51	0.55	0.49	0.57	
σ_x	cm			1.85	1.47	1.02	
Pipe full height	cm	4.88	5.10	5.48	4.88	5.70	
Pipe full width	cm	4.88	5.10	18.52	14.67	10.16	
rf Freq	(MHz)	200	200	200	200	400	
Acc./turn	(GeV)	0.20	0.40	0.17	0.50	4	
Acc. time	(μs)			1	6	62	
η	(%)	5.15	5.36	6.36	2.84	6.92	
Acc. Grad.	(MV/m)	8	8	8	10	10	
Synch rot's		0.62	0.63	1.38	2.29	16.39	
Cavity rad	(cm)	54.37	54.88	54.88	60.47	38.26	
rf time	msec	0.04	0.04	0.04	0.05	0.23	
Tot. peak rf	(GW)	0.12	0.21	0.11	0.57	1.02	2.03
Ave. rf power	MW	0.07	0.13	0.07	0.41	3.52	4.21
rf wall	MW	0.35	0.64	0.26	1.47	10.34	13.07

D. Acceleration for 3 TeV Collider

For a high energy machine, the muons accelerators are physically the largest component and are also probably the most expensive. More work is needed on its design. Table X gives an early example of a possible sequence of accelerators for a 3 TeV collider. The initial accelerators, up to 50 GeV, are very similar to those for the high luminosity 100 GeV machine given above (Tb. IX), although the transverse emittance is even smaller and the longitudinal a little larger. Again, it would be desirable to design a single 50 GeV front end that could meet all three requirements.

1. *Magnet Systems*

For the final three stages, pulsed magnet synchrotrons [87] are used. In the 200 GeV ring, all the magnets in the ring are pulsed, but in the two last rings a superconducting-pulsed hybrid solution is needed. In these cases, if only pulsed magnets were used, then the power consumed would be too high; and because only low pulsed fields could be used, the circumferences would also be very large. It is thus proposed to use rings with alternating warm pulsed magnets and superconducting fixed magnets [88] (see figure 23). The fixed magnets are superconducting at 8 T; the pulsed magnets are warm with fields that swing from - 2 T to + 2 T. The effective ramp frequency is given in the table. By choosing appropriate ratios of fixed and pulsed magnets, the last two such rings can be located in the same tunnel.

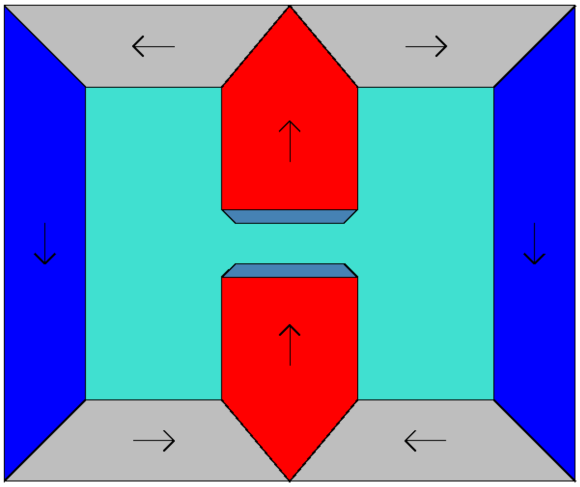

FIG. 22. A 2-d picture of an *H* frame magnet lamination with grain oriented 3 % Si-Fe steel.The arrows show both the magnetic field and the grain direction.

Designs of suitable pulsed magnets [88](see Fig. 22 have been shown to have sufficiently low losses for this application. The magnets employ cables made of many fine insulated strands (litz cable) and the yokes are made of very thin (.28 mm), 3% Si-Fe laminations, possibly of Metglas [89,90] for the higher rate cases.

2. *RF Systems*

In all the final three rings superconducting rf is employed to minimize the peak power requirements. In the final rings this is also important to obtain high wall to beam efficiency and thus keep the wall power consumption reasonable. In the final two rings the frequency and cavity designs are chosen to be the same as that in the TESLA [91] proposal. Higher order mode damping will have to be studied to see if modifications are needed.

E. Simulations

A study [92] followed the longitudinal motion of particles through a similar sequence of recirculating accelerators (for a 4 TeV collider in that case). rf cavities similar to those proposed for TESLA [91] were assumed. Figure 24 shows, after optimization of parameters, the final longitudinal phase space distributions corresponding to wake fields estimated for four different bunch charges: a) very small, b) 0.83×10^{12} muons, c) 2.08×10^{12} muons, and d) 4.17×10^{12} muons.

For the design beam charge of 2×10^{12} muons (approximately as for Fig. 24(c) the wakefield amplitude was estimated to be 2.5 MV/m, the accelerating phase used was 35^o, and rf voltage depression 26 %. The simulation used an initial longitudinal phase space 20 eV-s. It gave negligible particle loss, a final longitudinal phase space was 21.6 eV-s, and thus an increase of longitudinal emittance of only 8 %.

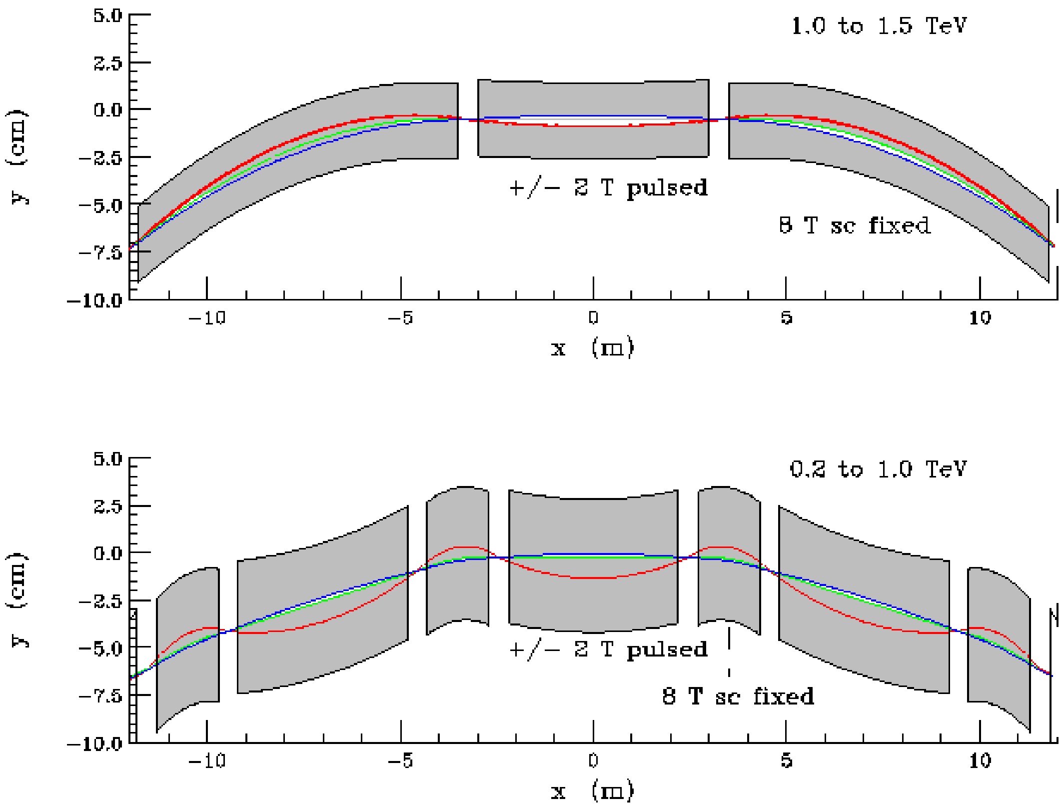

FIG. 23. Schematic of hybrid superconducting-pulse magnet accelerator ring

VII. COLLIDER STORAGE RING

A. Introduction

After acceleration, both μ^+ and μ^- bunches are injected into a separate storage ring. The highest possible average bending field is desirable, to maximize the number of revolutions before decay, and thus maximize the luminosity. Collisions would occur in one, or perhaps two, low-β^* interaction areas. Parameters of the rings were given earlier in Tb. I.

B. Lattice Design

In order to maintain the required short bunches without excessive rf, the ring must be approximately, or fully, isochronous.

The required β functions at the intersection point are small for a 3 TeV collider, we require $\beta^* = 3\,\mathrm{mm}$, and the quadrupoles needed to generate them are large (20-30 cm diameter). At 100 GeV CoM, the β's at the IP are not that small, and the quadrupoles are more conventional, but in both cases it has been found that local chromatic correction is essential [93–96].

The rings are racetracks, with two circular arcs separated by an experimental insertion, on one side, and a utility insertion for injection, extraction, and beam scraping, on the other. The experimental insertion includes the interaction region (IR) followed by a local chromatic correction (CCS) and a matching section. The chromatic correction section is optimized to correct the ring's linear chromaticity, which is almost completely generated by the IR.

The bending magnets would be superconducting. The magnets must be shielded from the electrons emitted by decay of the beam. Fields of 8 T have been assumed in the 100 GeV lattices described below, but higher field dipoles would reduce the ring diameters and increase luminosity. Studies of higher field dipoles have been started.

TABLE X. Parameters of Acceleration for 3 TeV Collider

Acc. type		linac	recirc	recirc	recirc	recirc	synch	synch	sums
Magnet type			warm	warm	warm	warm	hybrid	hybrid	
rf type		Cu	Cu	Cu	SC Nb	SC Nb	SC Nb	SC Nb	
E^{init}	(GeV)	0.10	0.70	2	7	50	200	1000	
E^{final}	(GeV)	0.70	2	7	50	200	1000	1500	
Circ.	(km)	0.07	0.12	0.26	1.74	4.65	11.30	11.36	29.52
Turns		2	8	10	11	15	27	17	
Loss	(%)	6.11	12.28	10.84	13.94	10.68	10.07	2.65	50.58
Decay heat	W/m	3.67	15.02	16.89	15.91	19.44	30.97	18.09	
B_{pulse}	(T)					2	2	2	
B_{fixed}	(T)		0.70	1.20	2		8	8	
Ramp freq.	(kHz)		162	57.34	8.00	2.15	0.50	0.79	
Disp.	m		0.40	0.60	0.80	1	2	4	
βmax	m	0.89	3.97	8.75	36.29	52.20	108	120	
Mom. compactn	%		1	-0.25	-0.50	-0.50	-0.50	-1	
σ_z^{init}	(cm)	16.34	8.53	5.29	3.57	1.59	0.96	0.78	
$\Delta p/p^{\text{init}}$	(%)	19.27	8.49	5.41	2.47	0.82	0.35	0.09	
σ_y	cm	0.45	0.45	0.42	0.48	0.22	0.16	0.08	
σ_x	cm		3.40	3.25	1.98	0.82	0.71	0.36	
Pipe full height	cm	4.46	4.52	4.22	4.77	2.20	1.62	0.78	
Pipe full width	cm	4.46	33.95	32.49	19.79	8.20	7.06	3.62	
rf Freq	(MHz)	200	100	200	200	800	1300	1300	
Acc./turn	(GeV)	0.40	0.17	0.50	4	10	30	30	
Acc. time	(μs)		3	8	62	232	1004	631	
η	(%)	3.82	0.96	1.97	1.11	10.15	14.37	12.92	
Acc. Grad.	(MV/m)	8	8	10	10	15	25	25	
Synch. rot's		0.81	0.76	1.02	5.82	19.14	54.29	31.30	
Cavity rad.	(cm)	54.88	110	60.47	76.52	19.13	11.77	11.77	
rf time	msec	0.04	0.12	0.05	0.56	0.40	1.25	0.96	
Tot. peak rf	(GW)	0.21	0.14	0.59	1.31	1.06	1.16	1.04	5.51
Ave. rf power	MW	0.14	0.25	0.45	11.04	6.32	21.91	15.07	55.18
rf wall	MW	0.64	0.88	1.62	32.47	18.59	44.72	30.76	130

The rf requirements depend on the lattice momentum compaction and bunch parameters. For the very low momentum spread Higgs collider parameters, synchrotron motion does not occur and rf is used solely to correct impedance generated momentum spread in the bunch. For the higher momentum spread cases, there are two options. If the momentum compaction can be corrected to high order then synchrotron motion can still be eliminated and the rf is again only used for energy spread correction. Alternatively, if some momentum compaction is retained, then significant rf is needed to maintain the specified short bunches. In either case rf quadrupoles will be required to generate BNS [97] damping of the transverse head-tail instability (beam breakup).

C. Lattices

Preliminary lattices have been designed for both 4 TeV and 0.5 TeV machines [98], and several designs now exist for the 100 GeV case. For the 100 GeV CoM collider, two operating cases are being considered a high-luminosity case with broad momentum acceptance to accommodate a beam with a $\delta p/p$ of $\pm 0.12\%$ (rms) and one with a much narrower momentum acceptance and lower luminosity for beam with $\delta p/p$ of $\pm 0.003\%$ (rms). For the broad momentum acceptance case, the β^* must be 4 cm and for narrow momentum acceptance, 13 cm. In either case, the bunch length must be held comparable to the value of β^*. It is assumed that a single lattice can be designed that can operate in either mode by adjusting settings.

We describe below two examples of 100 GeV designs. They were generated by two different semi-independent, but converging, studies. The primary difference between the two is in the flexible momentum compaction arc modules.

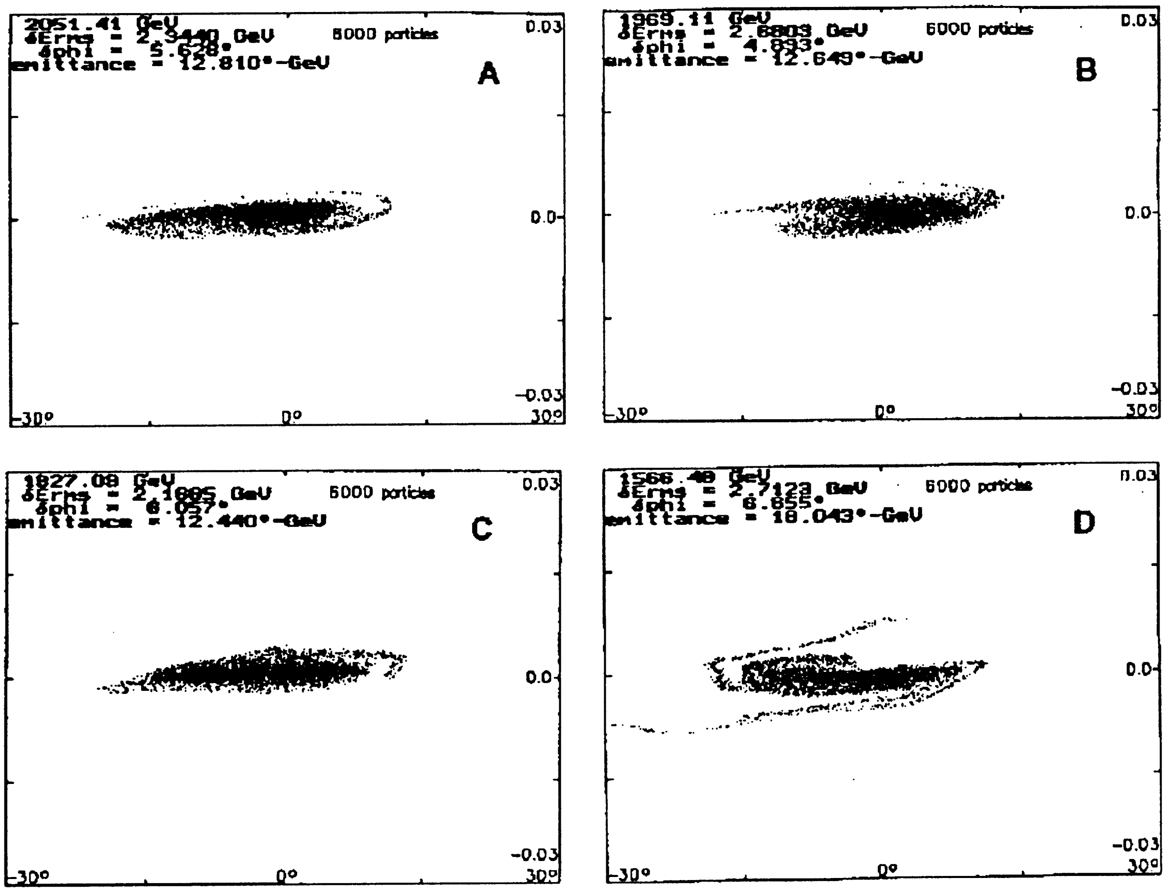

FIG. 24. μRLA simulation results with wake fields, with beam accelerated from 200 to 2000 GeV in a 10-turn RLA. Longitudinal phase space plots for: A) very small number; B) 0.83×10^{12}; C) 2.08×10^{12} and D) 4.17×10^{12} muons in a bunch.

1. 100 GeV first example

This design, shown in Fig. 25, has a total circumference of about 350 m with arc modules accounting for only about a quarter of the ring circumference.

The low-beta function values at the IP are mainly produced by three strong superconducting quadrupoles in the Final Focus Telescope (FFT) with pole-tip fields of 8 T. The full interaction region is symmetric with reflection about the intersection point (IP). Because of significant, large-angle backgrounds from muon decay, a background-sweep dipole must be included in the final focus telescope and placed near the IP to protect the detector and low-β quadrupoles [99]. It was found that 2.5 m of an 8 T field was required to attain sufficient background suppression. The first quadrupole is located 5 m away from the interaction point, the beta reaches a maximum of 1.5 km in the final focus telescope when the beta functions are equalized in both planes. For this value of beta, quadrupole apertures must be at least 15 cm in radius to accommodate 5σ of an 90 π mm-mr, 50-GeV muon beam (normalized rms emittance) plus a 2 to 3 cm thick tungsten liner [100]. The natural chromaticity of this interaction region is about -60.

Local chromatic correction of all muon collider interaction regions is required to achieve broad momentum acceptance. The basic approach developed by Brown [94] and others [101], is used. Two pairs of sextupoles, one pair in each plane, are separated by a phase advance of π, all in high dispersion, with each being $(2n+1)\pi/2$ from the IP. The geometric aberrations of each sextupole is canceled by its companion while the chromaticity corrections add.

In our case, this chromatic correction section design (Fig. 26) was optimized to be as short possible. The $\beta_{\rm max}$ is only 100 m and the $\beta_{\rm min} = 0.7$ m, giving a $\beta_{\rm ratio}$ between planes of about 150 without compromising aperture by a large amplitude dependent tuneshift.

The sextupoles are centered about the opposite-plane minimum ($\beta_{min} < 1$), which provides a chromatic correction

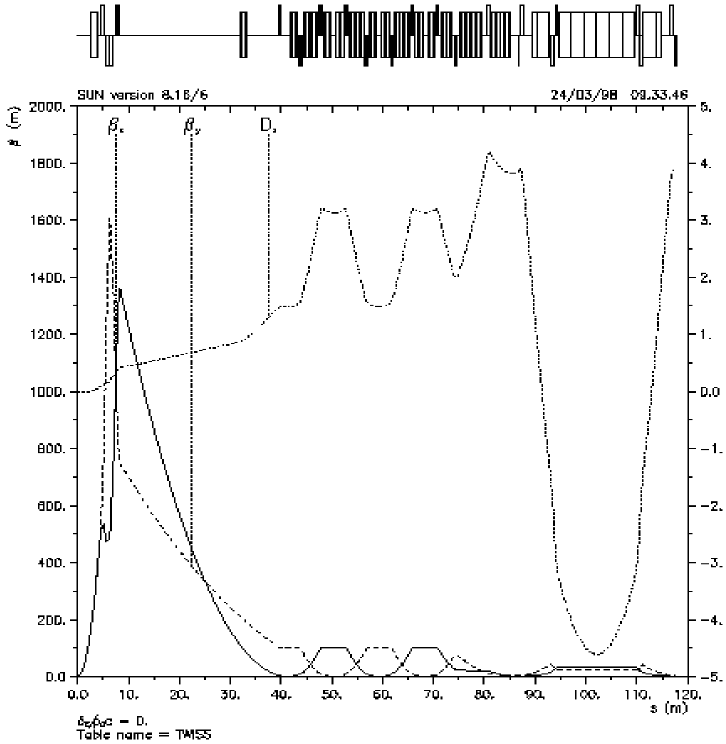

FIG. 25. Example (a): Half of the IR, local chromatic correction, and one of three arc modules.

with minimal cross correlation between planes. A further advantage to locating the opposite-plane minimum at the center of the sextupole is that this point is $\pi/2$ away from, or, "out of phase" with the chromatic effects from the final-focus quadrupoles; i.e. the plane not being chromatically corrected is treated like the IP in terms of phase to eliminate a second order chromatic aberration arising from the sextupole.

The large beta ratio combined with the opposite-plane phasing allowed sextupoles for opposite planes to be interleaved without significantly impacting lattice nonlinearity. In point of fact, interleaving improved lattice performance over a non-interleaved correction scheme, primarily due to a shortening of the chromatic correction section, which is accompanied by a lowering of its contribution to overall chromaticity [102]. Shallower minima and less variations in beta were also applied to soften chromatic aberrations, but at the expense of an exact π phase separation between sextupole partners. The retention of an exact π phase difference between sextupoles was found to be less important to the dynamic aperture than elimination of minima with $\beta_{\rm min} < 0.5$ m.

The momentum compaction of the IR, chromatic correction section, and matching sections is about 0.04. Since the length of this part is 173 m, the 93 m arc length must have a negative momentum compaction of about -0.09 in order to offset the positive portion of the ring.

The arc module Fig. 27 has the small beta functions characteristic of FODO cells, yet a large, almost separate, variability in the momentum compaction of the module which is a characteristics associated with the flexible momentum compaction module [103]. The small beta functions are achieved through the use of a doublet focusing structure which produces a low beta simultaneously in both planes. At the dual minima, a strong focusing quadrupole is placed to control the derivative of dispersion with little impact on the beta functions. Negative values of momentum compaction as low as $\alpha = -0.13$ has been achieved, and $\gamma_t = 2$ i, has been achieved with modest values of the beta function.

This arc module was able to generate the needed negative momentum compaction with beta functions of 40 m or less. The peak dispersion is somewhat high, 4.6 m and needs to be reduced.

A very preliminary calculation of the dynamic aperture [79] without optimization of the lattice nor inclusion of errors and end effects is given in Fig. 28.

For the very low momentum spread operation, a larger acceptance is required. This should be possible by turning the sextupoles off. The result of doing this is also shown in the figure (dashed line). The momentum acceptance is lost, as expected, but the gain in transverse acceptance, though real, is disappointing. More work is needed.

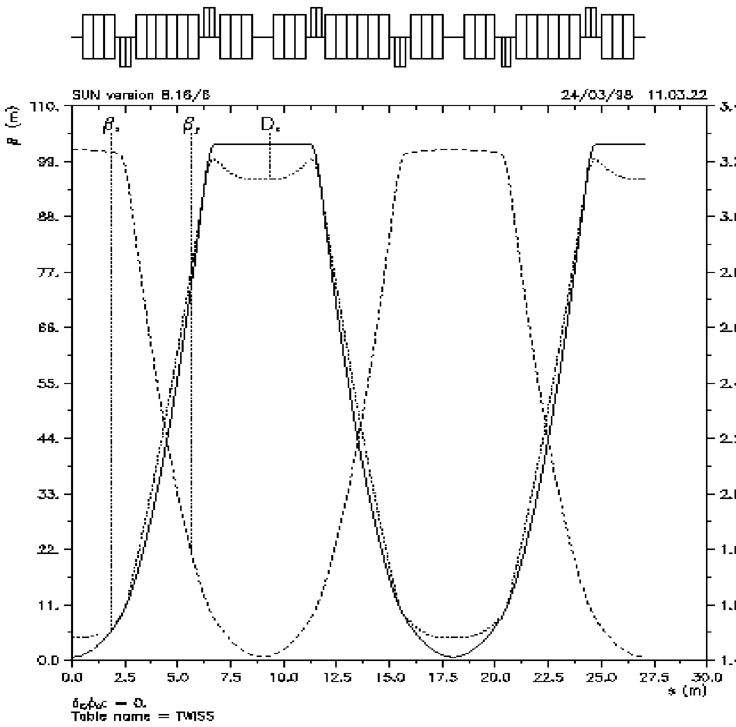

FIG. 26. Example (a): The Chromatic Correction Module.

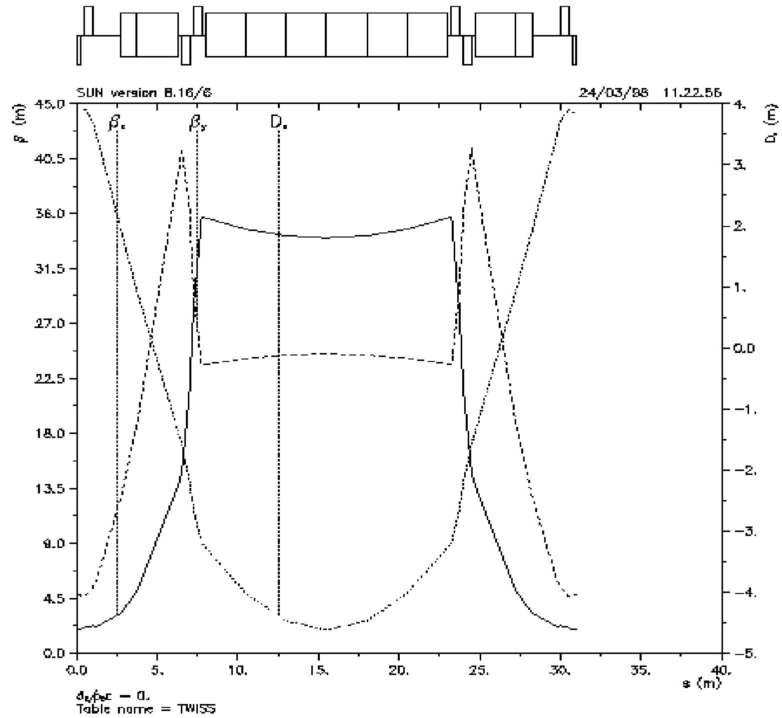

FIG. 27. Example (a): A New Flexible Momentum Compaction Arc Module.

2. 100 GeV second example

The second lattice is shown in Fig. 29 starting from the IP.

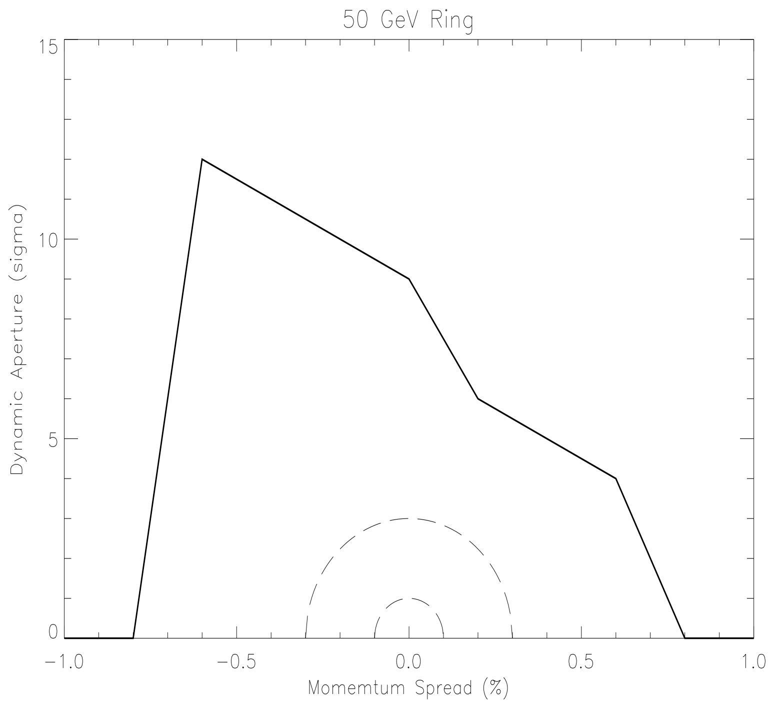

FIG. 28. Example (a): A preliminary dynamic aperture.

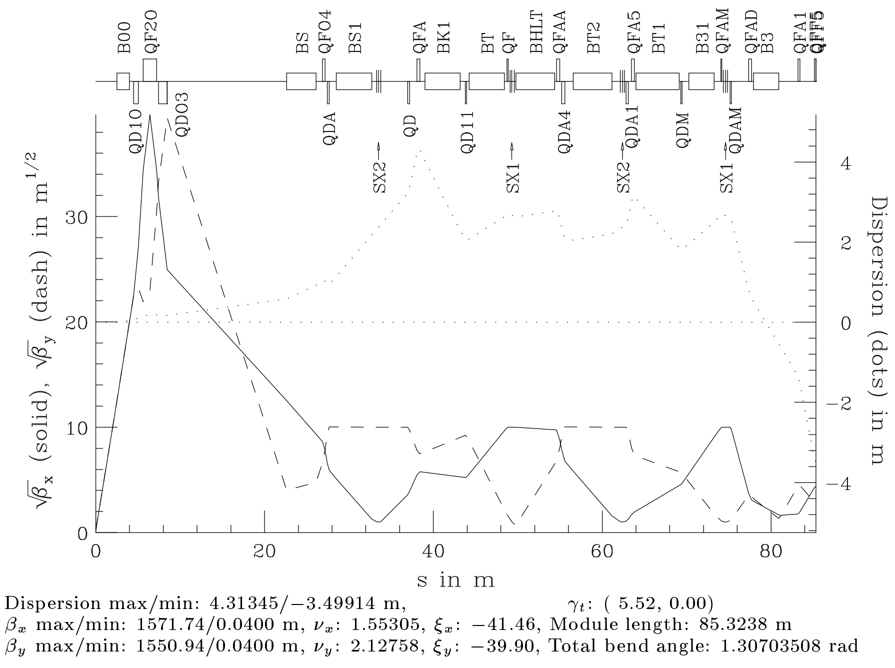

FIG. 29. Example (b): Structure of the interaction region including local chromaticity corrections.

The 1.5 m background clearing dipole is 2.5 m away from the IP and is followed by the triplet quadrupoles with the focusing quadrupole in the center. The interaction region (IR) stops at about 24 m from the IP and the local correction section begins. The Twiss properties at the centers of the 4 correction sextupoles are listed in Tb. XI.

We denote by SX1 the two horizontal correction sextupoles. They are placed at positions with the same betatron functions and dispersion function, and are separated horizontally and vertically by phase advances π so that their

TABLE XI. Twiss properties of the interaction region correction sextupoles.

	Distance	Phase Advances		Betatron Functions (m)		Dispersion
	(m)	ν_x	ν_y	β_x	β_y	(m)
SX2	33.5061	0.48826	0.74953	1.00000	100.00012	2.37647
SX2	62.3942	0.98707	1.24953	1.00000	100.00009	2.37651
SX1	49.3327	0.74892	0.87703	100.00023	1.00000	2.66039
SX1	74.6074	1.24892	1.47987	99.99967	0.99992	2.65817

nonlinear effect will be confined in the region between the two sextupoles. Their horizontal phase advances are also integer numbers of π from the triplet focusing F-quadrupole so that the chromaticity compensation for that quadrupole will be most efficient [101]. The SX2's are the two vertical correction sextupoles and are placed similarly at designated locations. Notice that the correction section on each side of the IP spans a distance of roughly 61.3 m.

Flexible momentum-compaction (FMC) modules [104] are used in the arc. The momentum compaction of the arc has to be made negative in order to cancel the positive momentum compaction of the IR, so that the whole ring becomes quasi-isochronous. This is accomplished in three ways: removing the central dipole of the standard FMC module, by increasing the length of the first and last dipoles, and by increasing the negative dispersion at entrance. Two such modules are required for half of the collider ring, one of which is shown in Fig. 30.

To close the ring geometrically, there will be a $\sim$ 72.0 m straight section between the two sets of FMC modules. The total length of the collider ring is now 354.3 m. Note that the interaction region and local correction sections take up 48.2% of the whole ring. The momentum-compaction factor of the whole ring is now $\alpha_0 = -2.77 \times 10^{-4}$. If the bucket height is taken as $k = 8$ times the rms momentum spread of the bunch, an rf voltage of $V_{\rm rf} \approx 770(\frac{\delta p}{p})^2$ kV will be required. Since α_0 is negative already, its absolute value can be further lowered easily. However, we must make sure that the contributions from the higher-order momentum compaction are small also. This will be studied. Note that there are not yet families of sextupoles to correct for the higher order chromaticities in this ring with only 4 FMC modules.

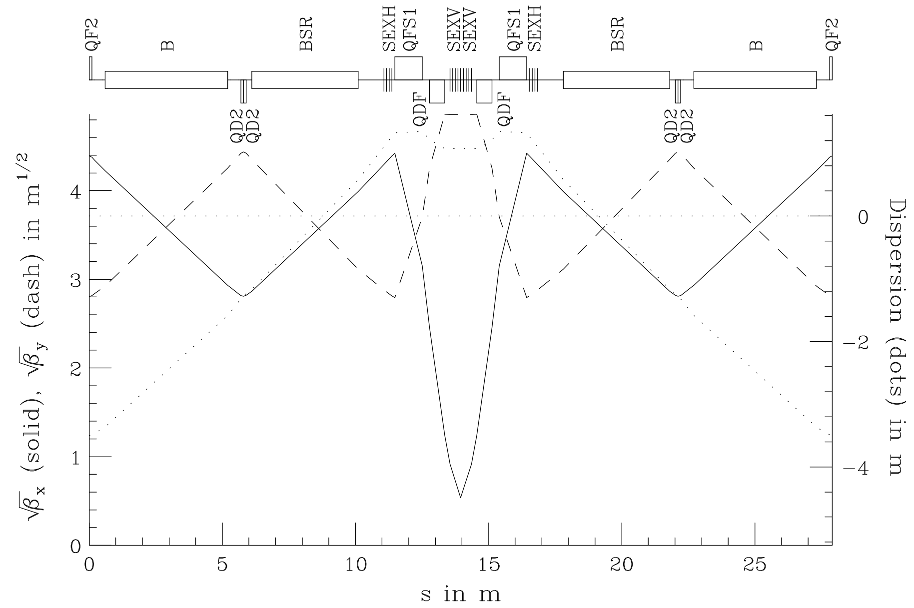

FIG. 30. Example (b): Lattice structure of the flexible momentum-compaction module.

The dynamical aperture of the lattice is computed by tracking particles with the code COSY [105]. We track 16 particles with the same momentum offset and x' and y' placed uniformly on a very small circle. If all particles survive, then the radius is increased and the tracking repeated. The largest radius that provide survival of the 16 particles in 1000 turns is defined here as the dynamical aperture at this momentum offset and is plotted in solid in Fig. 31(a) in units of the rms radius of the beam at the IP. (At the 4 cm low-beta IP, the beam has an rms radius of 82 μm). As a reference, the 7-sigma aperture spanning ± 5 sigmas of momentum offset is also displayed as a semi-ellipse in dots. To maximize the aperture, first, the tunes must be chosen to avoid parametric resonances. The on-momentum amplitude dependent horizontal and vertical tunes are $\nu_x = 8.126337 - 100\epsilon_x - 4140\epsilon_y$ and $\nu_y = 6.239988 - 4140\epsilon_x - 54.6\epsilon_y$, where ϵ_x and ϵ_y are the horizontal and vertical unnormalized emittance in πm. With the designed rms $\epsilon_x = \epsilon_y = 0.169$ πm, the variations appear to be small. Second, the chromaticity variations with momentum must be as small as possible. This is shown in Fig. 31(b). For momentum spread varying from -1 to 0.9%, ν_x varies from 8.16698 to 8.07459, and ν_y from 6.28305 to 6.22369 for the center of the beam.

During aperture tracking we notice particle loss occurs mostly in the horizontal direction. We are convinced that the small aperture is a result of the large dispersion swing in the lattice from +4.5 to −3.5 m. For example, −4.5 m dispersion and 0.6% momentum offset translates into a 2.7 cm off-axis motion. The nonlinearity of the lattice will therefore diminish the dynamical aperture. A resonant strength study actually reveals that this lattice is unusually nonlinear. Recently, we made a modification of the flexible momentum compaction arc modules which have a smaller dispersion swing from −2.6 to +2.0 m only. The interaction region was not changed except for the matching to the arc modules. The aperture was tracked with TEAPOT [106] in the same way as it was done with COSY and is plotted as dashes in Fig. 31(a). We see that the momentum aperture is wider, but the aperture near on-momentum is one sigma less than the lattice discussed above; nevertheless, this may not be so bad, because all trackings have been performed in steps of one sigma only.

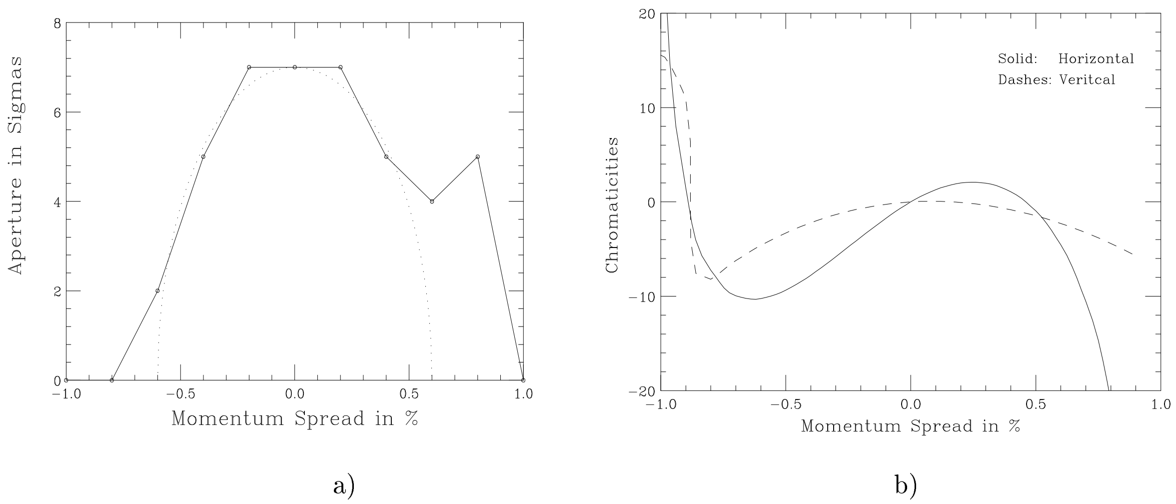

FIG. 31. Example (b): a) Dynamical aperture of the lattice *vs.* momentum offset. b) Chromaticities *vs.* momentum offset.

D. Scraping

It has been shown [107] that detector backgrounds originating from beam halo can exceed those from decays in the vicinity of the interaction point (IP). Only with a dedicated beam cleaning system far enough from the IP can one mitigate this problem [100]. Muons injected with large momentum errors or betatron oscillations will be lost within the first few turns. After that, with active scraping, the beam halo generated through beam-gas scattering, resonances and beam-beam interactions at the IP reaches equilibrium and beam losses remain constant throughout the rest of the cycle.

Two beam cleaning schemes have been designed [100], one for muon colliders at high energies, and one for those at low energies.

The studies [100] showed that no absorber, ordinary or magnetized, will suffice for beam cleaning at 2 TeV; in fact the disturbed muons are often lost in the IR, but a simple metal collimator was found to be satisfactory at 100 GeV.

1. Scraping for High Energy Collider

At high energies, a 3-m long electrostatic deflector (Fig. 32) separates muons with amplitudes larger than 3σ and deflects them into a 3-m long Lambertson magnet, which extracts these downwards through a deflection of 17 mrad. A vertical septum magnet is used in the vertical scraping section instead of the Lambertson to keep the direction of extracted beam down. The shaving process lasts for the first few turns. To achieve practical distances and design apertures for the separator/Lambertson combinations, β-functions must reach a kilometer in the 2-TeV case, but only 100 m at 50 GeV. The complete system consists of a vertical scraping section and two horizontal ones for positive and negative momentum scraping (the design is symmetric about the center, so scraping is identical for both μ^+ and μ^-). The system provides a scraping efficiency of a factor of 1000.

2. Scraping for Low Energy Collider

At 50 GeV, collimating muon halos with a 5-m long steel absorber (Fig. 33) in a simple compact utility section does an excellent job. Muons lose a significant fraction of their energy in such an absorber (8% on average) and have broad angular and spatial distributions. Almost all of these muons are then lost in the first 50-100 m downstream of the absorber with only 0.07% of the scraped muons reaching the low-β quadrupoles in the IR, i.e. a scraping efficiency is 1500 in this case, which is significantly better than with in an earlier septum scraping system [100] similar to that developed for the high energy collider.

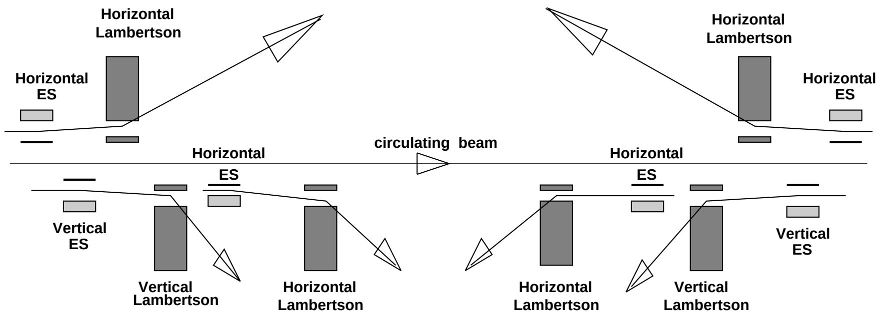

FIG. 32. Schematic view of a $\mu^+\mu^-$collider beam halo extraction.

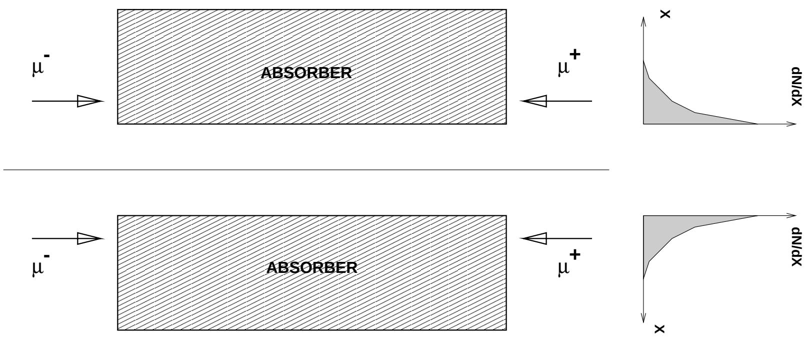

FIG. 33. Scraping muon beam halo with a 5-m steel absorber.

E. Beam-Beam Tune Shift

Several studies have considered beam emittance growth due to beam-beam tune shift and none observed significant luminosity loss. For instance, a study [108], using the high energy collider parameters (Tb.I), in which particles were tracked assuming Gaussian beam field distributions, and no muon decay, showed a luminosity loss of only 4 %. With muon decay included, the loss contribution from beam-beam effects is even less. Another study [109] using a particle in cell approach with no assumptions about field symmetry obtained a similar result. Collisions between beams displaced by 10 % of their radius also gave little loss. But all these studies assumed an ideal lattice, and none considered whether a very small fraction of the beam may be lost, giving probably unacceptable background. More work is in progress.

F. Impedance/Wake Field Considerations

A study [110] has examined the resistive wall impedance longitudinal instabilities in rings at several energies. At the higher energies and larger momentum spreads, solutions were found with small but finite momentum compaction, and moderate rf. For the special case of the Higgs Factory, with its very low momentum spread, a solution was found with no synchrotron motion, but rf provided to correct the first order impedance generated momentum spread. The remaining off-momentum tails, that would not affect the luminosity, but which might generate background, could be removed by a higher harmonic rf correction. Solutions to the higher energy and larger momentum spread cases without synchrotron motion are also being considered.

Given the very slow, or nonexistent synchrotron oscillations, the transverse beam breakup instability is significant. This instability can be stabilized using rf quadrupole [97] induced BNS damping. For instance, in the 3 TeV case, to stabilize the resistive wall instability, the required tune shift with position in the bunch, calculated [111] using the two particle model approximation, for a 1 cm radius aluminum pipe, is only 1.58×10^{-4}. However, this application of the BNS damping to a quasi-isochronous ring, and other head-tail instabilities due to the chromaticities ξ and η_1, needs more careful study.

G. Bending Magnet Design

The dipole fields assumed in the 100 GeV collider lattices described above was 8 T. This field can be obtained using 1.8^o Niobium Titanium (NbTi) cosine theta superconducting magnets similar to those developed for LHC. The only complication is the need for a tungsten shield between the beam and coils to shield the latter from beam decay heating.

The μ's decay within the rings ($\mu^- \rightarrow\ e^-\overline{\nu_e}\nu_\mu$), producing electrons whose mean energy is approximately 0.35 that of the muons. With no shielding, the average power deposited per unit length would be about 2 kW/m in the 4 TeV machine, and 300 W/m in the 100 GeV Higgs factory. Figure 34 shows the power penetrating tungsten shields of different thickness [20,99,100,112]. One sees that 3 cm in the low energy case, or 6 cm at high energy would reduce the power to below 10 W/m, which can reasonably be taken by superconducting magnets.

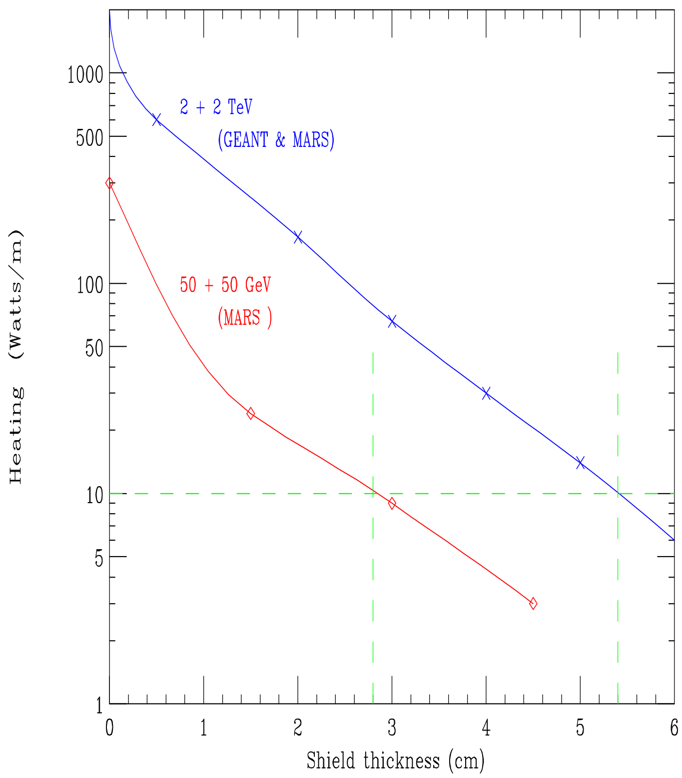

FIG. 34. Power penetrating tungsten shields vs. their thickness for a) 4 TeV, and b) 100 GeV, collider.

Figure 35 shows the cross section of a baseline magnet suitable for the 100 GeV collider.

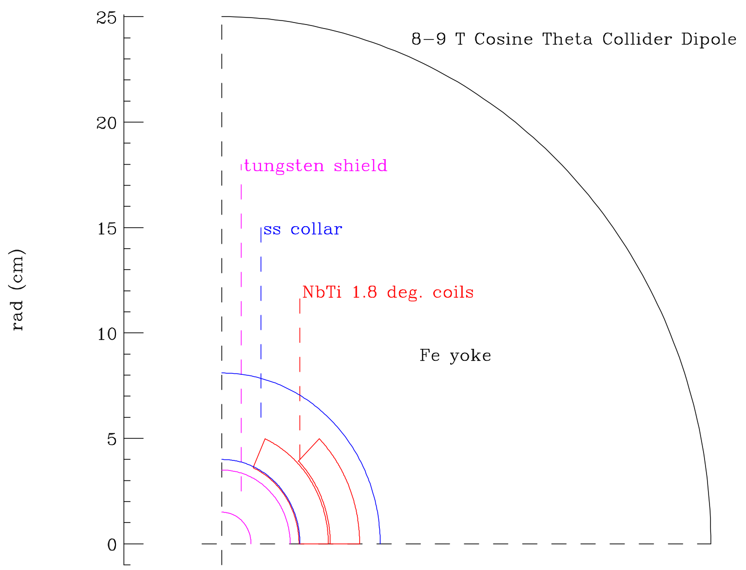

FIG. 35. Cross Section of a Baseline Dipole Magnet Suitable for the 100 GeV Collider.

The quadrupoles could use warm iron poles placed as close to the beam as practical. The coils could then be either superconducting or warm, placed at a greater distance from the beam and shielded from it by the poles.

The collider ring could be made smaller, and the luminosity increased, if higher field dipoles were used. In the low energy case, the gain would not be great since less than half the circumference is devoted to arc. For this reason, and to avoid yet another technical challenge, higher field magnets are not part of the baseline design of a 100 GeV collider. But they would give a significant luminosity improvement for the higher energy colliders, and would be desirable there. There have been several studies of possible designs, three of which (two that are promising and one that appears not to work) are included below.

1. Alternative Racetrack Nb_3Sn dipole

A higher field magnet based on Nb_3Sn conductor and racetrack coils is presently being designed. The Nb_3Sn conductor allows higher fields and provides a high temperature margin over the operating temperature, but being brittle and sensitive to bending or other stress, presents a number of engineering challenges.

In this design, the stress levels in the conductor are reduced by the use of a rectangular coil block geometry and end support problems are reduced by keeping the coils flat. In the more conventional *cos theta* designs, the conductor is distributed around a cylinder and the forces add up towards the mid-plane; in addition, the ends, as the arc over the cylinder, are relatively hard to support.

The geometry of the cross section is shown in Fig. 36. It uses all 2-D flat racetrack coils. Each quadrant of the magnet aperture has two blocks of conductors. The block at the pole in the first quadrant has a return block in the second quadrant, similar to that in a conventional design. The height of this block is such that it completely clears the bore. In a conventional design, the second block, the midplane block, would also have a return block in the second quadrant. That would, however, require the conductor block to be lifted up in the ends to clear the bore and thus would lose the simple 2-D geometry. In the proposed design, the return block retains the 2-D coil geometry as it is returned on the same side (see Fig. 36) and naturally clears the bore. Since the return block does not contribute to the field, this design uses 50 % more conductor. This, however, is a small penalty to pay for a few magnets where the performance and not the cost is a major issue. The field lines are also shown in Fig. 36.

Preliminary design parameters for two cases are given here. The first case is one when the performance of the cable used is the same that is in the LBL D20 magnet, which created a central field of 13.5 T. The second case, is the one when the cable is graded and two types of cables are used, and it is assumed that a reported improvement in cable performance is realized. It is expected to produce a central field of 14.7 T when operated at 4.2 ^oK.

Case 1: Same conductor as in LBL 13.5 T D20 magnet without grading	
Central field at quench	13 T at 4.2 $^o K$
Coil dimensions	25 mm $\times$ 70 mm
Total number of racetrack coils in whole magnet	6
Total number of blocks per quadrant in aperture	2 (+1 outside the aperture)
Yoke outer radius	500 mm (same as in D20)
Field harmonics	a few parts in 10^{-5} at 10 mm
Midplane gap (midplane to coil)	5 mm (coil to coil 10 mm)
Minimum coil height in the end	45 mm (Note: coils are not lifted up.)

Case 2: Newer conductor and graded	
Central field at quench	14.7 T at 4.2 $^o K$
Grading	70 mm divided in two 35 mm layers
Overall current densities	370 A/mm^2 and 600 A/mm^2
Peak fields	16 T and 12.5 T
Copper current density	1500 A/mm^2
Other features are the same as in *case 1*	

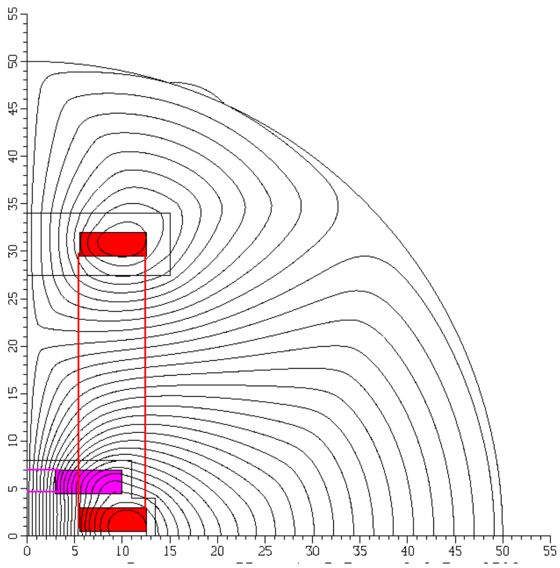

FIG. 36. Cross section of Alternative High Field ($\approx$ 15 T) Race Track Coil Dipole Magnet magnet with Nb_3Sn conductor.

2. *Alternative Cos Theta Nb_3Sn dipole*

In this case the problem with the brittle and sensitive conductor is solved by winding the coil inside many separate slots cut in metal support cylinders. There is no build up of forces on the coil at the mid-plane. The slots continue round the ends, and thus solve the support problem there too.

Figure 37 shows this alternative Nb_3Sn dipole cos theta design. It is an extension of the concept used to build helical magnets [113] for the polarized proton program at RHIC [114]. The magnet is wound with pre-reacted, kapton-insulated, B-stage impregnated, low current cable. The build up forces is controlled by laying the cables in machined slots in a metal support cylinder. After winding, the openings of the slots are bridged by metal spacers and the coils pre compressed inward by winding B-stage impregnated high tensile thread around the spacers. After curing, the outside of each coil assembly is machined prior to its insertion into an outer coil, or into the yoke. There are 3 layers. The inner bore is 55 mm radius, the outer coil radius approximately 118 mm, and the yoke inside radius 127 mm. The maximum copper current density is 1300 A/mm^2.

Using the same material specification as used in the above high field option, a central short sample field of 13.2 T was calculated. This is somewhat less than the block design discussed above, but could be improved by increasing the cable diameters to improve the currently rather poor (64%) cable to cable-plus-insulator ratio.

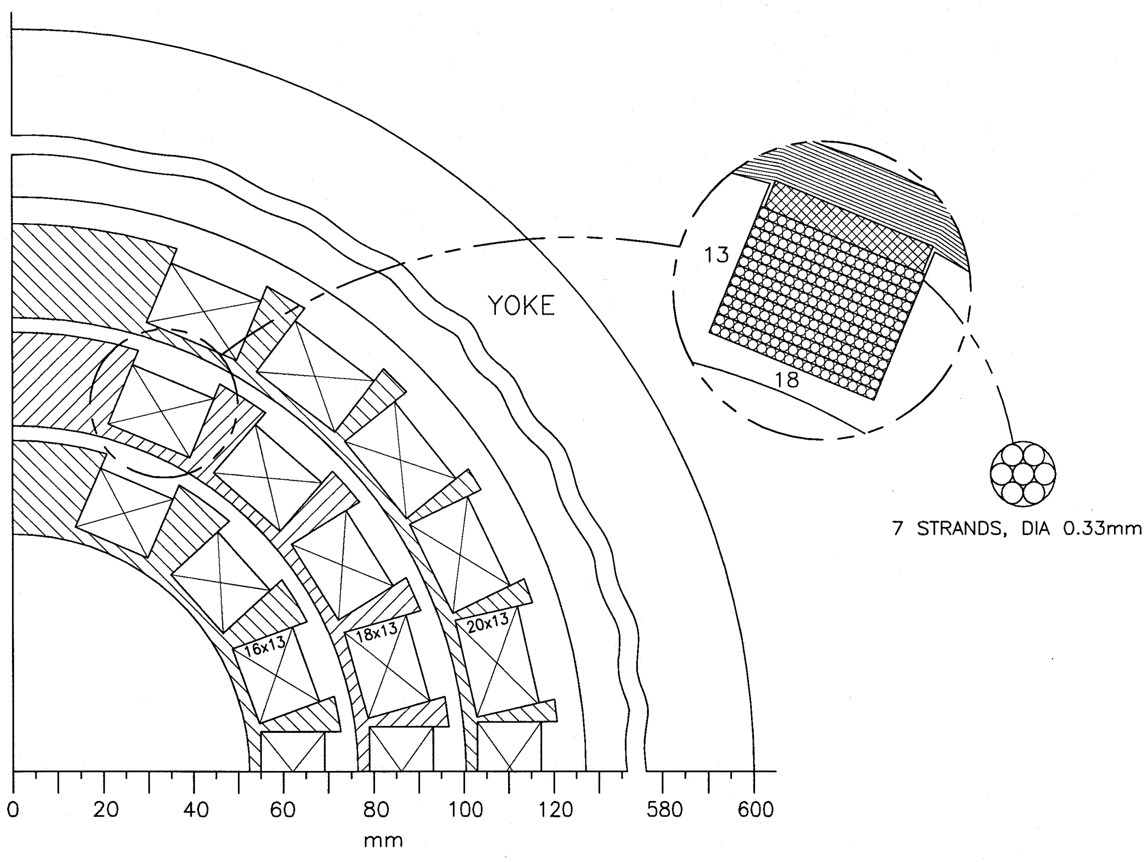

FIG. 37. Cross section of Alternative High Field Slot Dipole made with Nb_3Sn conductor.

3. Study of C-magnet dipole

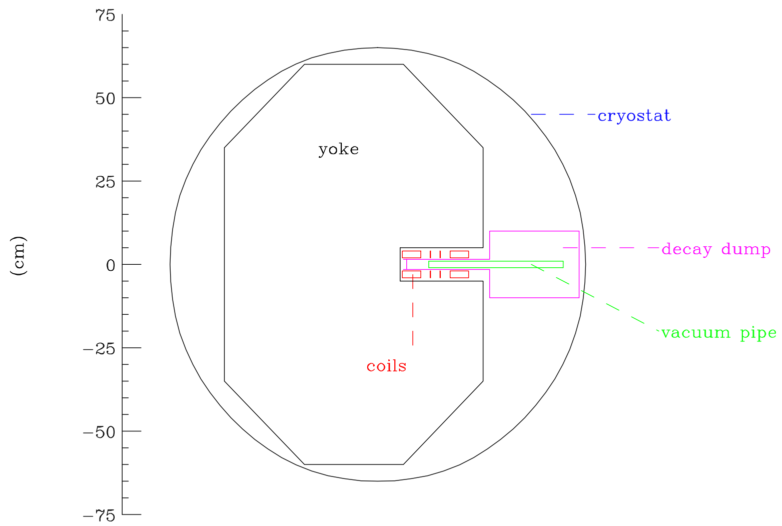

FIG. 38. Cross section of unsuccessful alternative high field C magnet with open mid-plane.

Figure 38 shows the cross section of a high field dipole magnet in which it was hoped to bring the coils in closer to the beam pipe without suffering excessive heating from beam decay. The coil design [115] appeared reasonable, but the required avoidance of coil heating was not achieved.

Decay electrons are generated at very small angles ($\approx 1/\gamma$) to the beam, and with an average energy about 1/3 of the beam. Such electrons initially spiral inward (to the right in Fig. 38) bent by the high dipole field. In the high energy case, they also radiate a significant fraction of their energy as ($\approx$ 1 GeV) synchrotron gamma rays, some of which finish up on the outside (to the left in Fig. 38). The concept was to use a very wide beam pipe, allow the electrons to exit between the coils, and be absorbed in an external cooled dump. Unfortunately a preliminary study found that a substantial fraction of the electrons did not reach the dump. They were bent back outward, before reaching it, by the return field of the magnet coils and the nature of the curved ring geometry. Such electrons were then trapped about the null in the vertical field and eventually hit the upper or lower face of the unshielded vacuum pipe. They showered, and deposited unacceptable levels of heat in the coils.

Another idea called for collimators between each bending magnet that would catch such trapped electrons. This option was not studied in detail, but the impedance consequences of such periodic collimators was expected to be unacceptable.

Further study of such options might find a solution, but the use of a thick cylindrical heavy metal shield appears practical, adequate, and is thus the current baseline choice.

H. Energy Scale calibration

In order to scan the width of a Higgs boson of mass around 100 GeV, one needs to measure the energy of the individual muon stores to an accuracy of a few parts per million, since the width of a Higgs boson of that mass is expected to be a few MeV. Assuming that muon bunches can be produced with modest polarizations of ≈ 0.25, and that the polarization can be maintained from turn to turn in the collider, it is possible to use the precession of the polarization in the ring to measure accurately the average energy of the muons [21]. The total energy of electrons produced by muon decay observed in a calorimeter placed in the ring varies from turn to turn due to the $g-2$ precession of the muon spin, which is proportional to the Lorentz factor γ of the muon beam. Figure 39 shows the result of a fit of the total electron energy observed in a calorimeter to a functional form that includes muon decay and spin precession [21]. Figure 40 shows the fractional error $\delta\gamma/\gamma$ obtained from a series of such fits plotted against the fractional error of measurement in the total electron energy that depends on the electron statistics. It has been shown [21] that precisions of a few parts per million in γ are possible with modest electron statistics of $\approx 100,000$ detected. It should be noted that there are 3.2×10^6 decays per meter for a muon intensity of 10^{12} muons.

1. Possible Implementation Strategy

Our current plans to measure the energy due to decay electrons entail an electromagnetic calorimeter that is segmented both longitudinally and transversally placed inside an enlarged beam pipe in one of the straight sections in the collider ring. The length of the straight section upstream of the calorimeter can be chosen to control the number of decays (3.2×10^6 decays per meter for a beam intensity of 10^{12} muons) and hence the rate of energy deposition. The sensitive material can be gaseous, since the energy resolution is controlled by decay fluctuations rather than sampling error. In order to measure the total number of electrons entering the calorimeter, we plan to include a calorimeter layer with little absorber upstream of it as the first layer.

This scheme will enable us to calibrate and correct the energy of individual bunches of muons and permit us to measure the width of a low mass Higgs boson.

VIII. RADIATION AND BACKGROUNDS

A. Conventional Radiation

The proton source generates a 4 MW proton beam which is comparable to the proposed spallation sources [29]. This is a very high power and will, as in the spallation sources, require great care in reducing unwanted particle losses, as well as careful machine shielding, and target and beam dump design. Initial studies of the target and capture solenoid region have been performed with the MARS code, and preliminary specifications for shielding determined, but more work is needed.

The cooling and accelerator chain is rather clean: a relatively small fraction of the muons decay, and their energies are low. Power deposited in the accelerators is (see Tables VIII, IX, and X) typically about 10-30 W/m.

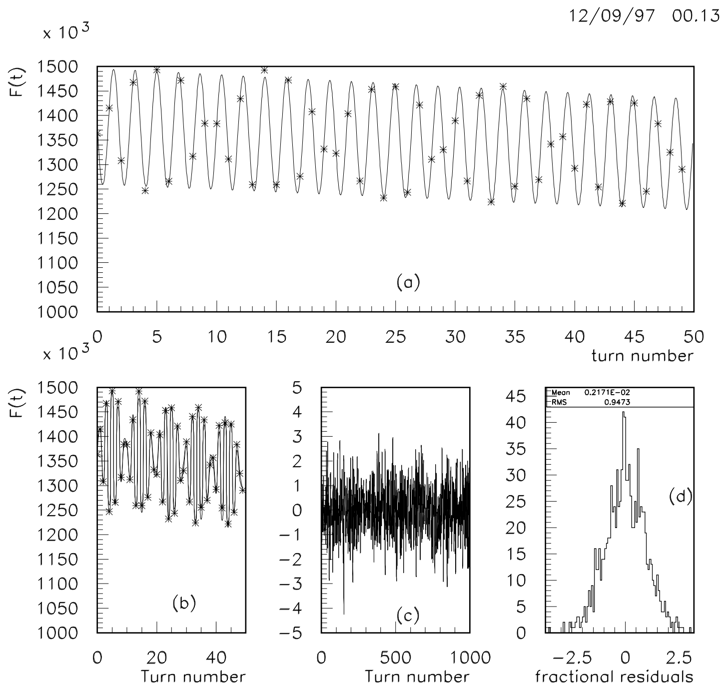

FIG. 39. (a) Energy detected in the calorimeter during the first 50 turns in a 50 GeV muon storage ring (points). An average value of $\hat{P} = -0.26$ is assumed and a fractional fluctuation of 5×10^{-3} per point. The curve is the result of a MINUIT fit to the expected functional form. (b) The same fit, with the function being plotted only at integer turn values. A beat is evident. (c) Pulls as a function of turn number (d) Histogram of pulls. A pull is defined by (measured value-fitted value)/(error in measured-fitted).

If no muons are lost, then the only sources of radiation are the muon decays yielding electrons and neutrinos. The neutrino radiation we discuss below. The electrons shower in the collider beam pipe shields, depositing most of their energy there and a relatively small amount in the magnet coils and yoke. For a 4 TeV example, the MARS code [116] calculated doses after five years operation, immediately after turn off, and 1 day after turn off, are given in Tb. XII. It is seen that the areas in the tunnel, but outside the magnets are relatively free of radioactivation. Special procedures will be needed when the shield pipe has to be opened, as for instance when a magnet is changed. For the lower energy colliders, the radioactivation levels are proportionally less.

TABLE XII. 4 TeV (CoM) collider ring radioactivation levels (mrem/hour) after turn off.

	immediate	after 1 day
Inside face of shield	9000	4000
Outside face of shield	200	170
Outside of Coils	30	14
Outside of Yoke	3	1.4

If muons are lost either accidentally, by scraping, or deliberately after some number of turns, then the muons penetrate to considerable distances (3.5 km at 2 TeV, 800 m at 250 GeV) and deposit their energy primarily near the end of their paths. Figures 41 and 42 show the distribution of radiation levels assuming 25 % of all muons (4 bunches of 2×10^{12} at 15 Hz) are dumped into soil/rock with density 2.24 g/cm^3. It is seen that the radiation is contained within cylinders of radius $\approx$ 15 m. If any water were present in the soil/rock then the first two meters around the aborted beam axis would require insulation or drainage up to a distance of 2.5 km at 2 TeV or 550 m at 250 GeV.

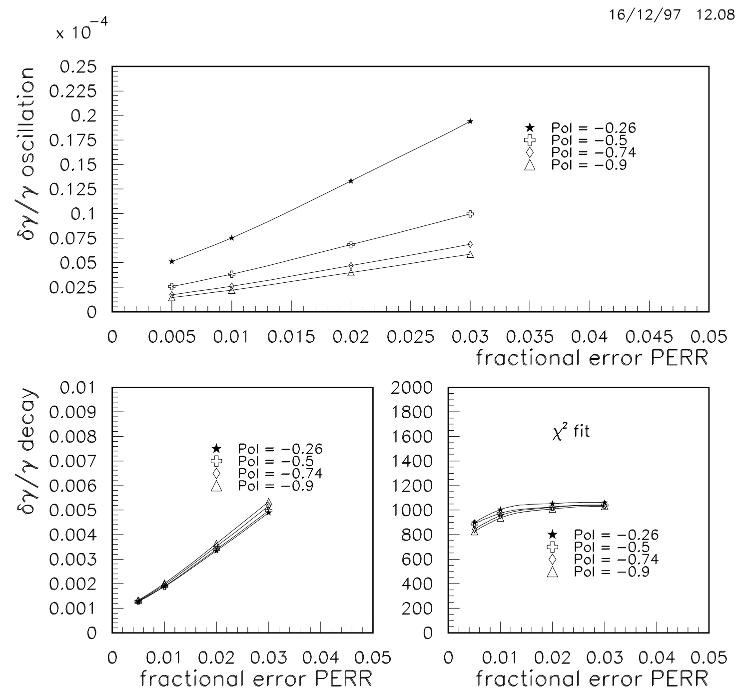

FIG. 40. (a) Fractional error in $\delta\gamma/\gamma$ obtained from the oscillations as a function of polarization $\hat{P}$ and the fractional error in the measurements PERR. (b) Fractional error in $\delta\gamma/\gamma$ obtained from the decay term as a function of polarization $\hat{P}$ and the fractional error in the measurements PERR. (c) The total χ^2 of the fits for 1000 degrees of freedom. PERR is the percentage measurement error on the total electron energy in the calorimeter measuring the decay electrons.

B. Neutrino Radiation

It had been noticed [117] that the neutrinos created in muon beam decays can generate excessive secondary radiation at large distances from a muon collider (see Fig. 43). The surface radiation dose $D_B(Sv)$ over a time $t(s)$, in the plane of a bending magnet of field B(T), in a circular collider with beam energy $E(TeV)$, average bending field $< B(T) >$, at a depth $d(m)$ (assuming a spherical earth), with muon current (of each sign) of I_μ(muons/s/sign) is given by:

$$D_B \;\approx\; 4.4 \times 10^{-24}\; \frac{I_\mu\; E^3\; t}{d}\; \frac{< B >}{B} \tag{4}$$

and the dose D_S at a location on the surface, in line with a high beta straight section of length $\ell(m)$ is:

$$D_S \;\approx\; 6.7 \times 10^{-24}\; \frac{I_\mu\; E^3\; t}{d}\; \ell < B >. \tag{5}$$

The later equation assumes that the average divergence angles satisfy the condition: $\sigma_\theta << \frac{1}{\gamma}$. This condition is not satisfied in the straight sections approaching the IP, and these regions, despite their length, do not contribute a significant dose. These expressions have been confirmed, and refined, by Monte Carlo simulations [118] using the MARS code. For the 3 TeV parameters given in Tb. I (muon currents $I_\mu = 6 \times 10^{20}\, \mu^-/yr$, $< B >= 6\,T$, $B = 10\,T$), and taking the federal limit on off site radiation Dose/year, D_{Fed} to be 1 mSv/year (100 mrem/year), then the annual dose D_B (1 year is defined as 10^7 s), in the plane of a bending dipole is,

$$D_B = 1.07 \times 10^{-5}\ \text{Sv}\ \approx 1\%\ D_{Fed}, \tag{6}$$

and for a straight section of length 0.6 m is:

$$D_S = 9.7 \times 10^{-5}\ \text{Sv}\ \approx 10\%\ D_{Fed}, \tag{7}$$

which may be taken to be within a reasonable limit.

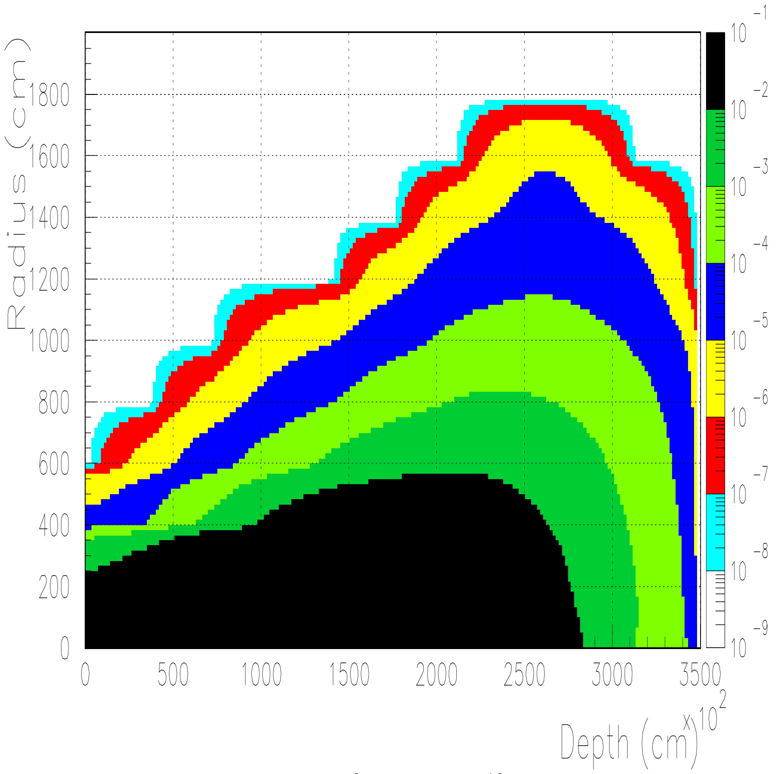

FIG. 41. Isodose contours in the soil/rock (ρ=2.24 g/cm^3) for 3×10^{13} extracted 2 TeV muons per second. Right scale is dose rate in rem/s.

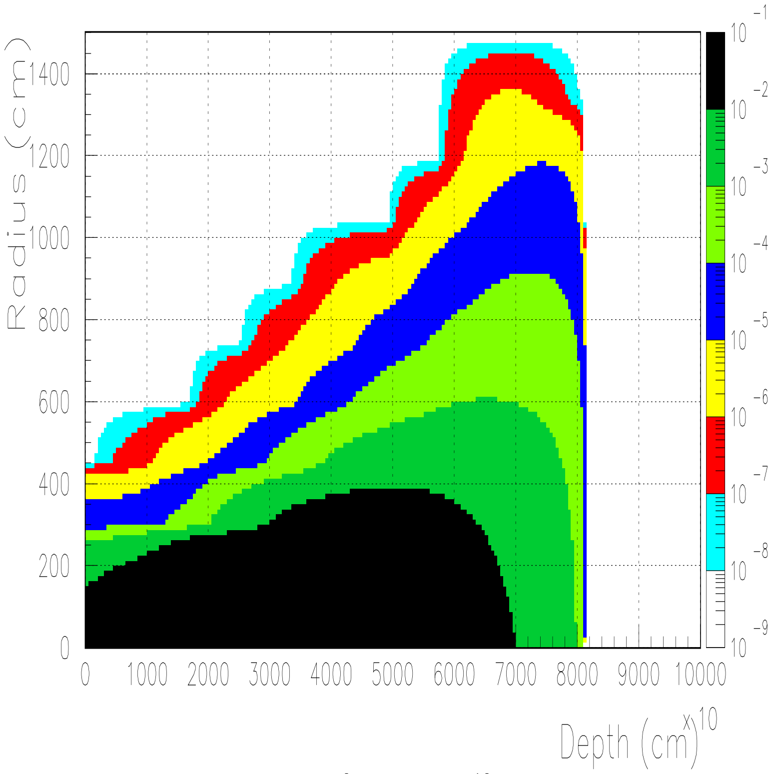

FIG. 42. Isodose contours in the soil/rock (ρ=2.24 g/cm^3) for 3×10^{13} extracted 250 GeV muons per second. Right scale is dose rate in rem/s.

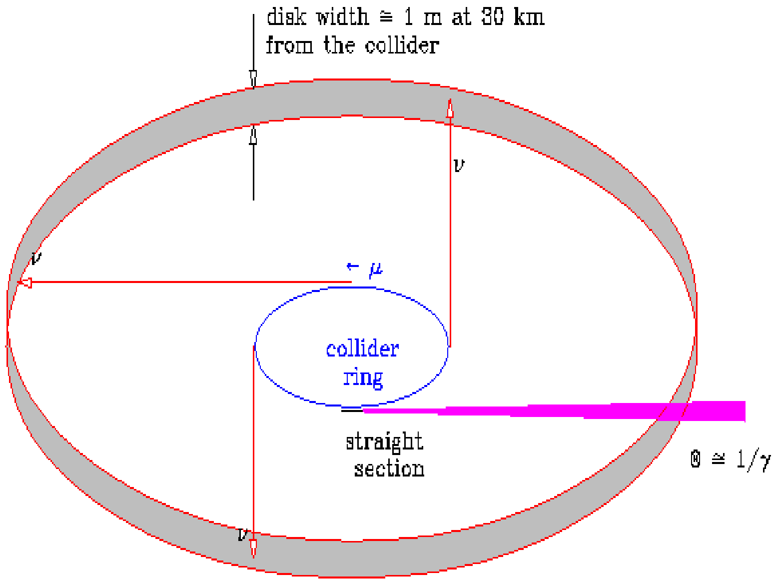

FIG. 43. Neutrino radiation disk. For a 3 TeV CoM collider the neutrino radiation width is ≈ 1 m at a distance of 30 km. A *hot spot* produced by 0.1 m straight section in the ring contains twice the number of neutrinos on the disk on average.

Special care will be required in the lattice design to assure that no field free region longer then 0.6 m is present. This may sound difficult, but it may be noted that the presence of a field of even 1 T, over any length, is enough to reduce the dose to a level below the federal limit. The application of such a field over all rf and other components seems possible [118,119].

For lower energy machines, the requirements get rapidly easier: a 0.5 TeV machine at 500 m depth could have 130 m straight sections, or if at 100 m depth then 25 m long sections, for the same surface dose. For a 100 GeV machine the doses are negligible.

For machines above 3 TeV, various strategies can be employed:

- The machines could be built at greater depths (mines many km deep are common).
- The vertical beam orbits in the machine could be varied so as to spread the plane of radiation and thus reduce the peak doses.
- The specific locations in line with straight sections could be purchased and restricted.
- Straight sections could be further reduced by using continuous combined function magnets.
- The machines could be built on an island. This would be particularly attractive since the radiation above water is intrinsically less (because of the lower water density), as well as being unoccupied for significant times.

But for any large increase in energy, to 10 TeV for instance, some reduction in muon beam flux will probably be required. The resultant loss of luminosity might be made up in a number of ways:

- The beam-beam tune shift constraint could be avoided by introducing a conducting medium (e.g. liquid lithium) at the interaction point [120].
- The focusing strength could be increased by the use of plasma or other exotic focusing method.
- Better cooling could be developed. Optical Stochastic Cooling [57], for instance, might reduce the emittances by many orders of magnitude, thus greatly reducing the required beam currents. Indeed, such cooling would require lower currents to function appropriately.

Such options will need future study.

C. Muon Decay Background

With 4×10^{12} muons per bunch in the collider ring there are approximately 4×10^5 muon decays per meter giving rise to high energy electrons. These off-energy, off-axis electrons undergo bremsstrahlung when they traverse magnetic fields and when exiting the beam pipe interact and produce electromagnetic showers and to a lesser extent hadrons and muons. Much of this debris can be locally shielded so the primary concern is muon decays near the Intersection Point (IP) [20]. This is the background we discuss in some details below.

Figure 44 shows the final 130 meters which include four quadrupoles, dipoles and a solenoidal field surrounding the detector. Detailed Monte Carlo simulations of electromagnetic, hadronic and muon components of the background

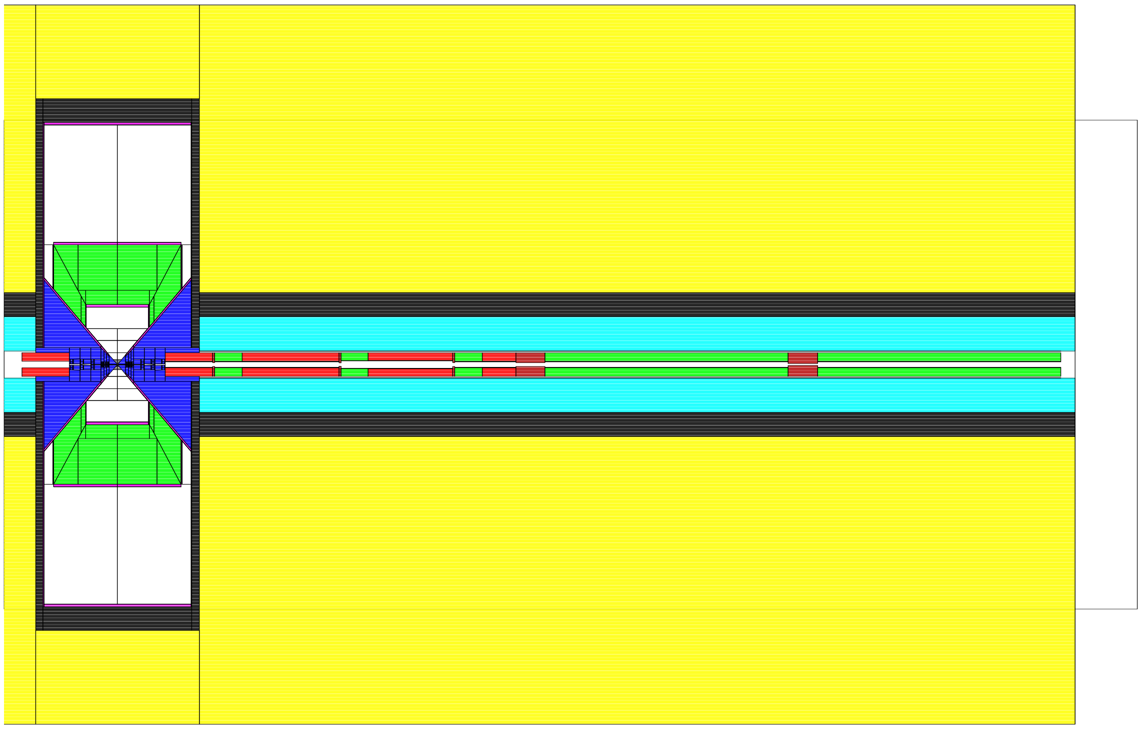

FIG. 44. Region around the Intersection region modeled in GEANT. The triangular blue regions represent tungsten shielding. On the right side of the figure, the red areas represent quadrupoles in the beam line. The areas around the IP represent the various detector volumes used in the calculations of particle fluences.

[20,99,107,112,119,121,122] have been performed using the MARS [38] and GEANT [68] codes. The most recent study [121] has been done with GEANT.

The latest study:

- followed shower neutrons and photons down to 40 keV and electrons to 25 keV.
- used a tungsten shield over the beam, extending in to within 14 cm of the intersection point, and extending outward to an angle of 20 degrees from the axis.
- inside this shield, between its smallest aperture 1 m from the IP, and its tip, the inner surface is shaped into a series of rising collimating steps and slopes, designed so that, the detector could not *see* any surface directly illuminated by the initial decay electrons, whether in the forward or backward (albedo) directions (see Fig. 45).
- from the aperture point of minimum radius to a few meters (2.5 m for Higgs Factory) upstream, the inside forms another series of stepped collimators placed at $\pm\ 4\ \sigma_{\theta_0}$ (where σ_{θ_0} is the rms divergence of the beam).
- further upstream, prior to the first quadrupole (from 2.5 to 4 m in the Higgs case) an 8 T dipole, with collimators inside, is used to sweep decay electrons before the final collimation.

Every modern detector will have to be able to identify and reconstruct secondary vertices such as b's. In order to estimate the viability of a vertex detector we have to show that the occupancy of its elements is not higher than about

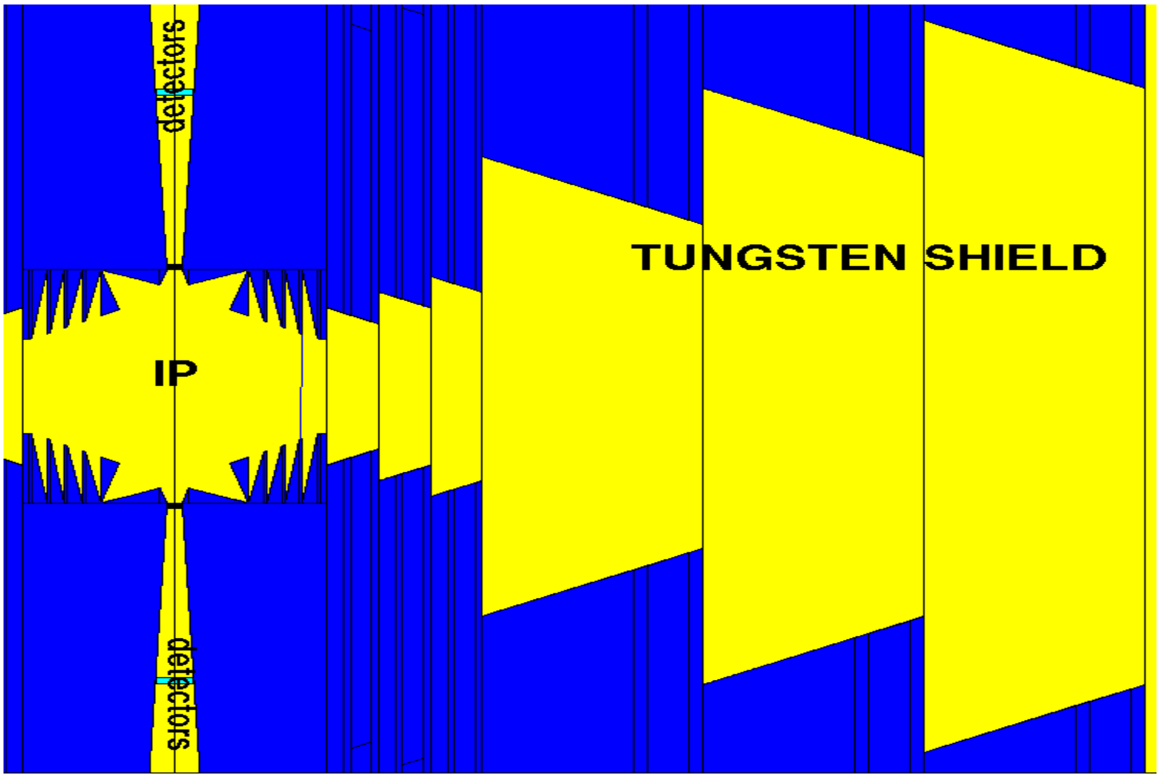

FIG. 45. Detail of the tungsten shielding designed so that the detector is not connected with an straight line with any surface hit by decay electrons in both forward or backward direction.

1 %. Figure 46 shows the occupancy as a function of radial distance from the Intersection Point for the three CoM energies studied : 100, 500 GeV and 4 TeV . The occupancy was calculated for silicon pads of 300×300 μm. One can observe that the total occupancy (left figure) is above one percent for small radii . The majority of the hits are due to conversions of photons. Since the average energy of the background photons is only 1 MeV, then if one uses a pair of silicon detectors inter-spaced by about 1 cm, the electrons resulting from photon conversions will curl in the 4 T solenoidal field and will never trigger the second member of the paired detectors. A simple coincidence requirement would eliminate most of the hits induced by neutral particles. The remaining charged occupancy is below 1% (right figure). One can also lower the occupancy at small radii by using smaller pixel sizes, as, for instance, indicated in Tb. XIII below.

Table XIII gives the hit density for the Higgs factory from the various sources and the occupancy of pixels of the given sizes; in all cases the numbers are given per bunch crossing. The hit density for the higher energy machines is found to be somewhat lower than these, due to the smaller decay angles of the electrons.

TABLE XIII. Detector backgrounds from μ decay

Radius	cm	5	10	20	100
Photons hits	cm^{-2}	26	6.6	1.6	0.06
Neutrons hits	cm^{-2}	0.06	0.08	0.2	0.04
Charged hits	cm^{-2}	8	1.2	0.2	0.01
Total hits	cm^{-2}	34	8	2	0.12
Pixel size	μm^2	60×150	60×150	300×300	300×300
Occupancy all	%	0.6	0.14	0.4	0.02
Occupancy charged	%	0.14	0.02	0.04	0.002

The radiation damage by the neutrons on a silicon detector has also been estimated. In the Higgs case, at 5 cm from the vertex, the number of hits from neutrons above 100 keV is found to be 1.8×10^{13} per year. This is significantly less than that expected at the LHC (LHC is now ordering silicon detectors claimed to have a life expectancy of 5×10^{14},

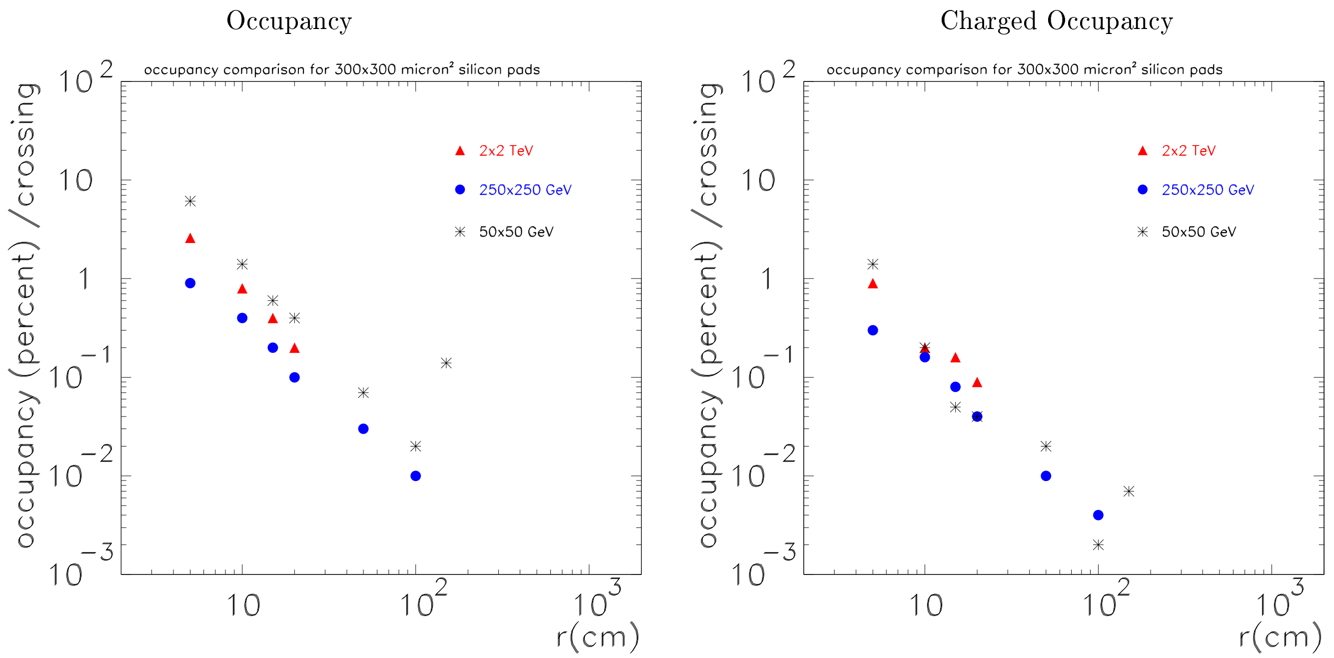

FIG. 46. Occupancy as a function of the radius for the three energies studied. Left figure shows the total occupancy and right the charged occupancy.

approximately three times that assumed here). The damage for silicon detectors in the higher energy machines is of the same order (see Tb. XIV).

TABLE XIV. Radiation damage by neutrons on silicon detectors. The working assumptions are: 1000 turns, 15 Hz and 1 year=10^7 s. An acceptable number of hits per year is 1.5×10^{14}.

CoM (TeV)	μ's/bunch (10^{12})	neutrons/cm^2/crossing (above 100 KeV)	Hits/year (10^{13})	Lifetime (years)
4	2	100	3	5
0.5	4	50	3	5
0.1	4	30	1.8	8

This study also found a significant flux of muons, with quite high energies, from μ pair production in electromagnetic showers (Bethe-Heitler). Their most serious effect appears to arise when they make deeply inelastic interactions and deposit spikes of energy in the electromagnetic and hadronic calorimeters. This is not serious in the Higgs case, for which the fluxes and cross sections are low, but at higher energies timing and/or longitudinal calorimeter segmentation appears necessary to identify and remove the problem.

Earlier studies with the code MARS, using less sophisticated shielding, gave results qualitatively in agreement with those from GEANT.

D. Halo Background

Muon halo refers to those muons which are lost from the beam bunch as it circulates around the collider ring. In conventional electron or proton accelerators, beam particles which are lost away from the IP are of little concern as they can be locally shielded. However, muons can traverse long distances and therefore, have the potential to generate background in a detector. The magnitude of this background depends on a detailed knowledge of the injected beam profile and a credible model for beam halo and beam losses. More work is needed before these are well enough understood. Nevertheless, it is clear that the beam will need careful preparation before injection into the collider, and the injection system will have to be precise and free of ripple.

The collimation system described in the previous subsection was designed to scrape the beam both initially and during the 1000 turns, to assure that all loss occurs at the scraper and not near the IP. That study indicated suppressions better than 10^3 of background in the detector [100].

Beam loss must be limited as far as possible. Gas scattering has been studied [123] and shown to give a negligible contribution. The effects of beam-beam scattering are under study and need further work. Momentum spread tails from uncorrected wake field effects must be controlled. Assuming that the total loss from all causes, after injection and the first few turns is less than 10^{-4} in 1000 turns, (i.e. 10^{-7} per turn), then the number of background muons passing through the detector should be less than 800 ($2 \times 4 \times 10^{12} \times 10^{-3}$/[1000 turns]). This is a low density of tracks per cm^2 and should be acceptable, but lower losses or better scraping would be desirable.

E. Pair Production

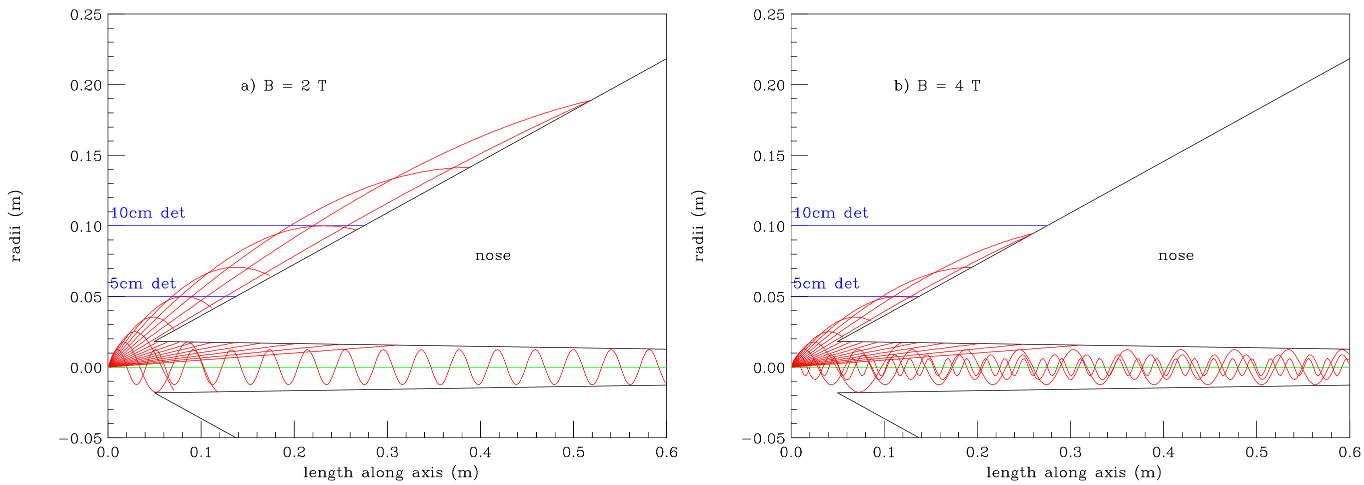

FIG. 47. Radius vs. length of electron pair tracks for initial momenta from 3.8 to 3000 MeV in geometric steps of $\sqrt{2}$; (a) for a solenoid field of 2 T, (b) for 4 T.

Coherent beam-beam electron pair production (beamstrahlung), despite an early worry, has been shown [109,124] to be negligible, but the incoherent pair production (i.e. $\mu^+\mu^- \rightarrow e^+e^-$) in the 4 TeV collider case is significant.

The cross section is estimated to be 10 mb [124], which would give rise to a background of $\approx 3 \times 10^4$ electron pairs per bunch crossing. The electrons at production, do not have significant transverse momentum, but the fields of the oncoming 3 μm bunch can deflect them towards the detector. A simple program was written to track electrons from close to the axis (the worst case) as they are deflected away from the bunch center. Once clear of the opposing bunch, the tracks spiral under the influence of the experimental solenoid field. Figures 47 shows the radii vs. length of these electron tracks for initial momenta from 3.8 to 3000 MeV in geometric steps of $\sqrt{2}$, Fig. 47(a) for a solenoidal field of 2 T and Fig. 47(b) for 4 T. In the 2 T case, tracks with initial energy below 30 MeV do not make it out to a detector at 10 cm, while those above 100 MeV have too small an initial angle and remain within the shield. Approximately 10 % (3000) of these are in this energy range and pass through a detector at 10 cm. The track fluence at the ends of the detector are less than 10 tracks per cm^2 which should not present a serious problem. At 5 cm, there are 4500 tracks giving a fluence of 30 per cm^2, which is also probably acceptable. If the detector solenoid field is raised to 4 T, then no electrons reach 10 cm and the flux at 5 cm is reduced by a factor of 2.

F. Bethe-Heitler Muons

The GEANT study also found a significant flux of muons, with quite high energies, from μ pair production in electromagnetic showers (Bethe-Heitler). Figures 48 and 49 show the trajectories of typical muons from their sources in the shielding around the beam pipe to the detector. Figure 48 is for a 4 TeV CoM collider, where the muons have high energy and long path lengths. A relatively long (130 m) section of beam pipe prior to the detector is shown. Figure 49 is for the 100 GeV CoM collider for which, since the muons have rather short path lengths, only a limited length of beam pipe is shown. Note that the scales are extremely distorted: the 20^o shielding cones on the right hand side of the figures appear at much steeper angles.

Their most serious effect appears to arise when they make deeply inelastic interactions and deposit spikes of energy in the electromagnetic and hadronic calorimeters. This is not serious in the Higgs case, for which the fluxes and

TABLE XV. Bethe Heitler Muons

CoM Collider Energy (TeV)	4	0.5	0.1
Assumed source length (m)	130	33	20
μ ($p_{muon} > 1\ GeV/c$) per electron	5.4×10^{-4}	8.3×10^{-5}	9.6×10^{-6}
Beam μ's per bunch	2×10^{12}	2×10^{12}	4×10^{12}
B.H. μ's per bunch crossing ($\times 10^3$)	28	17.5	6.1
$< p_{muon} >$ initial (GeV)	22	9.5	4.4
μ's entering calorimeter	220	160	25
$< p_{muon} >$ (GeV)	15.4	6.3	1.8
$< E_{dep} >$ (GeV)	2.9	1.3	0.4
Total E_{dep} (GeV)	640	210	10
E_{dep} pedestal subtracted (GeV)	50	25	1
Fluctuation in E_{dep} (GeV)	55	15	1
E_{trans} pedestal subtracted (GeV)	15	15	.5
Fluctuation in E_{trans} (GeV)	40	8	0.5

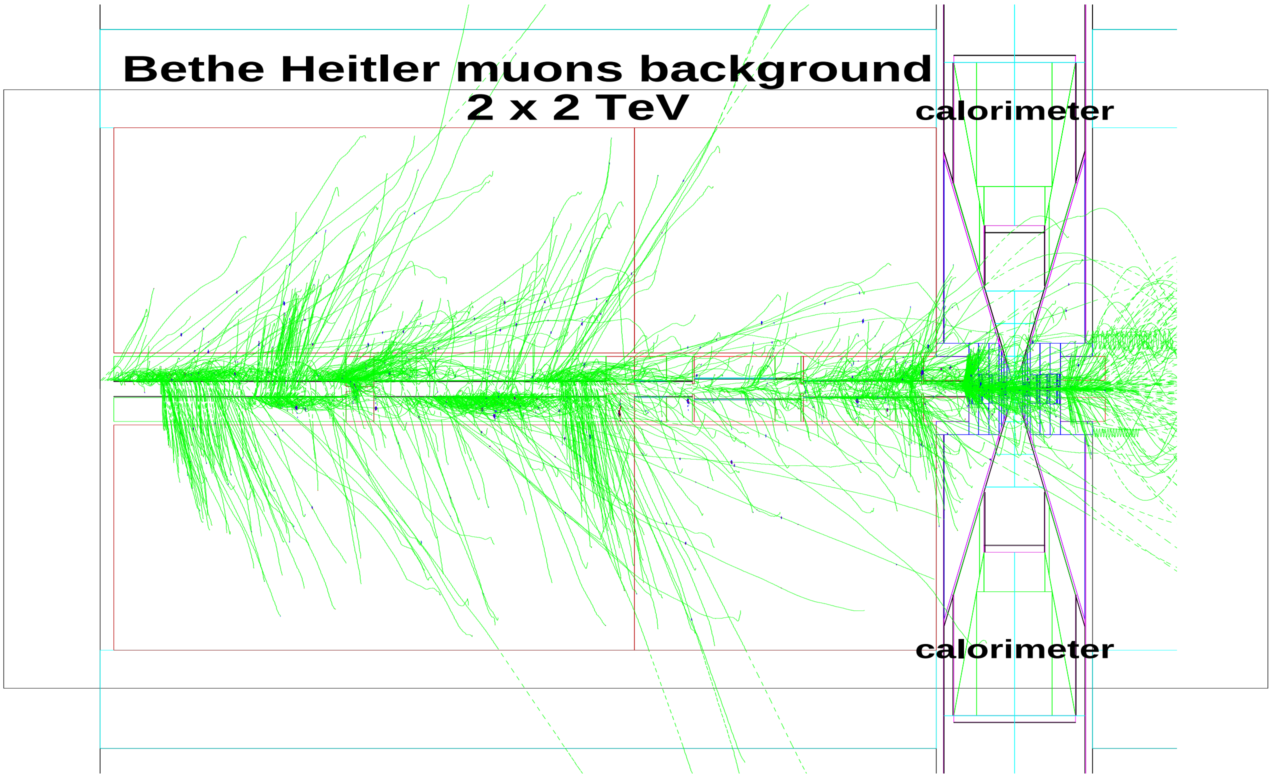

FIG. 48. Trajectories of typical Bethe Heitler muons from their source in the shielding around the beam pipe to the detector for a 4 TeV CoM collider. Notice that $< 1\,\%$ of the tracks end in the calorimeter (see Tb. XV)

cross sections are low, but at the higher energies they generate significant fluctuations in global parameters such as transverse energy and missing transverse energy

Table XV gives some parameters of the muons for three different machine energies. In the 4 TeV and 500 GeV CoM cases, massive lead shielding outside the focus quadrupoles has been included.

Figures 50 and 51 show energy deposition from Bethe Heitler muons in a typical bunch crossing; they are plotted against the cosine of the polar angle and azimuthal angles in the calorimeter for 4 TeV and for 500 GeV CoM respectively. The massive lead shielding referred to above was not included in this study. Right hand side plots in Figs. 50 and 51 show the same distributions with a 1 ns timing cut. It is seen that the timing cut, if it is possible, is effective at removing energy spikes at small rapidity, but has little effect in the forward and backward directions. The overall reduction in energy deposition is about a factor of two.

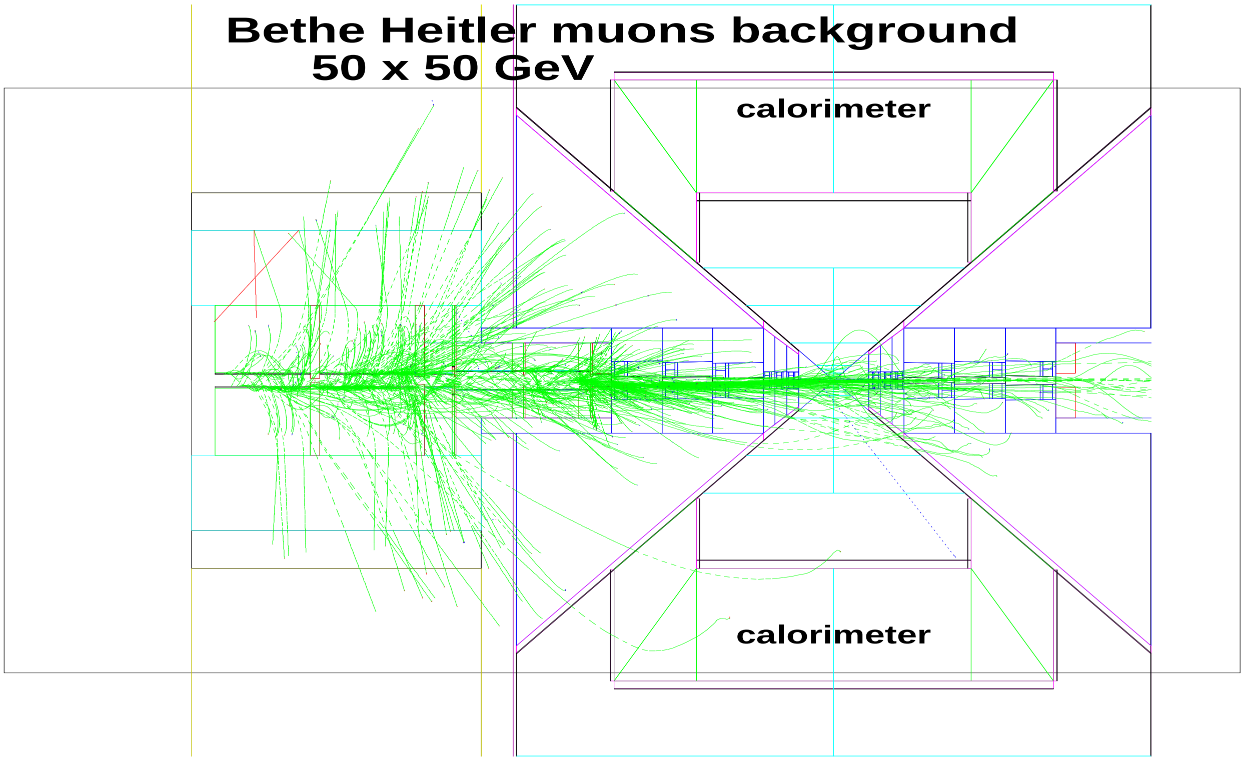

FIG. 49. Trajectories of typical Bethe Heitler muons from their source in the shielding around the beam pipe to the detector for 100 GeV CoM collider. Notice that $< 0.5\,\%$ of the tracks end in the calorimeter (see Tb. XV)

The energy spikes can cause several problems: they affect the triggers and event selections based on overall or transverse energy balance; they can generate false jets and they can give errors in the energies of real jets. After a pedestal subtraction, the effects on energy balances do not seem serious. The generation of false jets can be eliminated by a longitudinal energy distribution cut without introducing significant inefficiency. Energy errors in real jets appears to be the most serious problem. They can be reduced by the application of radial energy distribution cuts, but such cuts introduce significant inefficiencies for lower energy jets. More study is needed.

Earlier studies [122] with the code MARS, using less sophisticated shielding, gave results qualitatively in agreement with those from GEANT.

IX. CONCLUSION

Unlike protons, muons are point like but, unlike electrons, they emit relatively little synchrotron radiation and can be, therefore, accelerated and collided in rings. As a result, a muon collider with a given energy reach could be smaller than either a proton or electron machine. A 3 TeV muon collider (with effective energy comparable with that of an SSC) would fit on existing sites, such as BNL or FNAL. Another advantage resulting from the low synchrotron radiation is the lack of beamstrahlung and the possibility of very small collision energy spreads. A beam energy spread of ΔE/E of 0.003 % (equivalent to a CoM spread of ΔE/E of 0.002 %) is considered feasible for a 100 GeV machine; and it has been shown that by observing spin precession , the absolute energy could be determined to a small fraction of this width. These features become important in conjunction with the large s-channel Higgs production ($\mu^+\mu^- \to h$, 43000 times larger than for $e^+e^- \to h$), allowing precision measurements of the Higgs mass, width and branching ratios.

Such machines are clearly desirable. The questions are:

- whether they can be built and physics done with them
- what will they cost.

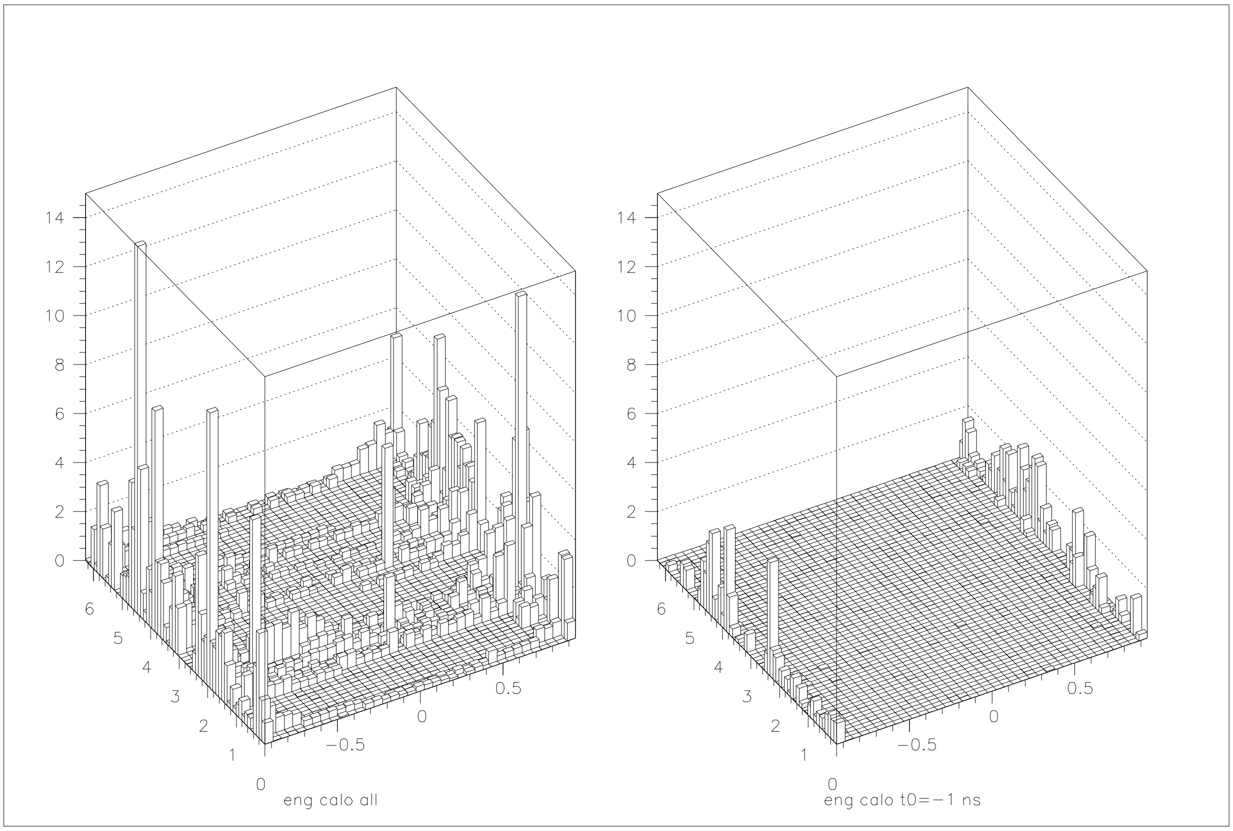

FIG. 50. Left hand-side plot shows the energy deposition from Bethe Heitler muons *vs.* the cosine of the polar angle and azimuthal angles in the calorimeter for 4 TeV CoM collider. Right hand-side plot shows the same distributions with a 1 ns timing cut.

Much progress has been made in addressing the first question and the answer, so far, appears to be yes. It is too early yet to address the second.

We have studied machines with center of mass energies of 100 GeV, 400 GeV and 3 TeV, defined parameters and simulated many of their components. Most recent work has been done on the 100 GeV *First Muon Collider*, the exact energy taken to be representative of the actual mass of a Higgs particle. A summary of progress and challengers follows:

a. Proton Driver The specification of the proton driver for the three machines is assumed the same: 10^{14} protons/pulse at an energy above 16 GeV and 1-2 ns rms bunch lengths. There have been three studies of how to achieve them. The most conservative, at 30 GeV, is a generic design. Upgrades of the FNAL (at 16 GeV) and BNL (at 24 GeV) accelerators have also been studied. Despite the very short bunch requirement, each study has concluded that the specification is attainable. Experiments are planned to confirm some aspects of these designs.

b. Muon Production Pion production has been taken from the best models available, but an experiment (BNL-E910) that has taken data, and is being analyzed, will refine these models. The assumed 20 T capture solenoid appears to be well within current technology (a coil with the specified field and aperture is now nearing completion at FSU). Capture, decay and phase rotation have been simulated, and have achieved the specified production of 0.3 muons per initial proton. The most serious remaining questions for this part of the machine are:

1. The nature and material of the target: The baseline assumption is that a liquid metal jet will be used, but the effects of shock heating by the beam, and of the eddy currents induced in the liquid as it enters the solenoid, are not yet fully understood.

2. The maximum RF field in the phase rotation. For the short pulses used, the current assumptions would be reasonably conservative under normal operating conditions, but the effects of the massive radiation from the nearby target are not known.

Both these questions can be answered in a target experiment planned to be performed within the next two years at the BNL AGS.

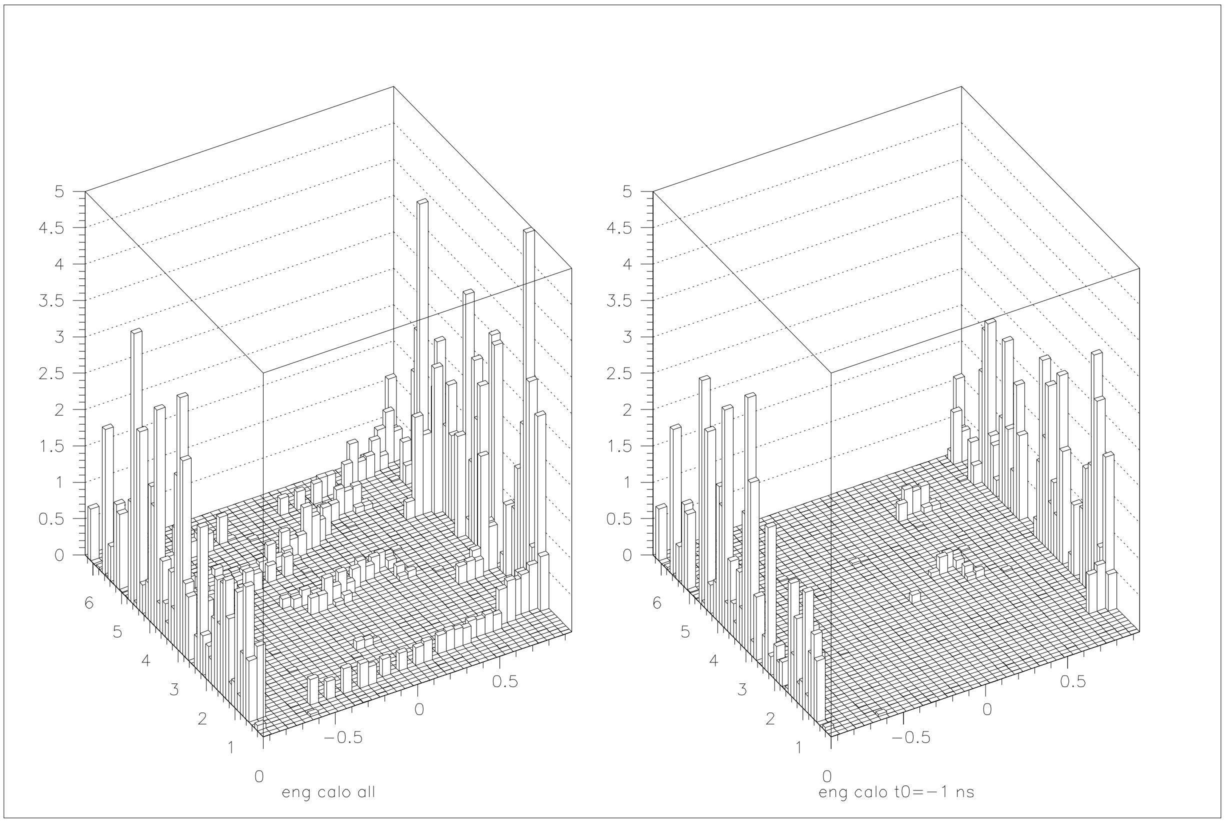

FIG. 51. Left hand-side plot shows the energy deposition from Bethe Heitler muons *vs.* the cosine of the polar angle and azimuthal angles in the calorimeter for 500 GeV CoM collider. Right hand-side plot shows the same distributions with a 1 ns timing cut.

c. Cooling The required ionization cooling is the most difficult and least understood element in any of the muon colliders studied. Ionization cooling is a phenomenon that occurs whenever there is energy loss in a strong focusing environment. Such an environment has existed, for instance, in the iron toroid muon calorimeters of several neutrino experiments, and a Monte Carlo simulation has shown [117] that cooling must have occured there. But achieving the nearly 10^6 reduction required is a challenge. Cooling over a wide range has been simulated using lithium lenses and ideal (linear matrix) matching and acceleration; and examples of limited sections of solenoid lattices with realistic accelerating fields have now been simulated, but the specification and simulation of a complete system has not yet been done. Much theoretical work remains: space charge and wake fields must be included; lattices at the start and end of the cooling sequences must be designed; lattices including liquid lithium lenses must be studied, and the sections must be matched together and simulated as a full sequence. The tools for this work are nearly ready, and this project should be completed within two years.

Technically, one of the most challenging aspects of the cooling system appear to be:

- High gradient RF (e.g. 36 MV/m at 805 MHz) operating in strong (5-10 T) magnetic field, with beryllium foils between the cavities.

An experiment is planned that will test such a cavity, in the required fields, in about two years time. On an approximately six year time scale, a "Cooling Test Facility" is being proposed that could test ten meter lengths of different cooling systems. If they are required, then an urgent need is to develop:

- Lithium Lenses: (e.g. 2 cm diameter, 70 cm long, liquid lithium lenses with 10 T surface fields and a repetition rate of 15 Hz).

The use of 31 T solenoids could avoid their need, at least in a the low energy "First Muon Collider", which would ease the urgency of this rather long term R & D, but more study is needed. Meanwhile a short lithium lens is under construction at BNIP (Novosibirsk, Russia).

d. Acceleration The acceleration system is probably the least controversial, although possibly the most expensive, part of a muon collider. Preliminary parameters have been specified for acceleration sequences for a 100 GeV and 3 TeV machines, but they need refinement. In the low energy case a linac is followed by three recirculating, or FFAG, accelerators. In the high energy accelerator, the recirculating, or FFAG, accelerators are followed by three fast ramping synchrotrons employing alternating pulsed and superconducting magnets. The parameters do not appear to be extreme, and it does not appear as if serious problems are likely.

e. Collider The collider lattices are challenging because of their required very low intersection betas, high single bunch intensities, and short bunch lengths; however, the fact that all muons will decay after about 1000 turns means that slowly developing instabilities are not a problem. Feasibility lattices have been generated for a 4 TeV case, and more detailed designs for 100 GeV machines studied. In the latter case, but still without errors, 5σ acceptances in both transverse and longitudinal phase space have been achieved in tracking studies. Beam scraping schemes have been designed for both the low energy (collimators) and high energy (septum extractors) cases.

The short bunch length and longitudinal stability problems are avoided if the rings, as specified, are sufficiently isochronous, but some rf is needed to remove the impedance generated momentum spread. Transverse instabilities (beam breakup) should be controlled by rf BNS damping.

The heating of collider ring superconducting magnets by electrons from muon decay can be controlled by thick tungsten shields, and this technique also shields the space surrounding the magnets from the induced radioactivity on the inside of the shield wall. A conceptual design of magnets for the low energy machine has been defined.

Although much work is yet to be done (inclusion of errors, higher order correction, magnet design, rf design, etc), the collider ring do not appear likely to present serious problems.

f. Neutrino Radiation and Detector Background Neutrino radiation, which naturally rises as the cube of the energy, is not serious for machines with center of mass energies below about 1.5 TeV. It is thus not significant for the First Muon Collider; but above 2 TeV, it sets a constraint on the muon current and makes it harder to achieve desired luminosities. However, advances in cooling, and correction of tune shifts may still allow a machine at 10 TeV with substantial luminosity ($> 10^{35}$ cm^{-2}s^{-1}).

Background in the detector was at first expected to be a very serious problems, but after much work, shielding systems have evolved that limit most charged hadron, electron, gamma and neutron background to levels that are acceptable. Muon background, in the higher energy machines, is a special problem that can cause serious fluctuations in calorimeter measurements. It has been shown that fast timing and segmentation can help suppress this background, and preliminary studies of its effects on a physics experiment are encouraging. The studies are ongoing.

g. Summary Much progress has been made since Snowmass, but much still needs to be done. A time scale of two years should allow completion of simulation studies, and the experimental testing of crucial technical challenges. Prototype construction and testing will be required for another 4-6 years. The construction of a *First Muon Collider* by about 2010 does seems possible.

X. ACKNOWLEDGMENTS

This research was supported by the U.S. Department of Energy under Contracts No. DE-ACO2-98CH10886, DE-AC02-76CH03000 and DE-AC03-76SF00098.

---

[1] G. I. Budker, Accelerators and Colliding Beams, Proc. of the 7th International Acc. Conference (Erevan), 1969.
[2] G. I. Budker, International High Energy Conference (Kiev) (unpublished), 1970.
[3] V. V. Parkhomchuk and A. N. Skrinsky, Ionization Cooling: Physics and Applications, Proc. 12th Int. Conf. on High Energy Accelerators, 1983, eds. F. T. Cole and R. Donaldson.
[4] A. N. Skrinsky and V. V. Parkhomchuk, Sov. J. of Nucl. Physics **12**, 223 (1981).
[5] D. B. Cline, in *Proceedings of the Physics Potential & Development of $\mu^+\mu^-$ Colliders. 2nd Workshop* , edited by D. B. Cline (AIP Press, Woodbury, New York, 1995), Vol. 352, p. 3.
[6] D. Neuffer, Principles and Applications of Muon Cooling, FNAL Report -FN-319, 1979.
[7] D. Neuffer, Part. Acc. **14**, 75 (1983).
[8] Presentation at the Mini-Workshop on $\mu^+\mu^-$ Colliders: Particle Physics and Design. UCLA, 1997.
[9] Proceedings of the Muon Collider Workshop, Los Alamos National Laboratory Report LA-UR-93-866 (1993).

[10] Proceedings of the Physics Potential & Development of $\mu^+\mu^-$ Colliders 2^{nd} Workshop, Vol. 352, edited by D. Cline. AIP Press, Woodbury, New York (1995).

[11] Proceedings of the 9^{th} Advanced ICFA Beam Dynamics Workshop, Vol. 372, edited by J. C. Gallardo. AIP Press, Woodbury, New York (1996).

[12] R. B. Palmer et al., in *Physics Potential & Development of $\mu^+\mu^-$ Colliders 2^{nd} Workshop*, edited by D. Cline (AIP Press, Woodbury, New York, 1995), Vol. 352, p. 108. See Ref. [13].

[13] R. B. Palmer et al., in *Proceedings of the Symposium on Physics Potential & Development of $\mu^+\mu^-$ Colliders*, edited by D. Cline (Nucl. Phys B (Proc. Suppl.), The Netherland, 1996), Vol. 51A, p. 61.

[14] R. B. Palmer and J. C. Gallardo, in *Techniques and Concepts of High Energy Physics IX*, edited by T. Ferbel (Plenum Pub., New York, New York, 1997), Vol. Phy-365, p. 183.

[15] R. B. Palmer and J. C. Gallardo, in *Proceedings of 250^{th} Anniversary Conference on Critical Problems in Physics, Princeton University*, edited by M. Dementi V. Fitch, D. Marlow (Princeton Press, Princeton, NJ, 1997), p. 247.

[16] R. B. Palmer, Progress on $\mu^+\mu^-$ Colliders, submitted to the Proceedings of the PAC97, Vancouver, Canada,(to be published), 1997.

[17] R. B. Palmer for the Muon Collider Collaboration, Muon Collider: Introduction and Status, submitted to the Proceedings of the Workshop on Physics at the First Muon Collider and at the Front End of a Muon Collider, FNAL (to be published), 1997.

[18] R. B. Palmer for the Muon Collider Collaboration, Muon Collider Design, submitted to the Proceedings of the Symposium on Physics Potential & Development of $\mu^+\mu^-$ Colliders, San Francisco, CA (to be published), 1997.

[19] R. B. Palmer A. Sessler and A. Tollestrup, in *Proceedings of the 1996 DPF/DPB Summer Study on High-Energy Physics Snowmass'96,* New Directions for High-Energy Physics (Stanford Linear Accelerator Center, Menlo Park, CA, 1997).

[20] Muon Collider Collaboration, in *Proceedings of the 1996 DPF/DPB Summer Study on High-Energy Physics Snowmass'96,* New Directions for High-Energy Physics (Stanford Linear Accelerator Center, Menlo Park, CA, 1997), for updated information, see the Muon Collider Collaboration WEB page at the URL, http://www.cap.bnl.gov/mumu/. See also Ref. [19].

[21] Rajendran Raja and Alvin Tollestrup, *Calibrating the energy of a* 50×50 *GeV Muon Collider using* $g-2$ *spin precession*, Fermilab-PUB-97-402; hep-ex/9801004; Phys. Rev. D**58**, 013005 (1998).

[22] B. J. King, private communication.

[23] V. Barger M. Berger J. Gunion et al., a collection of all relevant papers is listed at the URL http://www.fnal.gov/projects/muon_collider/physics/physics.html.

[24] Presentations at the Workshop on Physics at the First Muon Collider and at the Front End of the Muon Collider, FNAL, Nov. 1997; available at the URL http://fnphyx-www.fnal.gov/conferences/femcpw97/plenary/talks.html.

[25] S. Geer, presentation at the Workshop on Physics at the First Muon Collider and at the Front End of the Muon Collider, FNAL, Nov. 1997; available at the URL http://www.fnal.gov/projects/muon_collider/talks/steves_nu_talk.ps.

[26] B. King, presentation at the Workshop on Physics at the First Muon Collider and at the Front End of the Muon Collider, FNAL, Nov. 1997; available at the URL http://pubweb.bnl.gov/people/bking/sf97.

[27] Set of transparencies from the Workshop on Physics at the First Muon Collider and at the Front End of the Muon Collider, FNAL (unpublished), 1997.

[28] KAON Factory Study, Accelerator Design Report, TRIUMF, Vancouver, B.C., Canada.

[29] 5 MW Pulsed Spallation Neutron Source, Preconceptual Design Study, BNL-60678, 1994.

[30] C. Ankenbrandt and R. Noble, Summary of the Accelerator Working Group, Presentations at the Workshop on Physics at the First Muon Collider and at the Front End of the Muon Collider, FERMILAB-CONF-98-112, April 1998; available at the URL http://www-lib.fnal.gov/archive/1998/conf/Conf-98-074.html.

[31] M. Blaskiewicz et al., High Intensity Proton Operations at Brookhaven, 1995 Particle Accel. Conf. Dallas, Texas, p. 383, 1995.

[32] C. Ankenbrandt et al., Bunching Near Transition in the AGS, Fermilab Pub-98-006, submitted to Phys. Rev. D.

[33] Z.B. Qian J. E. Griffin, K.Y. Ng and D. Wildman, Experimental Study of Passive Compensation of Space Charge Potential Well Distortion at the Los Alamos National Laboratory Proton Storage Ring, Fermilab Report, FN-661 (1997).

[34] K. Koba et al., 1997, private communication.

[35] R. Noble N. Mokhov and A. Van Ginneken, in *Proceedings of the 9th Advanced ICFA Beam Dynamics Workshop* (AIP Press, Woodbury, New York, YEAR), Vol. 372, http://www-ppd.fnal.gov/muscan/munotes/MC-031.pdf.

[36] N.V. Mokhov and A. Van Ginneken, Technical report, FNAL, (unpublished), Fermilab-Conf-98/041 (1998); http://www-ap.fnal.gov/˜mokhov/papers/1998/Fermilab-Conf-98-41.ps.

[37] S. H. Kahana Y. Pang and T. J. Schlagel, Proceedings of Heavy Ion Physics at the AGS - HIPAGS '93, eds. G. S. F. Stephans, S. G. Steadman and W. L. Kehoe. See also http://bnlnth.phy.bnl.gov/arc/arc.html; D. Kahana and Y. Torun, Analysis of Pion Production Data from E-802 at 14.6 Gev/c Using ARC, July 1995, BNL report BNL-61983.

[38] N. V. Mokhov, The MARS Code System Userś Guide, Fermilab-FN-628, 1995; available at http://www-ap.fnal.gov/MARS/.

[39] N.V. Mokhov and S.I. Striganov, Model for Pion Production in Proton-Nucleus Interactions, Fermilab-Conf-98/053 (Feb. 5, 1998);

http://www-ap.fnal.gov/~mokhov/papers/1998/Fermilab-Conf-98-53.ps. 1997.
[40] J. Ranft, DPMJET version II.3 and II.4, INFN-AE-97-45 (1997); http://preprints.cern.ch/cgi-bin/setlink?base=preprint&categ=scan&id=SCAN-9711078.
[41] Experiment E-910 at BNL-AGS, http://www.nevis.columbia.edu/heavyion/e910/, 1997.
[42] C. Johnson, Solid and Liquid Targets Overview, Proceeding of the Mini-Workshop: Target and Muon Collection Magnets and Accelerators; Oxford, MS (unpublished), 1997.
[43] C. Lu and K. T. McDonald, Low-Melting-Temperature Metals for possible Use as Primary Targets at a Muon Collider Source, Princeton/$\mu\mu$/97-3; http://www.hep.princeton.edu/mumu/mumu-97-3.ps, 1998.
[44] R. Weggel, Deceleration of Conductor by Magnetic Field: 1) Paraxial; 2) Perpendicular, BNL-Technical Report, MU-xxx, 1998.
[45] C. Lu and K. T. McDonald, Flowing Tungsten Powder for Possible Use as the Primary Target at a Muon Collider Source, presentation at the Workshop on Physics at the First Muon Collider and at the Front End of a Muon Collider., 1997, princeton/$\mu\mu$/98-10 (Mar. 15, 1998); http://www.hep.princeton.edu/mumu/mumu-98-10.ps.
[46] B. J. King N. V. Nikolai and R. Weggel, *A Cu-Ni Rotating Band Target for Pion Production at Muon Colliders*, presentation at the Muon Collider Collaboration Meeting, Alabama, March 1998; available at http://pubweb.bnl.gov/people/bking/target_aps98/index.html.
[47] R. Weggel, 4-MW Hollow-Conductor Magnets for 20 T Hybrid Systems to Collect Pions for a Muon Collider, BNL-Technical Report MU-015; presentation at the Mini-Wokshop: Target and Muon Collection Magnets and Accelerators, Oxford, MI, Jan. 1997, 1997.
[48] J. R. Miller et al., IEEE Transactions on Magnetics **30**, 1563 (1994).
[49] R. B. Palmer and J. C. Gallardo, MC, Fortran program to simulate the front end and cooling section (unpublished).
[50] D. Neuffer and A. van Ginneken, (private communication) 1998.
[51] *Proceedings of the 1996 DPF/DPB Summer Study on High Energy Physics, Snowmass'96* (Stanford Linear Accelerator Center, Menlo Park, CA), 1996, pp. 220.
[52] H. Kirk, (private communication).
[53] K. Assamagan et al., Phys. Lett. **B**, 194 (1994). See Ref. [54].
[54] E. P. Wigner, Ann. Math. 194 (1939).
[55] E. P. Wigner, Rev. Mod. Phys. 255 (1957).
[56] B. Norum and R. Rossmanith, in *Proceedings of the Symposium on Physics Potential & Development of $\mu^+\mu^-$ Colliders* (Nucl. Phys B (Proc. Suppl.), The Netherland, 1996), Vol. 51A.
[57] A. A. Mikhailichenko and M. S. Zolotorev, Phys. Rev. Lett. **71**, 4146 (1993).
[58] A. Hershcovitch, Technical report, Brookhaven National Laboratory, (unpublished), report BNL-AGS/AD/Tech. Note No. 413.
[59] P. Chen Z. Huang and R. Ruth, in *Proc. Workshop on Advanced Accelerator Concepts*, edited by P. Schoessow (AIP Press, Woodbury, New York, 1995), Vol. 335, p. 646.
[60] A. Bogacz P. Sandler and D. Cline, in *Physics Potential & Development of $\mu^+\mu^-$ Colliders 2^{nd} Workshop*, edited by D. Cline (AIP Press, Woodbury, New York, 1995), Vol. 352, p. 146.
[61] Initial speculations on ionization cooling have been variously attributed to G. O'Neill and/or G. Budker, see D. Neuffer in [7].
[62] D. Neuffer, in *Advanced Accelerator Concepts* (AIP Press, Woodbury, New York, 1987), Vol. 156, p. 201, see also [3,6,8].
[63] R. C. Fernow and J. C. Gallardo, Phys. Rev **E52**, 1039 (1995).
[64] R. B. Palmer (unpublished).
[65] A. Van Ginneken, Nucl. Instr. Meth **A 362**, (1995).
[66] R. Fernow, ICOOL, Fortran program to simulate muon ionization cooling.
[67] H. Kirk, Parmela modeling of alternating solenoids, presented at the Mini-Workshop on Cooling BNL, (unpublished), 1998.
[68] *GEANT manual, v.3.2.1, CERN program Library W5013*, CERN, 1994.
[69] P. Le Brun, Alternate solenoid in DPGeant, presented at the Mini-Workshop on Cooling, BNL, 1998, (unpublished).
[70] G. Silvestrov, Proceedings of the Muon Collider Workshop, February 22, 1993, Los Alamos National Laboratory Report LA-UR-93-866 (1993), (unpublished).
[71] B. Bayanov et al., Nucl. Inst. and Meth. **190**, 9 (1981).
[72] C. D. Johnson, Hyperfine Interactions **44**, 21 (1988).
[73] M.'D. Church and J. P. Marriner, Annu. Rev. Nucl. Sci. **43**, 253 (1993).
[74] G. Silvestrov, in *Proceedings of the 9th Advanced ICFA Beam Dynamics Workshop*, edited by J. C. Gallardo (AIP Press, Woodbury, New York, 1996), Vol. 372.
[75] D. Neuffer, (unpublished) 1979.
[76] V. Balbekov and A. Van Ginneken, presented at the Mini-Workshop on Cooling, Fermilab Oct. 1997 (unpublished).
[77] D. Neuffer, (unpublished) 1979.

[78] D. Neuffer and A. Van Ginneken, presented at the Mini-Workshop on Cooling, BNL Jan. 1998 (unpublished).
[79] D. Neuffer and W. Wan, COSY transport for μ cooling, presentation at the Mini-Workshop on Cooling, FNAL, 1997, (unpublished).
[80] S/ Geer, spokesman of the MUCOOL Collaboration, Ionization Cooling Research and Development Program for a High Luminosity Muon Collider, Fnal-P904, 1998, available at the URL http://www.fnal.gov/projects/muoncollider/.
[81] K. T. McDonald C. Lu and E. J. Prebys, *A Detector Scenario for the Muon Cooling Experiment*, Princeton/$\mu\mu$/97-8; http://www.hep.princeton.edu/mumu/mumu-97-8.ps, 1997.
[82] F. Mills, Linear Orbit Recirculators, Internal report for Muon Collider Collaboration, 1997.
[83] F. Mills and C. Johnstone, presentation at the 4th Int. Conference on Physics Potential and Development of $\mu^+\mu^-$ Colliders, San Francisco, CA (unpublished).
[84] G. Morgan, presentation at the 9th Advanced ICFA Beam Dynamics Workshop, Montauk 1995 (unpublished).
[85] B. J. King, Variable Field Bending Magnets for Recirculating Linacs, Submitted to Muon Collider Workshop on Acceleration and Magnets, Mississippi University, Oxford, MI. Available at http://pubweb.bnl.gov/people/bking/papers.html, 1977.
[86] Z. D. Farkas et al., SLED: A Method of Doubling SLAC's Energy, SLAC-PUB-1435; Proceedings of the 9^{th} International Conference on High Energy Accelerators (Stanford, CA), 1974, pp. 576-583.
[87] D. J. Summers D. Neuffer Q. S. Shu E. Willen, *Proceedings 1997 Particle Accelerator Conference*, Vancouver, BC, Canada, 1997.
[88] D. J. Summers, *Proceedings of the 1996 DPF/DPB Summer Study on High-Energy Physics, Snowmass'96* (Stanford Linear Accelerator Center, Menlo Park, CA), 1997, pp. 238.
[89] *Allied Signal*, Amorphous Metals Division, 6 Eastmans Road, Parsippany, NJ 07054.
[90] *Magnetics*, Division of Spang & Company, 900 East Butler Road, Butler, PA 16003.
[91] TESLA Collaboration, TESLA Test Facility Linac- Design Report, Ed. D. Edwards, TESLA 95-01, 1995.
[92] D. Neuffer, in *Proceedings of the 9th Advanced ICFA Beam Dynamics Workshop*, edited by J. C. Gallardo (AIP Press, Woodbury, New York, 1996), Vol. 372.
[93] K. L. Brown and J. Spencer, presented at the Particle Accelerator Conf., Washington. SLAC-PUB-2678 (unpublished).
[94] K.L. Brown, SLAC-PUB-4811; Proc. Capri Workshop, 1988.
[95] K. L. Brown J.J. Murray and T.H. Fieguth, Particle Accelerator Conf., Washington, 1987.
[96] Olivier Napoly, CLIC Final Focus System: Upgraded Version with Increased Bandwidth and Error Analysis, CERN Report CLIC Note 227, 1994.
[97] A. Chao, *Physics of Collective Beam Instabilities in High Energy Accelerators* (John Wiley & Sons, Inc., New York, 1993).
[98] A. Garren and C. Johnstone, Lattice Design for a 100 GeV Muon Collider, presentation at the 4^{th} Int. Conference on Physics Potential and Development of $\mu - \mu$ Colliders, San Francisco, CA, 1997, (unpublished).
[99] C. J. Johnstone and N. V. Mokhov, *Optimization of a Muon Collider Interaction Region with Respect to Detector Backgrounds and the Heat Load to the Cryogenic Systems* , Proceedings of the 1996 DPF/DPB Summer Study on New Directions for High Energy Physics (Snowmass'96) and Fermilab-Conf-96/366, 1996.
[100] A. Drozhdin N. Mokhov C. Johnstone et al., *Scraping Beam Halo in $\mu^+\mu^-$ Colliders*, 4th International Conference on Physics Potential and Development of Muon Colliders, Dec. 1997. Fermilab-Conf-98/042, 1998; available at http://www-ap.fnal.gov/ mokhov/papers/1998/Fermilab-Conf-98-42.ps.
[101] M. Donald et al., Localized Chromaticity Correction of Low-Beta Insertions in Storage Rings, Proc. 1993 Part. Accel. Conf., Washington, D.C., pp. 131, 1993.
[102] W. Wan and C. Johnstone, *Tracking simulations of local, interleaved and noninterleaved chromatic correction sextupoles*, presentation at the Mini-Workshop on Lattice, BNL, 1997, unpublished.
[103] K.-Y. Ng S.Y. Lee and D. Trbojevic, Technical Report No. FNAL-FN595, FNAL (unpublished).
[104] K.-Y. Ng S.Y. Lee and D. Trbojevic, Phys. Rev **E48**, (1993).
[105] M. Berz, COSY INFINITY, v. 7. User's Guide and Reference Manual, Michigan State University Report, 1996; also at URL http://www.beamtheory.nscl.msu.edu/cosy/.
[106] L. Schachinger and R. Talman, Part. Accel. **22**, 35 (1987).
[107] G. W. Foster and N. V. Mokhov, in *Proceedings of the Physics Potential & Development of $\mu^+\mu^-$ Colliders*, 2^{nd} Workshop, Vol. 352, edited by D. Cline. AIP Press, Woodbury, New York (1995); Fermilab-Conf-95/037, 1995.
[108] M. Furman, The Classical Beam-Beam Interaction for the Muon Collider: A First Look, BF-19/CBP-Note-169/LBL-38563, 1996.
[109] P. Chen, in *Proceedings of the Symposium on Physics Potential & Development of $\mu^+\mu^-$ Colliders*, Vol. 51A of *Proceedings Suppl. Nucl Phy B*, edited by D. Cline (North-Holland, The Netherland, 1996), p. 179.
[110] A. M. Sessler W.-H. Cheng and J. Wurtele, in *Proceedings of the 9th Advanced ICFA Beam Dynamics Workshop*, edited by J. C. Gallardo (AIP Press, Woodbury, New York, 1996), Vol. 372.
[111] K.Y. Ng, in *Proceedings of the 9th Advanced ICFA Beam Dynamics Workshop*, edited by J. C. Gallardo (AIP Press, Woodbury, New York, 1996).
[112] N. V. Mokhov and S. I. Striganov, *Proceedings of the 9th Advanced ICFA Beam Dynamics Workshop* (AIP Press, Woodbury, New York, 1996), Vol. 372, pp. 234–256; also Fermilab–Conf–96/011 (1996).

[113] E. Willen et al., A Helical Magnet Design for RHIC, *Proceedings 1997 Particle Accelerator Conference*, Vancouver, BC, Canada, 1997.
[114] T. Roser (Spokesperson) et al., Conceptual Design for the Acceleration of Polarized Protons in RHIC, available at the URL http://www.ags.bnl.gov/ roser/cdr07034/cdr07034.html, 1995.
[115] E. Willen, (private communication).
[116] N. V. Mokhov, *Proceedings of the 1996 DPF/DPB Summer Study on High-Energy Physics, Snowmass'96* (Stanford Linear Accelerator Center, Menlo Park, CA), 1996.
[117] B. King, presentation at the Muon Collider Mini-Workshop: Lattice and Background, UCLA and private communication, 1997, (unpublished).
[118] N. V. Mokhov and A. Van Ginneken, Muon Collider Neutrino Radiation, presentation at the Muon Collider Collaboration Meeting, Orcas Is., Washington, 1997.
[119] C. Johnstone and N. V. Mokhov, Proceedings 1997 Particle Accelerator Conference, Vancouver, BC, Canada, 1997.
[120] A. Skrinsky, submitted to Proc. of the 4th Int. Conf. on Physics Potential and Development at $\mu^+\mu^-$ Colliders, San Francisco, CA, 1997, (to be published).
[121] I. Stumer et al., in *Proceedings of the 1996 DPF/DPB Summer Study on High-Energy Physics, Snowmass'96* (Stanford Linear Accelerator Center, Menlo Park, CA, 1996).
[122] N. V. Mokhov, Nucl. Phys. B **51A**, 210 (1996).
[123] See [20], section 8.5.3.
[124] I. Ginzburg, in *Proceedings of the Symposium on Physics Potential & Development of $\mu^+\mu^-$ Colliders*, Vol. 51A of *Proceedings Suppl. Nucl Phy B*, edited by D. Cline (North-Holland, The Netherland, 1996), p. 186.